PACIFIC EARTHQUAKE ENGINEERING
RESEARCH CENTER

Effects of Fault Dip and Slip Rake on Near-Source Ground Motions: Why Chi-Chi Was a Relatively Mild *M7.6* Earthquake

Brad T. Aagaard
John F. Hall
Thomas H. Heaton
California Institute of Technology

PEER 2002/12
DEC. 2002

Effects of Fault Dip and Slip Rake on Near-Source Ground Motions: Why Chi-Chi Was a Relatively Mild *M 7.6* Earthquake

Brad T. Aagaard
Postdoctoral Scholar in Geophysics
California Institute of Technology

John F. Hall
Professor of Civil Engineering
California Institute of Technology

Thomas H. Heaton
Professor of Geophysics and Civil Engineering
California Institute of Technology

PEER Report 2002/12
Pacific Earthquake Engineering Research Center
College of Engineering
University of California, Berkeley

December 2002

Abstract

This study focuses on how the fault dip and slip rake angles affect near-source ground motions as faulting transitions from strike-slip motion on a vertical fault to thrust motion on a shallow dipping fault. Ground motions are computed for five fault geometries with different combinations of fault dip and rake angles, and common values for the fault area and the average slip. With the fault reaching the surface in each scenario, the ground motions are dominated by Love and/or Rayleigh waves. The strike-slip faulting tends to generate Love waves, whereas the thrust faulting tends to generate Rayleigh waves. The degree to which the rupture reinforces these waves affects the severity of the shaking. For strike-slip faulting this directivity effect is most pronounced for unilateral rupture, while for thrust faulting it is most pronounced for up-dip rupture. These simulations suggest that the long-period ground motions in the 1999 Chi-Chi earthquake in Taiwan were not as severe as would be expected for other events of the same size with different styles of faulting or a deeper hypocenter.

Acknowledgments

Access to the Hewlett-Packard V-Class computer, located at the California Institute of Technology, was provided by the Center for Advanced Computing Research.

This work was supported in part by the Pacific Earthquake Engineering Research Center through the Earthquake Engineering Research Centers Program of the National Science Foundation under award number EEC-9701568.

Contents

List of Figures

List of Tables

1 Introduction

In the past decade several earthquakes near large urban areas have caused considerable damage, including the 1994 Northridge, California, the 1995 Hyogo-Ken Nanbu (Kobe), Japan, the 1999 Izmit and Duzce, Turkey, and the 1999 Chi-Chi, Taiwan, earthquakes. These earthquakes and their associated ground motion records have increased the awareness of the destructive capability and characteristics of near-source ground motions (e.g., see Olsen and Archuleta [1996], Somerville *et al.* [1997], Hisada *et al.* [1998], Kamae and Irikura [1998], Pitarka *et al.* [1998], Huang *et al.* [2000], Oglesby *et al.* [2000]). The primary factor controlling the size of near-source ground motions is not simply the distance the rupture propagates, but the distance the rupture propagates in the direction of slip. Consequently, the dimensions and the dip angle of the fault, the direction of slip (slip rake angle), and the hypocenter all play critical roles in determining the character and amplitude of near-source ground motions.

Early efforts aimed at understanding near-source ground motions focused on simple numerical models (e.g., Haskell [1969], Archuleta and Frazier [1978], and Archuleta and Hartzell [1981]). More recently, some researchers have focused on specific ground motion recordings [Iwan and Chen, 1994] or damage near a surface rupture [Allen *et al.*, 1998] to infer the characteristics of near-source ground motions. In addition to the modeling efforts mentioned above that attempt to explain damage in past earthquakes, three-dimensional simulations have focused on hypothetical scenarios. Olsen *et al.* [1995] and Graves [1998] examined near-source ground motions for ruptures on the San Andreas fault, and Olsen and Archuleta [1996] considered various scenarios within the Los Angeles area. While these previous studies help to explain patterns of damage in particular earthquakes or what such patterns might be for some future event, they generally do not shed light on the fundamental characteristics of near-source ground motions and how these vary with changes in the seismic source parameters. Dynamic rupture models have improved our understanding of how near-source ground motions develop from the basic features of the rupture process [Olsen *et al.*, 1997; Inoue and Miyatake, 1998; Oglesby *et al.*, 2000; Aagaard *et al.*, 2001], but only a couple of these studies [Oglesby *et al.*, 2000; Aagaard *et al.*, 2001] have systematically explored how the source parameters affect the near-source ground motions.

The research presented in this report complements these two efforts, and other work [Aagaard *et al.*, 2001] that used kinematic source models to systematically examine source parameters and near-source ground motions, by focusing on an event of a specific size and determining how changes in the fault geometry, in particular the fault dip and rake angles, affect the near-source ground motions. The distribution of shaking and the characteristics of the near-source ground motions are examined, as well as how these change in response to variations in the fault dip and slip rake angles for two hypocenters. Several measures of the ground motions are considered, including the horizontal acceleration response spectra, the area where the ground motion exceeds a given level, and the mean maximum amplitude as a function of distance from the fault. A parameters space is selected that includes a scenario that approximates the 1999 Chi-Chi, Taiwan, earthquake in order to explore the role of fault geometry in determining the intensity of the long-period shaking in this earthquake.

2 Earthquake Scenarios

The near-source ground motions are computed for two hypocenters for each of five different pairs of fault dip and slip rake angles. A realistic fault length-to-width ratio is selected for each dip angle. The scenarios vary from a pure strike-slip rupture on a long, narrow fault to a pure thrust rupture on a significantly shorter and wider fault.

2.1 Methodology

We follow the general methodology of our previous work involving simulations of near-source ground motions, and so include in this section only a brief summary of these simulation methods. Aagaard [1999] and Aagaard *et al*. [2001] provide detailed discussions of the methodology. This study improves upon our previous characterizations of the seismic source; in particular, the length scales of the spatial heterogeneity in the final slip are compatible with those found in kinematic source inversions, and the rupture speed is allowed to vary as a function of the direction of propagation relative to the direction of slip.

The three-dimensional domain is discretized using linear tetrahedral finite elements. This transforms the three-dimensional dynamic elasticity equation,

$$\lambda u_{k,kj}\delta_{ij} + \mu(u_{i,jj} + u_{j,ij}) = \rho\ddot{u}_i \tag{2.1}$$

into a matrix differential equation,

$$[M]\{\ddot{u}(t)\} + [C]\{\dot{u}(t)\} + [K]\{u(t)\} = \{F(t)\}, \tag{2.2}$$

where $[M]$ denotes the mass matrix, $[C]$ denotes the damping matrix, $[K]$ denotes the stiffness matrix, $\{F(t)\}$ denotes the force vector at time t, and $\{u(t)\}$ denotes the displacement vector at time t. The discretization of the finite-element model limits the simulation to wave propagation for waves with periods of 2.0 sec and longer.

Anelastic attenuation is not included because it has little effect on long-period near-source ground motions, so the only contribution to the damping matrix comes from the absorbing boundaries on the lateral sides and bottom of the domain. These absorbing boundaries prevent waves from reflecting off the truncated sides of the domain and contaminating the solution.

The earthquake is modeled by creating dislocations in the finite-element model that mimic the slip on a fault. In the scenarios discussed here, the slip time history is specified at each point on the fault, where the time history follows the integral of Brune's far-field time function with the final slip and peak slip rate as parameters.

2.2 Simulation Domain

All of the scenarios use the same geometry for the domain. In each case the domain is 160 km long, 80 km wide, and 40 km deep as shown in figure 2.1. The fault intersects the ground surface and strikes to the north. The center of the fault lies 70 km north and 40 km east with respect to the axes shown in the figure.

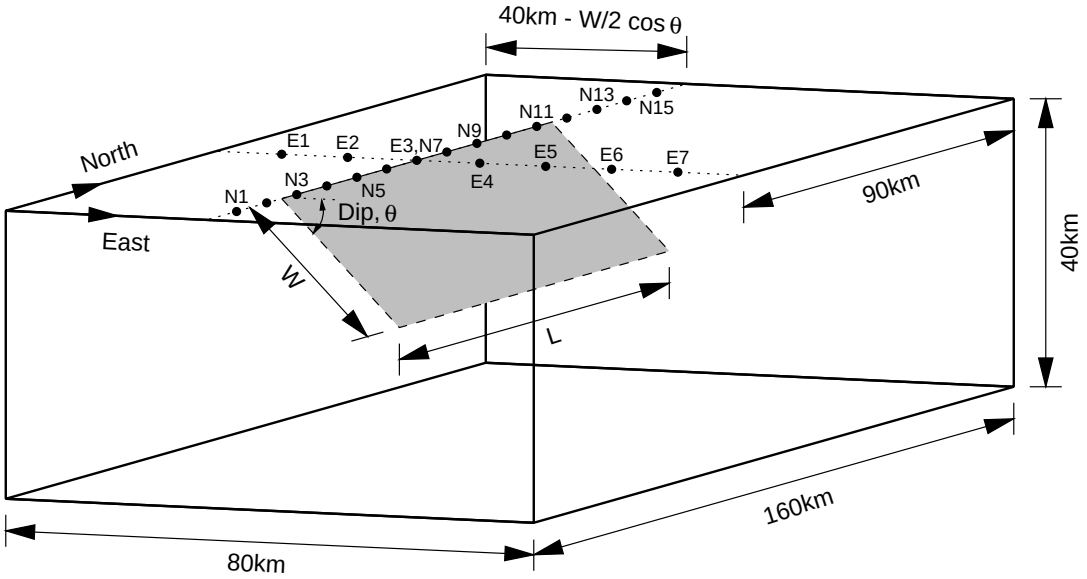

Fig. 2.1. Geometry of the simulation domain. The fault has a dip angle of θ, a length of *L*, and a width of *W*. The center of the fault lies 10 km south of the center of the domain. The dotted line running east-west sits above the center of the fault, while the dotted line running north-south intersects the fault trace. The filled circles along these two dotted lines identify sites (N1 through N15 and E1 through E7) used in subsequent sections of this report. The nominal spacing between sites is 10 km with those along the fault trace sitting on the hanging wall.

The material properties vary only as a function of depth as illustrated in figure 2.2. This set of material properties represents the average variations in Taiwan and corresponds to the variation in a region without a deep sedimentary basin [Ma *et al*., 1996; Ma *et al*., 2001].

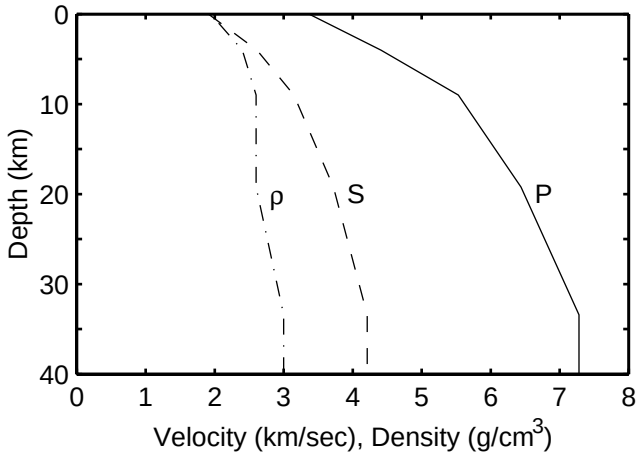

Fig. 2.2. Dilatational wave speed (P), shear wave speed (S), and mass density (ρ) as a function of depth.

2.3 Earthquake Source Parameters

Table 2.1 gives the five pairs of fault dip and slip rake angles along with the fault lengths and widths for the different fault geometries. Figure 2.3 illustrates how the values for these parameters define the geometry of the fault and the direction of the slip. For the five scenarios we chose fault dip angles uniformly distributed between 90 and 30 degrees with rake angles uniformly distributed between 0 and 90 degrees. Similarly, the lengths of the faults decreased linearly from 120 km long to 80 km long while maintaining an area of 2400 km^2. A fault area of 2400 km^2 was chosen so that the scenario with a fault dip angle of 30 degrees would roughly match the geometry of the 1999 Chi-Chi earthquake. Inversions for the source characteristics indicate that this earthquake had a rupture length of between 80 km and 100 km, a rupture width of between 30 m and 40 km, and a dip angle of 20 degrees to 30 degrees [Huang *et al*., 2000; Ma *et al*., 2000; Johnson *et al*., 2001; Ji *et al*.,]. The length to width ratios and slip rake angles both fall within the ranges of realistic values for all five fault dip angles.

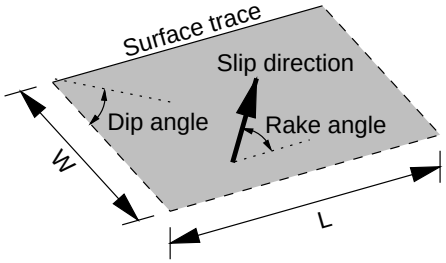

Fig. 2.3. Illustration of how the slip rake angle and the fault length, width, and dip angle control the geometry of the fault and the slip direction.

Table 2.1. Geometry of the fault for each pair of dip and rake angles. The fault geometry smoothly transitions from pure strike-slip motion on a long, narrow fault to pure thrust motion on a much shorter, wider fault.

Dip Angle (deg)	Rake Angle (deg)	Fault Length (km)	Fault Width (km)
90	0.0	120	20
75	22.5	110	22
60	45.0	100	24
45	67.5	90	27
30	90.0	80	30

Based on the regression relations of Wells and Coppersmith [1994] between the fault geometry and average slip coupled with these fault dimensions, a common average slip of 2.9 m was chosen for the scenarios in this report. This average slip is smaller than the average slip estimated for the Chi-Chi earthquake, so the hypothetical fault with a dip angle of 30 degrees and the selected material properties has a moment magnitude of only 7.4 compared to the moment magnitude of 7.6–7.7 estimated for the Chi-Chi earthquake. For each fault the slip rake angles are uniform and remain constant during the rupture. A uniform peak slip rate of 2.0 m/sec was used in the slip time history, which for final slips of around 3 m gives slip durations compatible with those found in kinematic source inversions [Heaton, 1990; Somerville *et al*., 1997]. Table 2.2 lists the source parameters, which remain constant across all of the scenarios.

Table 2.2. Seismic source parameters common to all scenarios. The rupture speed is set relative to the local shear wave speed, v_s.

Parameter	Value
Average Slip	2.9 m
Peak Slip Rate	2.0 m/sec
Rupture Speed, v_r	85% v_s parallel to slip 68% v_s perpendicular to slip

2.3.1 Distribution of Slip

The distributions of final slip were created to have the same wavenumber squared falloff in amplitude over the fault as what is generally observed in distributions of slip from source inversions

[Somerville *et al*., 1997]. Starting with a uniform random distribution on a 1.0 km uniform grid (which is coarser than the node spacing in the finite-element model), we low-pass filter along the fault strike and then along the dip using a first-order Butterworth filter. We also taper the slip along the buried edges of the fault. Because the length and width of the faults differ for each dip angle, we follow the above procedure to create separate distributions of slip for each fault geometry. While all of the distributions have an average slip of 2.9 m, the maximum slip ranges from 5.7 m to 7.1 m across the five fault geometries because we started with different random distributions for each fault geometry. Nevertheless, the spatial heterogeneity in the distributions contain the same same falloff in amplitude with the inverse of the wavenumber squared. Figure 2.4 shows the distribution of final slip for the fault with a dip angle of 60 degrees.

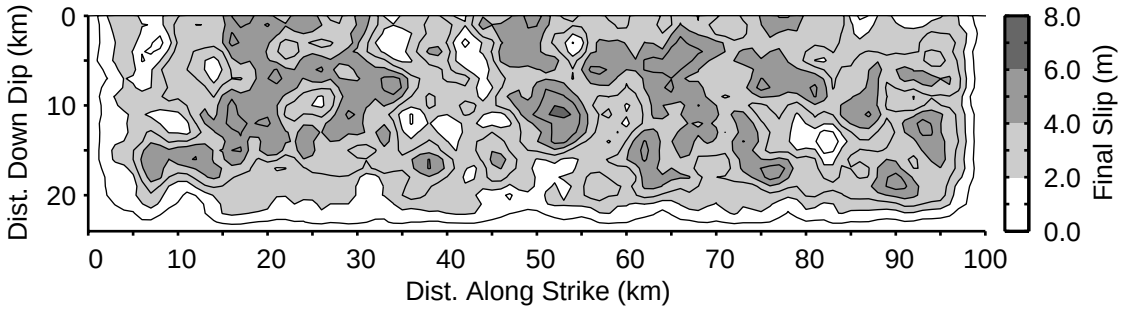

Fig. 2.4. Distribution of final slip for the fault with a dip angle of 60 degrees. The distribution is a low-pass filtered random distribution, where the amplitude of the spatial heterogeneity over the fault falls off as the inverse of the wavenumber squared.

2.3.2 Rupture Speed

The rupture speed determines when slip begins at each point on the fault. The rupture speed was set relative to the local shear wave speed. Different rupture speeds were allowed as a function of the direction of propagation relative to the direction of slip based on numerous observations of this phenomenon in dynamic rupture simulations; the rupture speed propagates slightly slower in the direction perpendicular to slip compared to the direction parallel to slip [Andrews, 1976; Day, 1982; Madariaga *et al*., 1998; Aagaard *et al*., 2001]. Instead of an isotropic rupture speed, the rupture speed was independently specified relative to the local shear wave speed in the mode-II direction (parallel to the slip direction) and in the mode-III direction (perpendicular to the slip direction) as illustrated in figure 2.5.

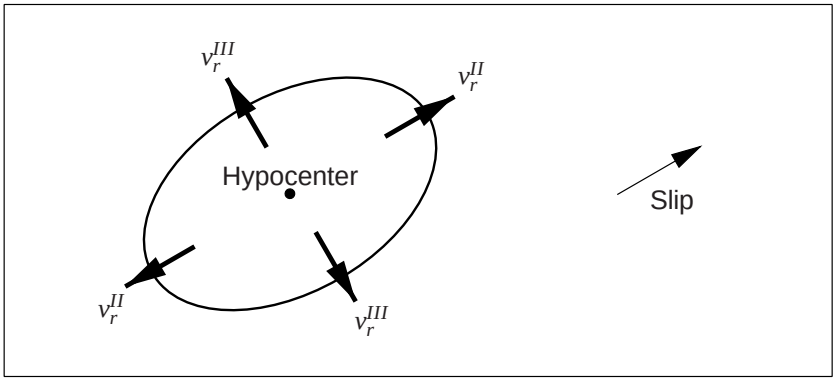

Fig. 2.5. Diagram illustrating that the rupture speed is set independently in the mode-II (v_r^{II}) and mode-III directions (v_r^{III}). The ellipse identifies the rupture front at some point in time and the large arrows indicate the propagation direction of the rupture on the fault (rectangle).

2.3.3 Hypocenters

Figure 2.6 shows the two hypocenters considered for each dip angle of the fault. Hypocenter HA sits mid-depth at the southern quarter point of the fault and corresponds to a highly unilateral rupture, while hypocenter HB sits 5.0 km up-dip from the bottom center of the fault and corresponds to the bilateral case with more up-dip rupture. Due to the shear wave radiation pattern, the near-source ground motions are most accentuated for ruptures that propagate predominantly in the mode-II direction (propagation parallel to the slip direction) [Somerville *et al*., 1997; Aagaard *et al*., 2001]. For strike-slip faulting the rupture propagates mostly in the mode-II direction (parallel to slip) for both hypocenters. On the other end of the spectrum, for pure thrust faulting the rupture propagates primarily in the mode-III direction for hypocenter HA with very little propagation in the mode-II direction; for pure thrust faulting and hypocenter HB the amount of rupture in the mode-II direction increases significantly.

2.4 Scenario Nomenclature

The name of each scenario corresponds to the dip angle of the fault and the hypocenter. For example, dip90HA refers to the scenario where the fault has a dip angle of 90 degrees and the rupture begins at hypocenter HA. Similarly, dip45HB refers to the scenario where the fault has a dip angle of 45 degrees and the rupture begins at hypocenter HB.

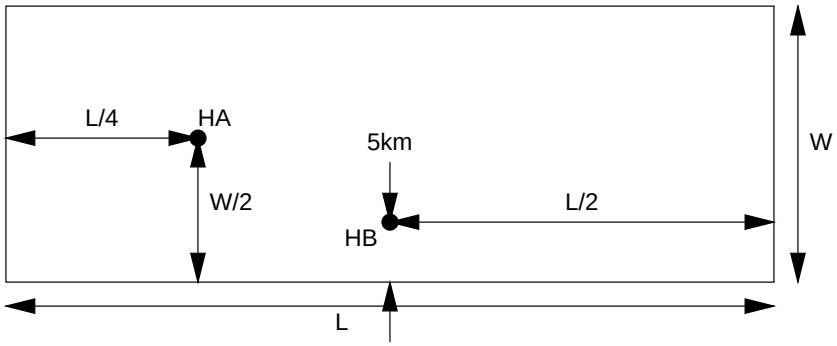

Fig. 2.6. Hypocenters HA and HB relative to the fault surface with length L and width W. Hypocenter HA lies mid-depth at a quarter point and hypocenter HB lies midway along strike 5 km up-dip from the bottom of the fault. Hypocenter HA approximates the hypocenter in the Chi-Chi earthquake.

3 Results

In this chapter the results of the simulations are analyzed and the trends in the behavior are illustrated with figures selected from a subset of the various scenarios. Appendix A discusses the computational requirements of the simulations, and appendices B–D contain full complementary sets of figures.

3.1 Overview of Rupture Behavior and Ground Motions

We begin by examining how the basic characteristics of the rupture behavior and resulting ground motions change with the fault dip and slip rake angles by using data from scenarios dip90HA (pure strike-slip faulting with predominantly unilateral rupture) and dip45HB (oblique faulting with predominantly bilateral rupture). The snapshots of the slip rate on the fault surface in figures 3.1 and 3.2 illustrate the three dominant characteristics of the prescribed rupture behavior. (1) The specified rupture speed varies with the direction of propagation relative to the slip direction. In the direction of slip (mode-II direction), the rupture propagates at a speed of 85% of the local shear wave speed, while in the direction perpendicular to slip (mode-III direction), the rupture propagates 20% slower at a speed of 68% of the local shear wave speed. (2) The rupture speed remains at a constant fraction of the local shear wave speed, so that it slows down as the rupture encounters softer material near the ground surface. (3) The shape of the trailing edge changes as the rupture encounters variations in the final slip because the uniform peak slip rate of $2.0\,\mathrm{m/sec}$ results in longer rise times in areas with larger slips. As discussed in section 2.3, these features are consistent with the behavior observed from kinematic source inversions and dynamic rupture simulations.

Figure 3.1 shows the simplest case of rupture behavior: pure strike-slip motion on a vertical fault. The rupture propagates fastest along the strike of the fault. As the dip angle of the fault decreases and the rake angle of slip increases so that it has a larger vertical component, the rupture speed along the strike decreases, while the rupture speed up-dip increases. For the case of the fault at a dip angle of 45 degrees and a rake angle of 67.5 degrees (figure 3.2), the fastest rupture speed

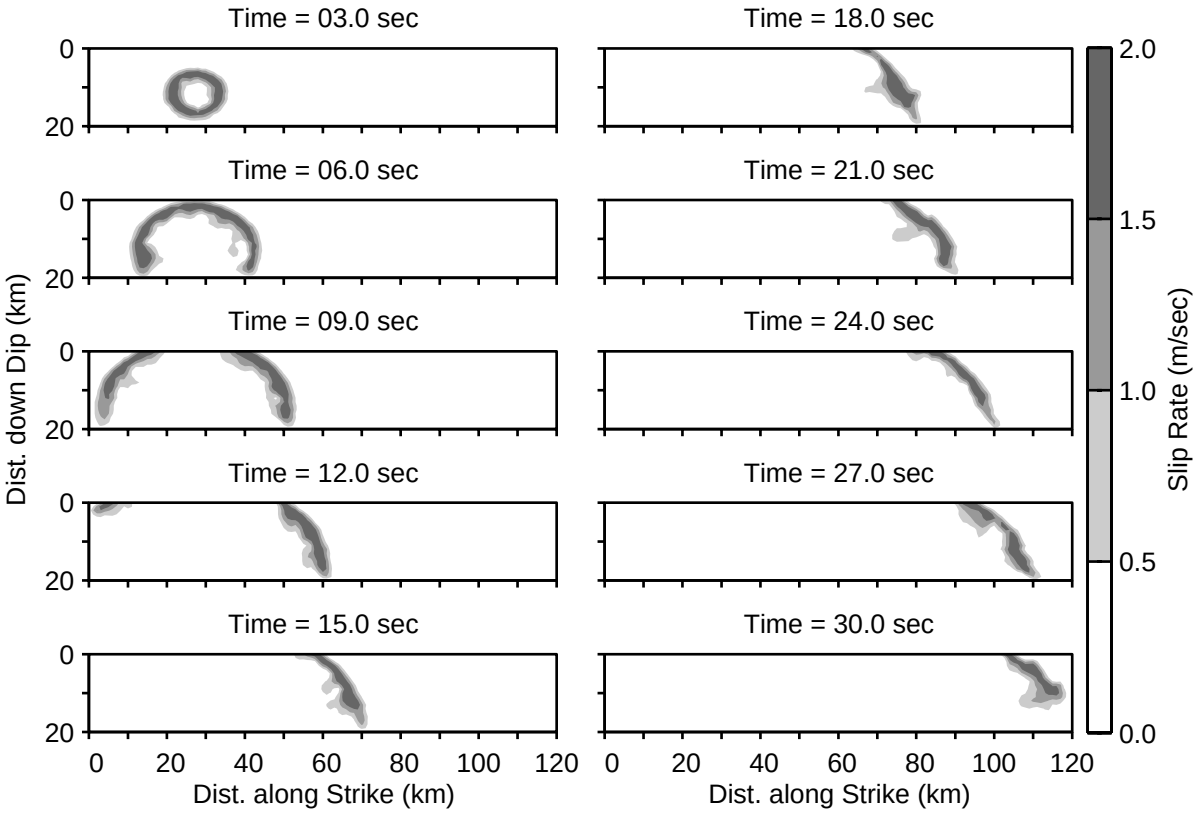

Fig. 3.1. Snapshots of slip rate on the fault surface for scenario dip90HA. The rupture propagates at 85% of the shear wave speed in the direction of slip (strike direction) and 20% slower in the direction perpendicular to slip (dip direction). The variation in the shear wave speed with depth alters the shape of the initially elliptic rupture front, while the uniform peak slip rate and heterogeneous distribution of slip create the large fluctuations in shape of the trailing edge of the rupture.

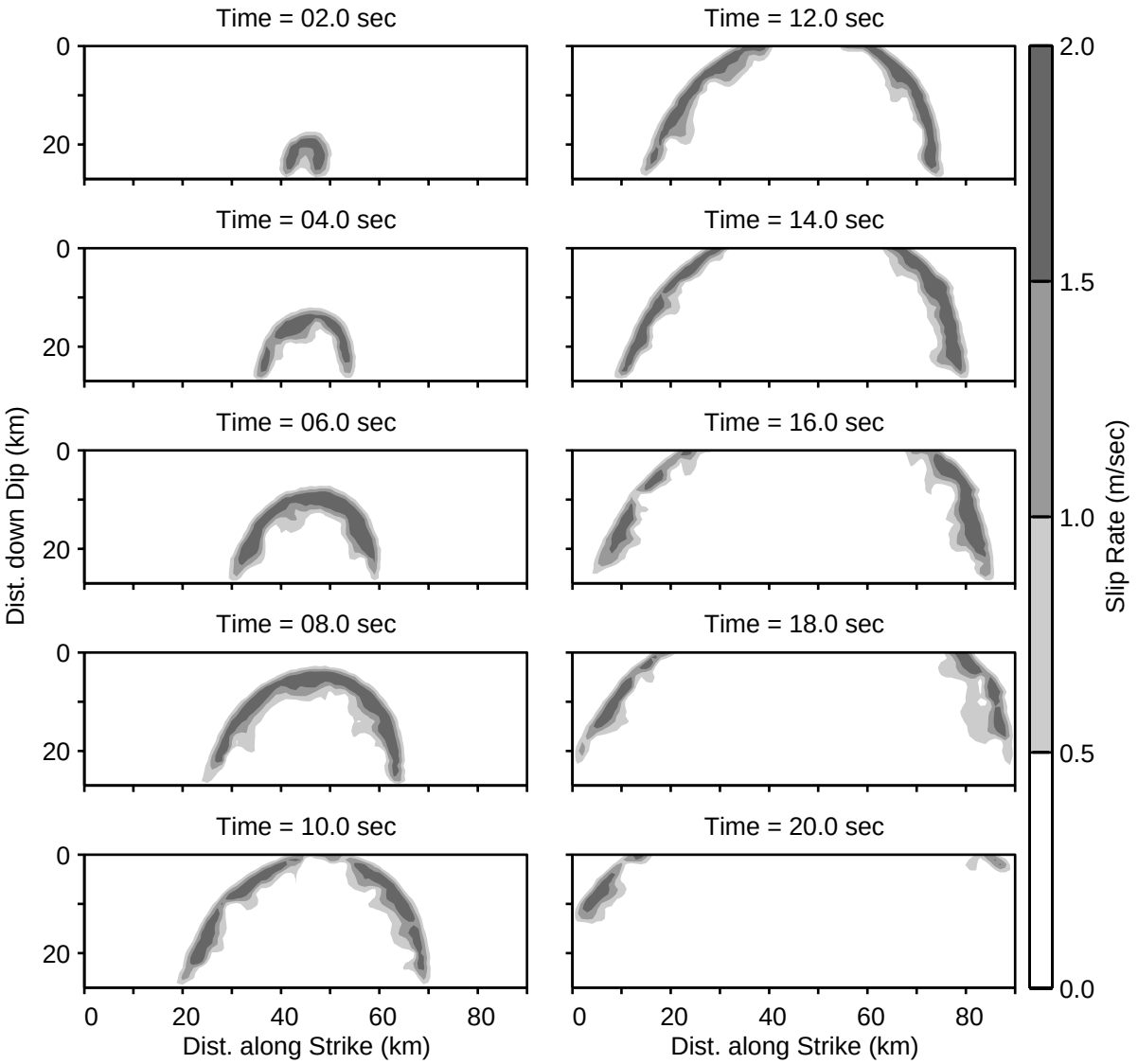

Fig. 3.2. Snapshots of slip rate on the fault surface for scenario dip45HB. The rupture propagates at 85% of the shear wave speed in the direction of slip (67.5 degrees up-dip from strike) and 20% slower in the direction perpendicular to slip (22.5 degrees down-up from strike). The variation in the shear wave speed with depth alters the shape of the initially elliptic rupture front, while the uniform peak slip rate and heterogeneous distribution of slip create the large fluctuations in shape of the trailing edge of the rupture.

occurs 22.5 degrees off the up-dip and down-dip directions. This creates the asymmetry in the snapshots of slip rate for the centrally located hypocenter.

Owing to the existence of surface rupture in the layered medium, surface waves in the form of combinations of Love and Rayleigh waves dominate the long-period ground motions. Figure 3.3 displays snapshots of the amplitude of the particle velocities on the ground surface for the vertical fault with hypocenter HA. As the rupture propagates, large-amplitude Love waves with amplitudes approaching $2.0\,\mathrm{m/sec}$ form in the region where the propagation direction generally coincides with the slip direction, which in this case is north of the epicenter. The particle motion for these waves is in the east-west direction (normal to the fault). The Love wave amplitudes generally build along the length of the fault as the rupture reinforces the waves, and then begin steadily decreasing upon reaching the northern tip of the fault. The heterogeneous distribution of slip causes the reinforcement of the Love waves to be haphazard, so that the amplitudes undergo minor fluctuations as they grow.

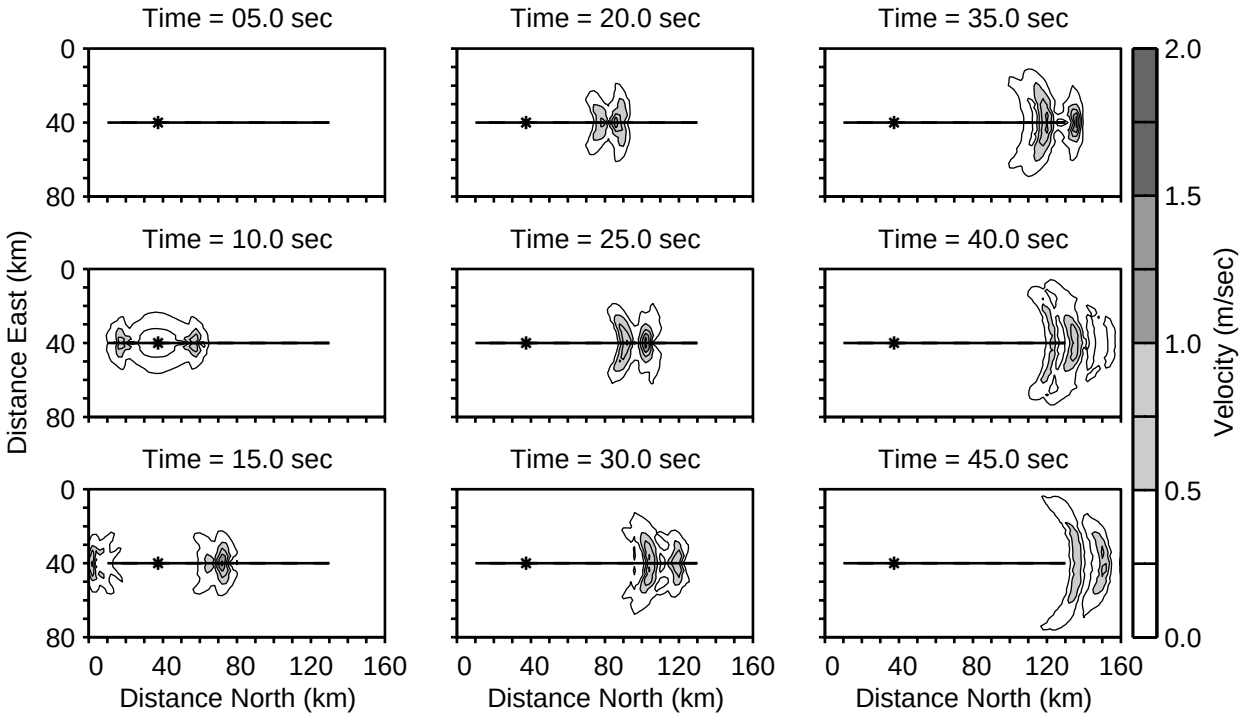

Fig. 3.3. Snapshots of the amplitude of the particle velocity on the ground surface for scenario dip90HA. The solid line indicates the surface trace of the fault and the asterisk denotes the hypocenter. Large-amplitude Love waves propagating along the fault away from the epicenter dominate the motions on the ground surface.

As the dip angle of the fault decreases and the vertical component of slip increases, the rupture generates Love waves less effectively and becomes more effective at generating Rayleigh waves. Figure 3.4 shows snapshots of the particle velocity for scenario dip45HB. The rotation of the slip direction toward the dip direction results in reinforcement of the SV waves (shear waves with particle motion in the vertical direction) emanating from an angle of 45 degrees with respect to the slip direction, which produce Rayleigh waves as they hit the ground surface. Consequently, the largest Rayleigh waves (the amplitudes are near $1.5\,\mathrm{m/sec}$) occur northwest of the epicenter; the particle motions are retrograde with the largest horizontal component in the northwest-southeast direction.

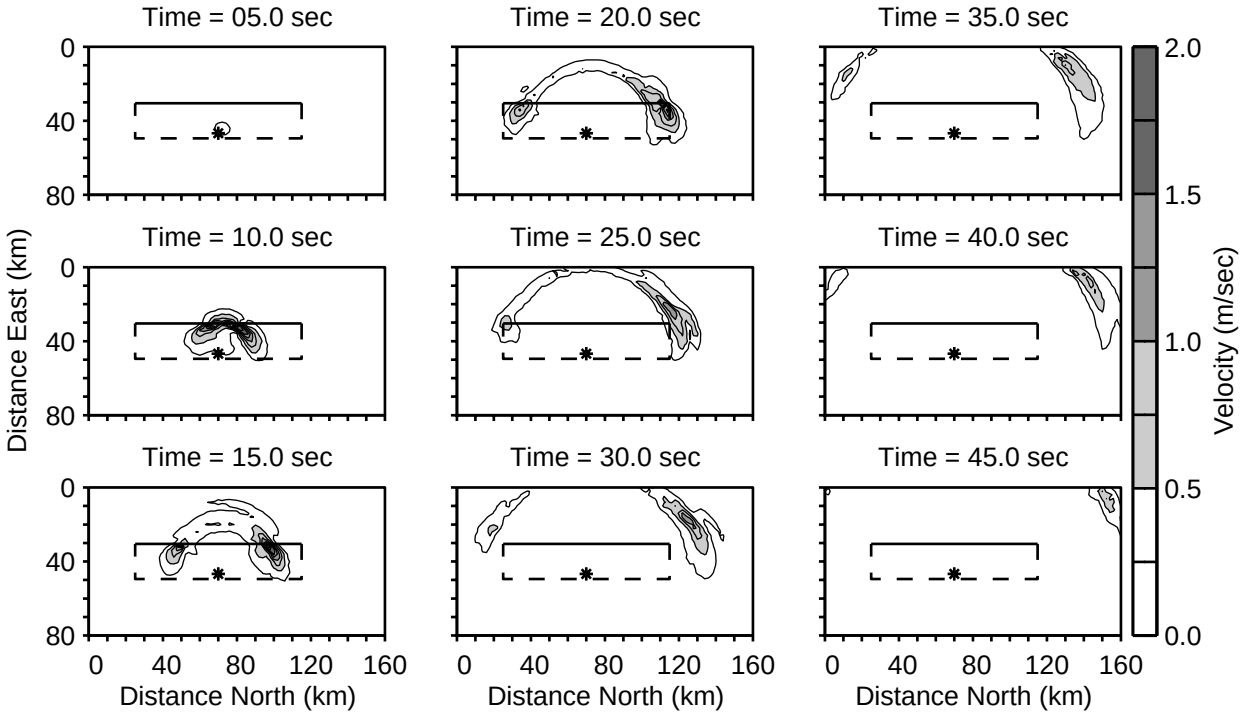

Fig. 3.4. Snapshots of the amplitude of the particle velocity on the ground surface for scenario dip45HB. The solid line indicates the surface trace of the fault, the dashed line shows the projection of the buried edges of the fault, and the asterisk denotes the hypocenter. Rayleigh waves propagating toward the northwest are responsible for the largest amplitude motions.

3.2 Maximum Displacements and Velocities

Next examined are the maximum displacements and velocities on the ground surface because they provide a good measure of the intensity of the long-period shaking. Both the maximum

amplitude of the motion and the maximum peak-to-peak amplitude of the motion are considered. Figure 3.5 highlights the differences between these measures for three definitive cases. (1) For a single-sided pulse the maximum amplitude and maximum peak-to-peak amplitude are the same. (2) For a double-sided pulse the maximum peak-to-peak amplitude can be up to twice the maximum amplitude. (3) For a fluctuating variation the maximum peak-to-peak amplitude can be smaller than the maximum amplitude.

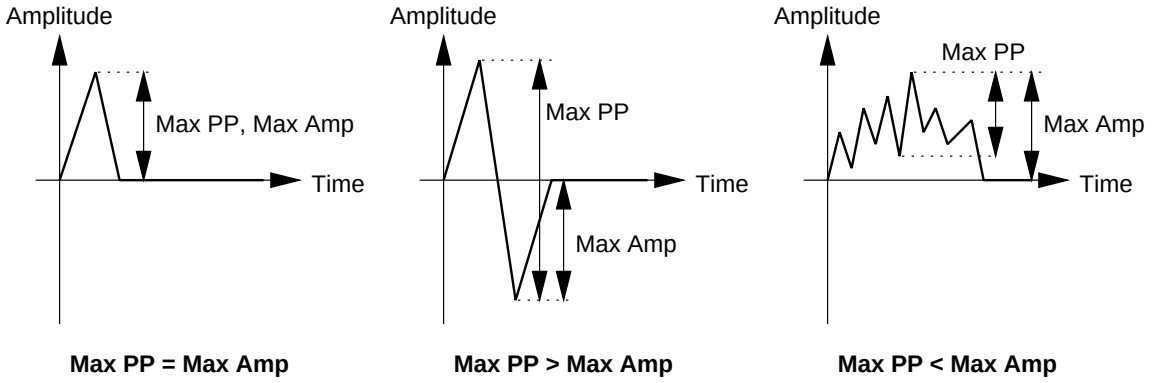

Fig. 3.5. Three examples illustrating how the maximum peak-to-peak amplitude compares to the maximum amplitude. For a single-sided pulse (left) the maximum peak-to-peak amplitude is equal to the maximum amplitude. For a double-sided, symmetric pulse (center) the maximum peak-to-peak amplitude is twice the maximum amplitude. For a fluctuating time history, the maximum peak-to-peak amplitude can be much smaller than the maximum amplitude.

In practice, the greatest difference between these two measures of amplitude occurs for the case of double-sided, symmetric displacement or velocity pulses, as shown in figure 3.6. A displacement ramp and the corresponding single-sided velocity pulse roughly approximate the ground motion at a location with a static offset. In this case, there is no difference between the maximum peak-to-peak amplitudes and the maximum amplitudes. A single-sided displacement pulse and the corresponding double-sided velocity pulse roughly approximate the ground motion at a location without a static offset and no surface waves. Whereas the maximum displacement equals the maximum peak-to-peak displacement, the maximum peak-to-peak velocity exceeds the maximum velocity by up to a factor of two. Finally, a double-sided displacement pulse and the corresponding velocity pulses roughly approximate the ground motion at a location with large-amplitude surface waves and no static offset. In this case, the maximum peak-to-peak displacement and velocity amplitudes can both be up to twice the maximum amplitudes. The peak-to-peak velocity often closely correlates with structural response.

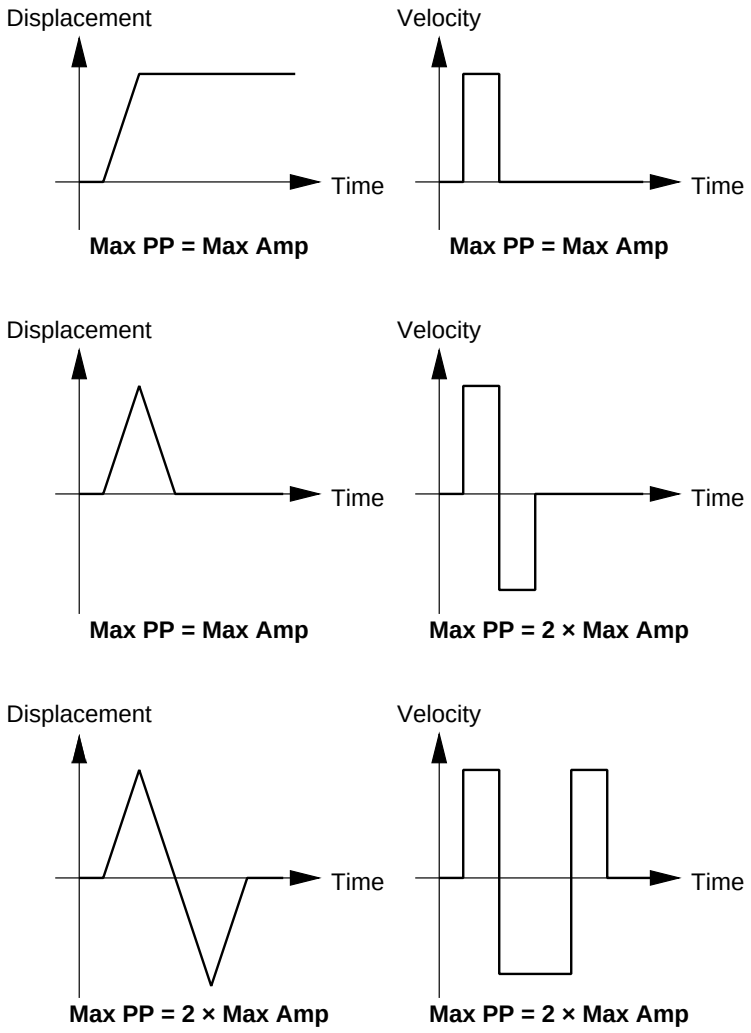

Fig. 3.6. Illustration of how the peak-to-peak displacement and velocity amplitudes compare to the maximum amplitudes for three different types of ground motions: a displacement ramp and corresponding single-sided velocity pulse (top), a single-sided displacement pulse and corresponding double-sided velocity pulse (middle), and a double-sided displacement pulse and corresponding velocity pulses (bottom). Except for the case of double-sided displacements, which are generally associated with surface waves, the maximum peak-to-peak displacements match the maximum displacements. On the other hand, the maximum peak-to-peak velocities exceed the maximum velocities except for the case in which there is a large static offset.

In scenario dip90HA the maximum horizontal displacements and velocities increase along the strike of the fault north and south of the epicenter as shown in figure 3.7. This effect is much more pronounced north of the epicenter because the rupture extends much further in this direction compared to south of the epicenter. The amplitudes also decay rapidly with distance away from the surface trace of the fault. The maximum horizontal displacement is 2.6 m, and the maximum horizontal velocity is 1.6 m/sec.

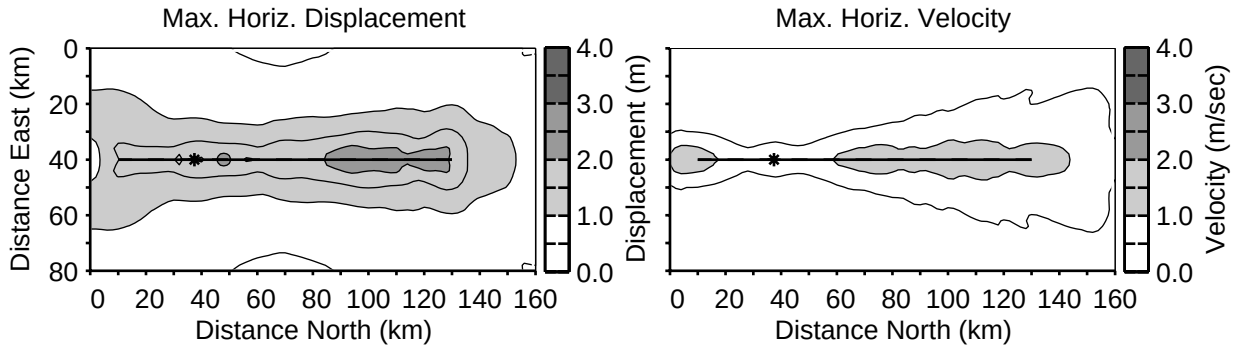

Fig. 3.7. Maximum amplitude of the horizontal displacements and velocities on the ground surface for scenario dip90HA. The thick solid line shows the surface trace of the fault and the asterisk identifies the epicenter. The maximum displacements and velocities generally increase along the fault away from the epicenter and then decrease steadily past the ends of the fault.

Comparing the maximum displacements and velocities in the epicentral region for scenario dip90HA in figure 3.7 with the maximum peak-to-peak displacements and velocities in figure 3.8, we find that the maximum peak-to-peak amplitudes exceed the maximum amplitudes at most locations. North of the north tip of the fault where the Love waves dominate the motions and the static displacements are small, the maximum peak-to-peak displacements exceed the maximum displacements by nearly a factor of two. The maximum peak-to-peak velocities are generally close to twice the maximum velocities nearly everywhere, indicating that double-sided motions dominate the velocity time histories. We find a maximum peak-to-peak displacement of 3.4 m and a maximum peak-to-peak velocity of 2.6 m/sec.

As the dip of the fault decreases and the vertical component of slip increases, the pattern of shaking becomes much more asymmetric with two clear features: (1) the ground displacements on the hanging-wall (above the fault) increase and closely resemble the distribution of slip, and (2) the strongest shaking remains concentrated in the region with the maximum directivity. These trends are visible in figures 3.9 and 3.10, which display the maximum horizontal displacements and velocities and the maximum peak-to-peak horizontal displacements and velocities, respectively, for scenario dip60HA. The steep dip of the fault and the rake angle of 45 degrees lead to large Love

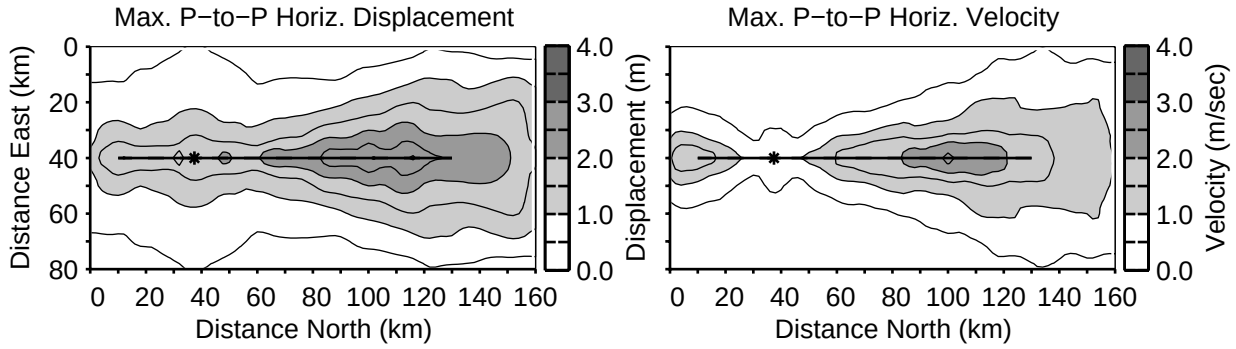

Fig. 3.8. Maximum peak-to-peak horizontal displacements and velocities on the ground surface for scenario dip90HA. The thick solid line shows the surface trace of the fault and the asterisk identifies the epicenter. The maximum peak-to-peak displacements display a greater increase along the strike of the fault than the maximum displacements, while the maximum peak-to-peak velocities are about twice the maximum velocities over nearly the entire ground surface.

and Rayleigh waves that propagate toward the northwest. As a result, a large region emanating off to the northwest from the northern end of the fault experiences maximum peak-to-peak motions exceeding 2.0 m and 2.0 m/sec. As in the case of scenario dip90HA, the maximum peak-to-peak displacements are about twice the maximum displacement around the north end of the fault, while the maximum peak-to-peak velocities are significantly larger than the maximum velocities over nearly all of the ground surface.

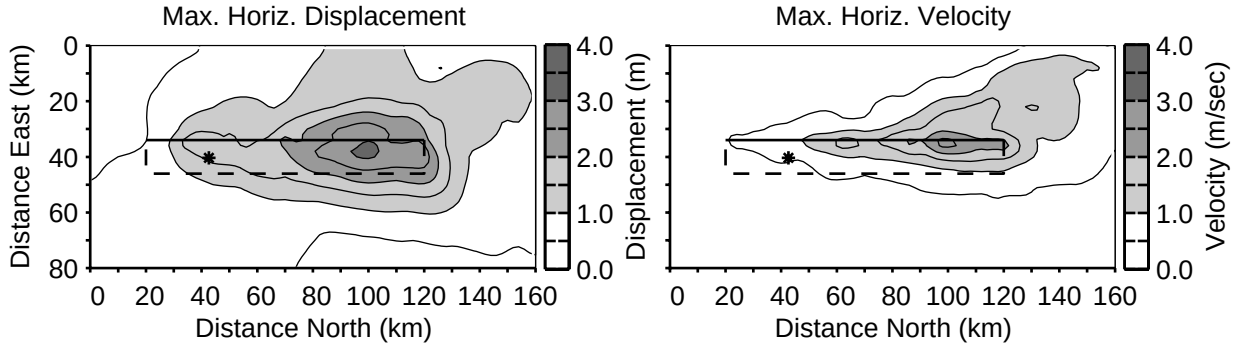

Fig. 3.9. Maximum horizontal displacements and velocities on the ground surface for scenario dip60HA. The thick solid line shows the surface trace of the fault, the thick dashed line indicates the surface projection of the buried edges of the fault, and the asterisk identifies the epicenter. The maximum displacements and velocities generally increase along the fault away from the epicenter with a large region of intense shaking extending to the northwest.

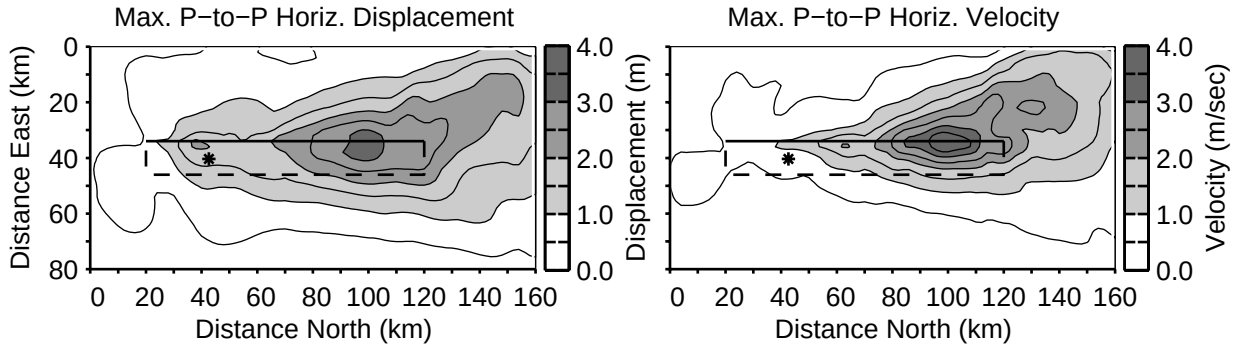

Fig. 3.10. Maximum peak-to-peak horizontal displacements and velocities on the ground surface for scenario dip60HA. The thick solid line shows the surface trace of the fault, the thick dashed line indicates the surface projection of the buried edges of the fault, and the asterisk identifies the epicenter. The maximum peak-to-peak displacements display a greater increase along the strike of the fault than the maximum displacements, while the maximum peak-to-peak velocities are about twice the maximum velocities over nearly the entire ground surface.

With hypocenter HA, in the transition from strike-slip motion to thrust motion, the rupture continues to propagate mostly along the strike of the fault so that the rupture direction becomes less aligned with the slip direction. In other words, the rupture switches from propagating in the mode-II direction to propagating in the mode-III direction. In our limiting case where the fault dip angle is 30 degrees with pure thrust faulting, the inability of the rupture to effectively reinforce Love or Rayleigh waves leads to much smaller ground velocities (figures 3.11 and 3.12). While the maximum velocities do reach $1.4\,\mathrm{m/sec}$ at one location, the maximum peak-to-peak velocity is only $1.7\,\mathrm{m/sec}$. On the hanging wall side of the fault, the maximum displacements do remain large although they are dominated by the static displacement, which is consistent with equal values of $3.1\,\mathrm{m}$ for the maximum amplitude and the maximum peak-to-peak amplitude.

However, moving the hypocenter toward the bottom center of the fault increases the amount of mode-II rupture for the thrust motion cases. Of course, it has the opposite effect for the case of pure strike-slip motion on a vertical fault where the distance over which the rupture effectively reinforces waves decreases by one third. Thus, for the steeply dipping faults with mostly horizontal slip, the ground motions decrease in most locations when the hypocenter moves from HA to HB, while for shallow dipping faults with a large thrust component of slip, the ground motions increase at many locations for the deeper hypocenter. Figures 3.13 and 3.14 display the maximum peak-to-peak displacements and velocities for scenarios dip60HB and dip30HB. For the 60 degree dipping fault with a slip rake angle of 45 degrees, the maximum peak-to-peak velocity is 33% smaller for hypocenter HB compared to hypocenter HA. On the other hand, for the 30 degree dipping fault

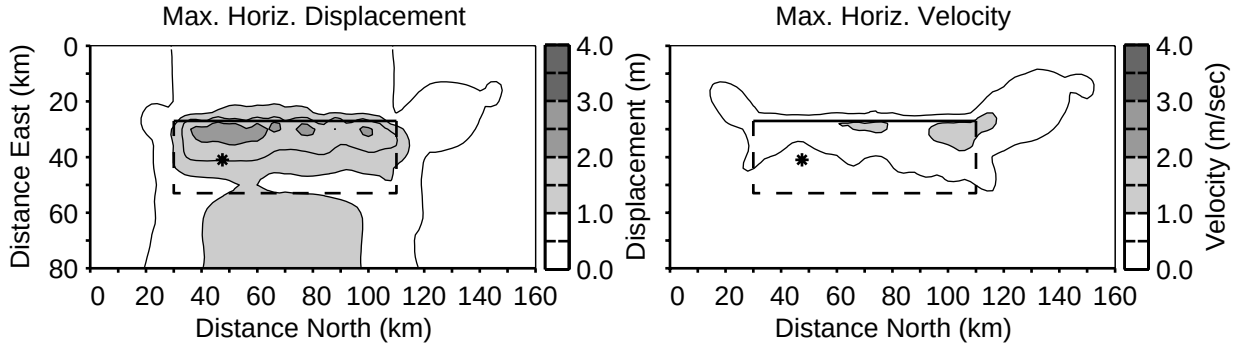

Fig. 3.11. Maximum horizontal displacements and velocities on the ground surface for scenario dip30HA. The thick solid line shows the surface trace of the fault, the thick dashed line indicates the surface projection of the buried edges of the fault, and the asterisk identifies the epicenter. The predominantly mode-III rupture does not efficiently reinforce the Love and Rayleigh waves, which results in much smaller ground motions relative to the other scenarios.

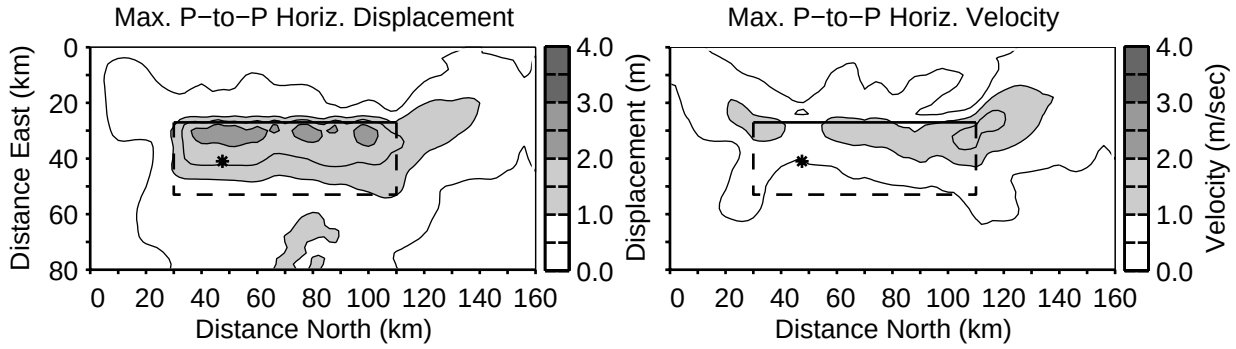

Fig. 3.12. Maximum peak-to-peak horizontal displacements and velocities on the ground surface for scenario dip30HA. The thick solid line shows the surface trace of the fault, the thick dashed line indicates the surface projection of the buried edges of the fault, and the asterisk identifies the epicenter. The mostly mode-III rupture leads to mostly one-sided ground motions with maximum peak-to-peak amplitudes only slightly larger than the maximum amplitude.

with a slip rake angle of 90 degrees (pure thrust), the maximum peak-to-peak velocity *increases* by 30% when the hypocenter moves from HA to HB.

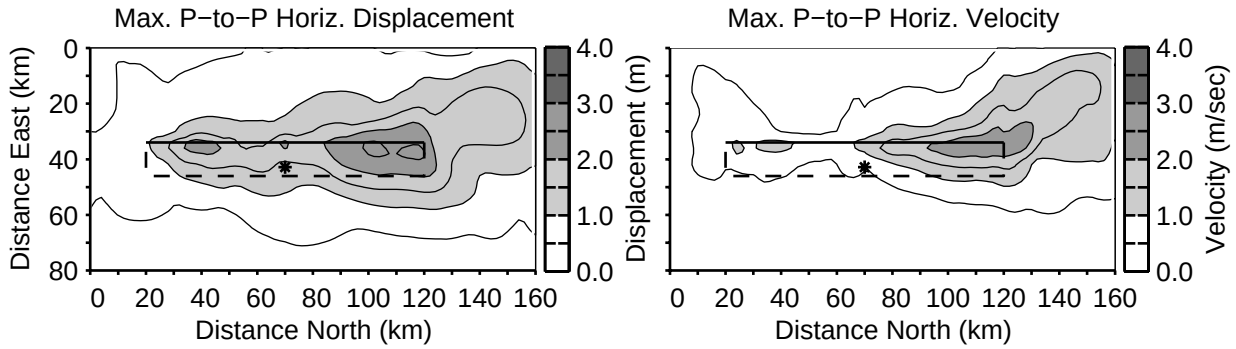

Fig. 3.13. Maximum peak-to-peak horizontal displacements and velocities on the ground surface for scenario dip60HB. The thick solid line shows the surface trace of the fault, the thick dashed line indicates the surface projection of the buried edges of the fault, and the asterisk identifies the epicenter. Moving the hypocenter toward the bottom center of the fault reduces the reinforcement of the Love and Rayleigh waves, resulting in significantly smaller ground motions compared to when the hypocenter sits at the southern quarter point of the fault.

Tables 3.1 and 3.2 give the maximum displacements and velocities in the east-west, north-south, and vertical directions as well as the maximum in any horizontal direction for each of the ten scenarios. Plots of the maximum peak-to-peak horizontal displacements and velocities for all ten scenarios are compiled in appendix B. In all ten scenarios the ground motions are large with the maximum displacements exceeding 2.0 m and the maximum peak-to-peak velocities exceeding 1.7 m/sec.

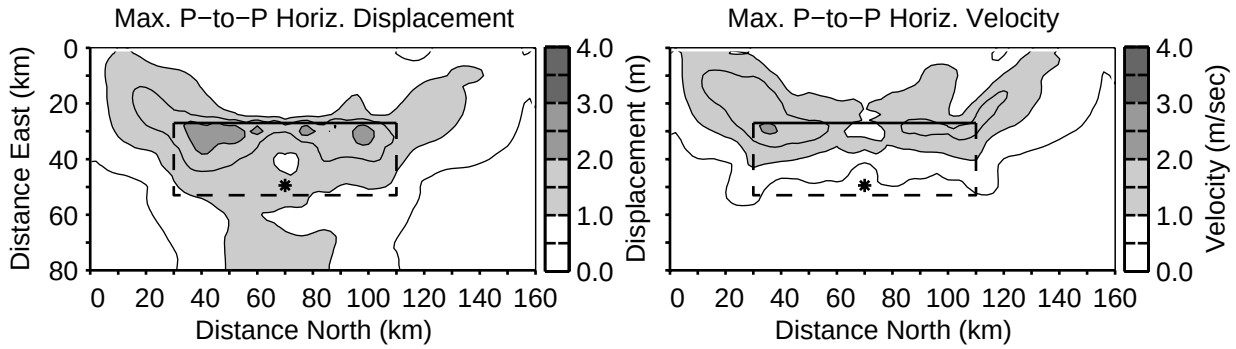

Fig. 3.14. Maximum peak-to-peak horizontal displacements and velocities on the ground surface for scenario dip30HB. The thick solid line shows the surface trace of the fault, the thick dashed line indicates the surface projection of the buried edges of the fault, and the asterisk identifies the epicenter. Moving the hypocenter from mid-depth at the southern quarter point of the fault to a position slightly up-dip from the bottom center of the fault yields a longer up-dip, mode-II rupture which allows more reinforcement of the Rayleigh waves and, consequently, larger ground motions.

Table 3.1. Maximum displacements and maximum peak-to-peak displacements in the east-west, north-south, horizontal, and vertical directions for each scenario.

Scenario	Max. Disp.				Max. P-to-P Disp.			
	EW (m)	NS (m)	Horiz. (m)	Vert. (m)	EW (m)	NS (m)	Horiz. (m)	Vert. (m)
dip90HA	2.0	2.6	2.6	0.76	2.9	2.6	3.4	0.74
dip90HB	1.8	2.6	2.6	0.74	2.4	2.6	2.8	0.76
dip75HA	3.1	3.1	3.3	1.4	3.4	3.1	3.6	1.4
dip75HB	2.1	3.1	3.1	1.3	2.6	3.2	3.2	1.4
dip60HA	3.1	2.8	3.2	2.9	3.5	2.9	3.5	3.0
dip60HB	2.2	2.8	2.8	2.5	2.6	3.1	3.1	2.8
dip45HA	2.1	2.2	2.2	3.5	2.1	2.2	2.3	3.7
dip45HB	2.1	2.3	2.3	3.2	2.1	2.3	2.4	3.4
dip30HA	3.1	1.4	3.1	2.5	3.1	1.7	3.1	2.7
dip30HB	3.1	1.7	3.1	2.8	3.0	1.9	3.0	2.9

Table 3.2. Maximum velocities and maximum peak-to-peak velocities in the east-west, north-south, horizontal, and vertical directions for each scenario.

Scenario	Max. Velocity				Max. P-to-P Velocity			
	EW (m/sec)	NS (m/sec)	Horiz. (m/sec)	Vert. (m/sec)	EW (m/sec)	NS (m/sec)	Horiz. (m/sec)	Vert. (m/sec)
dip90HA	1.5	1.0	1.6	0.52	2.6	1.0	2.6	0.80
dip90HB	1.4	1.0	1.4	0.52	2.0	1.1	2.0	0.72
dip75HA	2.3	1.1	2.4	0.91	3.6	1.5	3.7	1.2
dip75HB	2.1	1.2	2.2	0.89	2.5	1.3	2.8	1.2
dip60HA	2.7	1.6	2.8	2.2	3.9	2.4	4.2	3.0
dip60HB	1.9	1.4	2.0	1.8	2.4	2.2	2.8	2.2
dip45HA	1.3	1.6	1.7	2.5	2.0	2.5	2.7	3.9
dip45HB	1.2	1.4	1.4	2.3	1.5	2.4	2.4	2.8
dip30HA	1.4	1.2	1.4	1.9	1.5	1.7	1.7	3.0
dip30HB	1.4	1.5	1.6	2.5	1.6	2.2	2.2	3.3

3.3 Ground Motion Time Histories

This section examines the velocity time histories at a set of sites located along two perpendicular lines on the ground surface (dotted lines shown in figure 2.1). The north-south line runs along the entire length of the domain and over the surface trace of the fault with the sites sitting on the hanging wall side of the fault. The east-west line runs across the entire width of the domain perpendicular to the strike of the fault; it sits above the center of the fault. On both lines the sites lie approximately 10 km apart.

The velocity time histories for scenario dip90HA, which are shown in figure 3.15, further illustrate the trends seen in the snapshots of the velocity and the plots of the maximum displacements and velocities. At all of the sites, the vertical component is negligible compared to the north-south and east-west components for the pure strike-slip faulting. The slip time histories dominate the north-south component (fault parallel) along the surface trace of the fault, while the Love waves dominate the east-west component. The velocities along the east-west line demonstrate that the strongest motions are concentrated near the trace of the fault.

As the dip of the fault decreases and the slip rake angle increases, the amplitude of the Love waves decreases and the amplitude of the Rayleigh waves increases. This corresponds to smaller-amplitude motion in the east-west direction and larger-amplitude motion in the north-south and vertical directions. For scenario dip60HA (figure 3.16) the amplitudes of the three components are relatively equal because the motions contain large-amplitude Love and Rayleigh waves. Along the north-south line, the vertical component is largest along most of the fault trace, while off the north end of the fault, the east-west component is largest. The sites along the east-west line indicate that at the center of the fault, the strongest motion remains concentrated near the surface trace. However, from the maximum displacements and velocities (figures 3.9 and 3.10) we know that the region northwest of the northern portion of the fault also experiences strong shaking from the Love and Rayleigh waves.

Maintaining the hypocenter at HA while further decreasing the dip of the fault and increasing the slip rake angle means that the rupture propagates predominantly in the mode-III direction (perpendicular to the slip direction). In our limiting case of the 30 degree dipping fault with pure thrust motion, the velocity time histories displayed in figure 3.17 indicate that the slip time histories and Rayleigh waves control the motion; Love waves are much less prominent. At sites along the north-south line, the east-west component generally corresponds to the slip time history (the negative amplitude means the hanging wall motion is to the west), while the retrograde motion of the Rayleigh waves dominates the north-south and vertical components. On the east-west line, the shallow dip of the fault causes stronger motions on the hanging wall away from the fault trace compared to the motions from scenarios with the more steeply dipping faults.

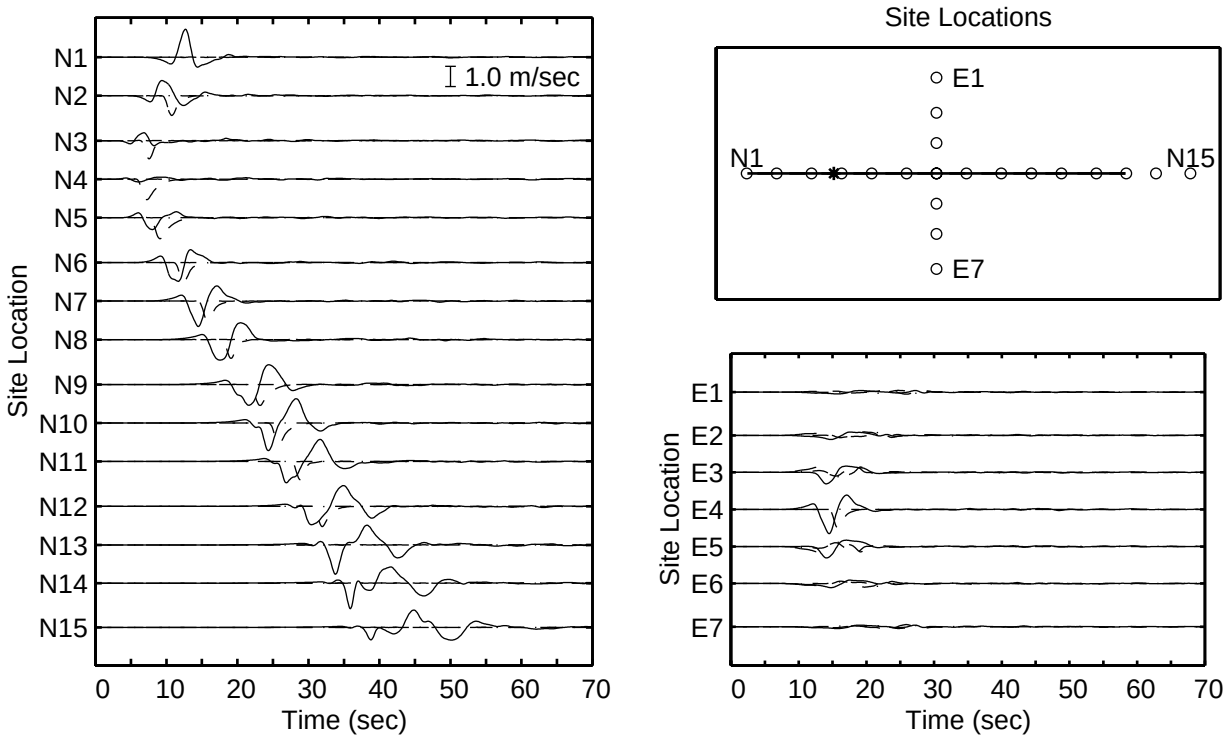

Fig. 3.15. Velocity time histories along a north-south line over the trace of the fault (left) and along an east-west line passing over the center of the fault (lower right) for scenario dip90HA. The three components are denoted by the solid line (east-west), the dashed line (north-south), and the dash-dotted line (vertical). The diagram in the upper right identifies the locations of the sites (open circles) relative to the fault trace (solid line) and the epicenter (asterisk). On the north-south line the slip time histories dominate the north-south component, while the Love waves dominate the east-west component. The motions on the east-west line are small except near the fault trace.

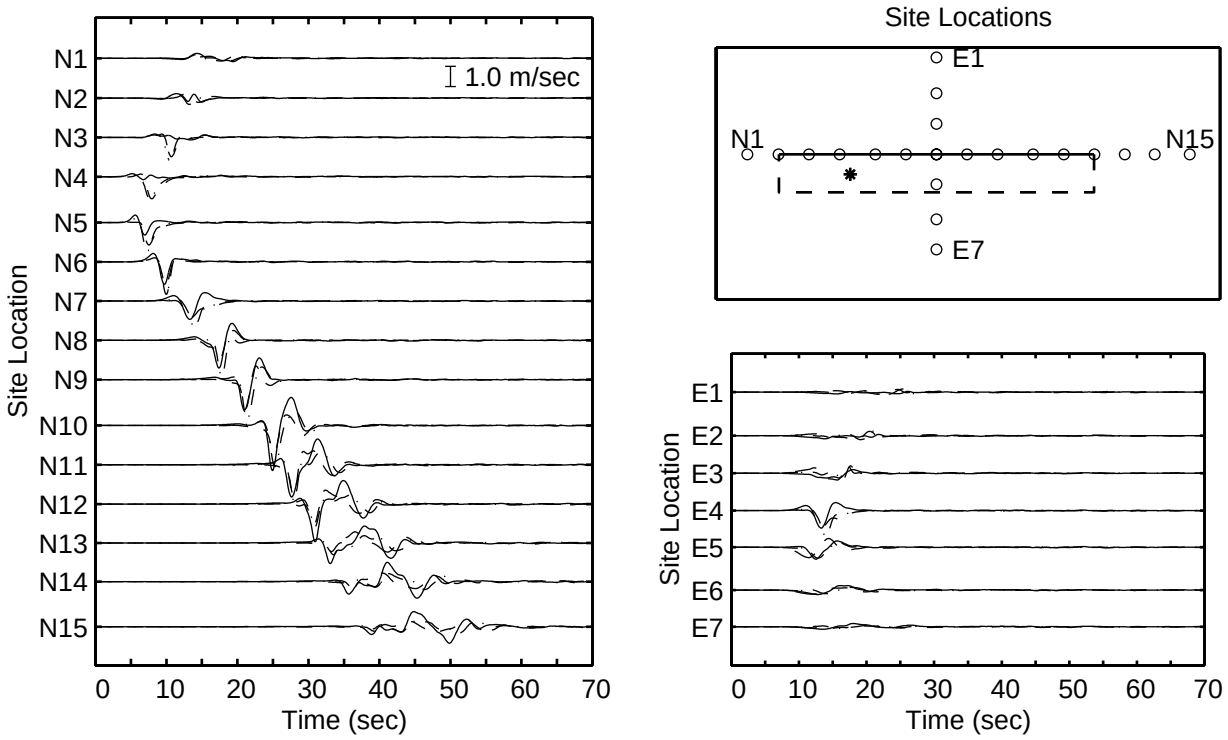

Fig. 3.16. Velocity time histories along a north-south line over the trace of the fault (left) and along an east-west line passing over the center of the fault (right) for scenario dip60HA. The three components are denoted by the solid line (east-west), the dashed line (north-south), and the dash-dotted line (vertical). The diagram in the upper right identifies the locations of the sites (open circles) relative to the fault trace (solid line), the buried edges of the fault (dashed lines), and the epicenter (asterisk). The presence of large-amplitude Love and Rayleigh waves results in all three velocity components having similar amplitudes at sites along the north-south line.

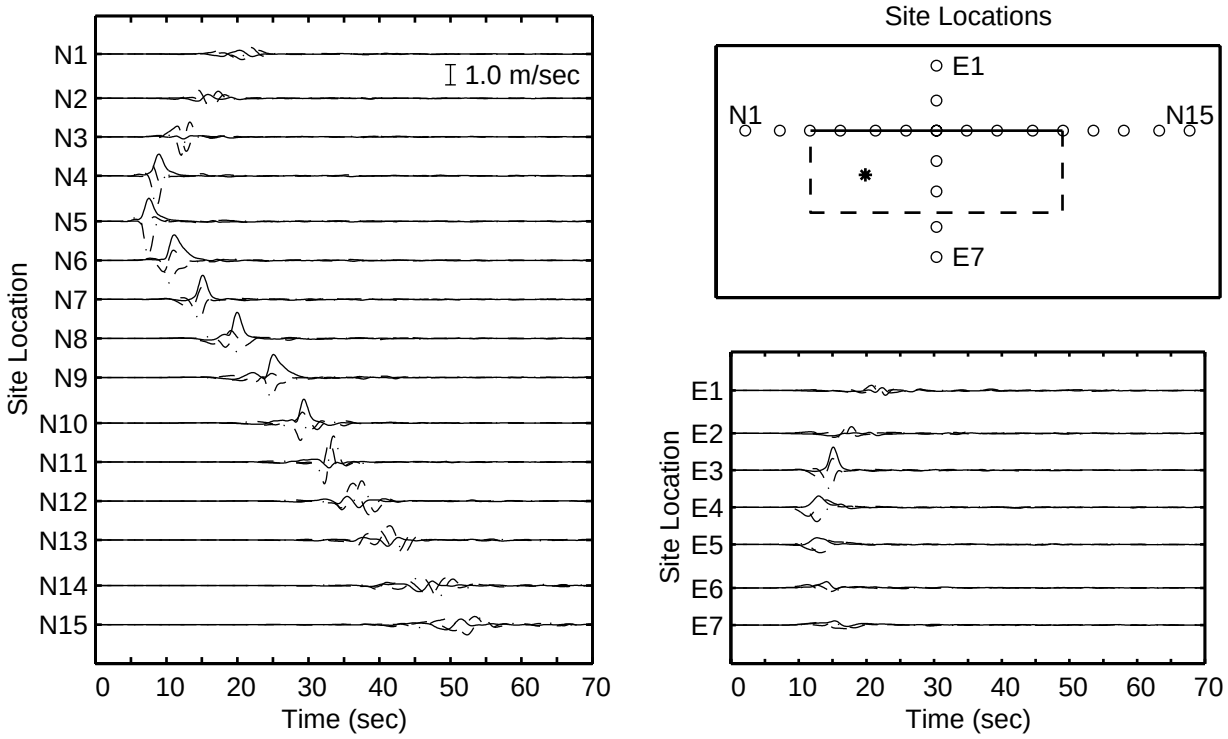

Fig. 3.17. Velocity time histories along a north-south line over the trace of the fault (left) and along an east-west line passing over the center of the fault (right) for scenario dip30HA. The three components are denoted by the solid line (east-west), the dashed line (north-south), and the dash-dotted line (vertical). The diagram in the upper right identifies the locations of the sites (open circles) relative to the fault trace (solid line), the buried edges of the fault (dashed lines), and the epicenter (asterisk). Sites along the surface trace of the fault on the hanging wall show the slip time history on the east-west component, while the retrograde motion of the Rayleigh waves controls the north-south and vertical components. The ground motions are significantly larger on the hanging wall in this scenario compared to scenarios with the same hypocenter and steeper dipping faults.

Shifting the hypocenter from HA to HB (5 km up-dip from the bottom center of the fault) creates a more bilateral rupture. For the 60 degree dipping fault, the velocity waveforms retain the same general shape in scenario dip60HB (figure 3.18) as in scenario dip60HA (figure 3.16). In the northern half of the domain, the rupture propagates over a shorter distance in the direction of slip which reduces both the amplitude of the ground motions and the duration of shaking away from the fault.

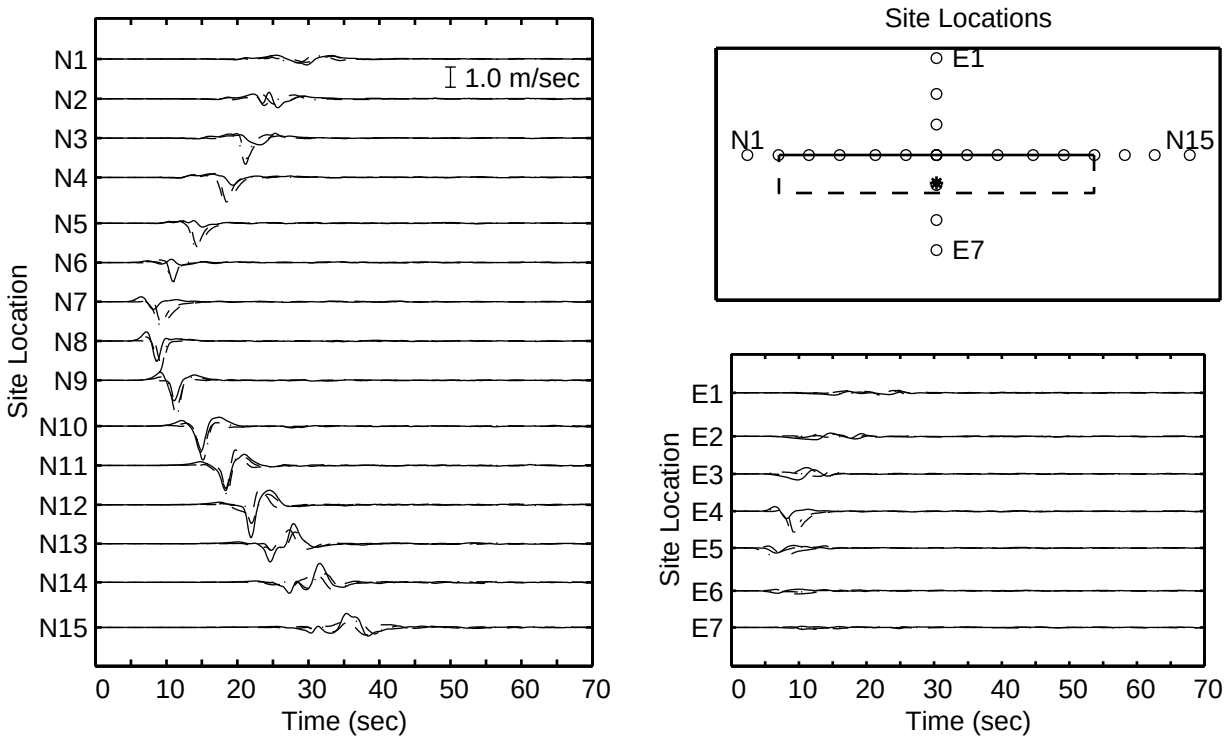

Fig. 3.18. Velocity time histories along a north-south line over the trace of the fault (left) and along an east-west line passing over the center of the fault (right) for scenario dip60HB. The three components are denoted by the solid line (east-west), the dashed line (north-south), and the dash-dotted line (vertical). The diagram in the upper right identifies the locations of the sites (open circles) relative to the fault trace (solid line), the buried edges of the fault (dashed lines), and the epicenter (asterisk). Moving the hypocenter from HA to HB creates a more bilateral rupture and reduces the amplitude of the velocity time histories in the northern half of the domain (region with maximum directivity). The waveforms retain the same general shapes.

For the case of pure thrust motion (with a fault dip angle of 30 degrees), the mode-II direction corresponds to up-dip rupture, so the hypocenter near the bottom center of the fault increases the amount of mode-II rupture. Consequently, as shown in figure 3.19, larger-amplitude motions are observed in scenario dip30HB compared to scenario dip30HA. This is especially true

for the east-west line over the center of the fault. Additionally, while the vertical component for the site on the north-south line located directly up-dip from the hypocenter is about the same for the two scenarios, the vertical components at the surrounding locations dramatically increase for hypocenter HB. Finally, with hypocenter HB single-sided pulses characterize the velocity time histories along the fault trace, while off the ends of the fault double-sided pulses associated with Rayleigh waves characterize the motion.

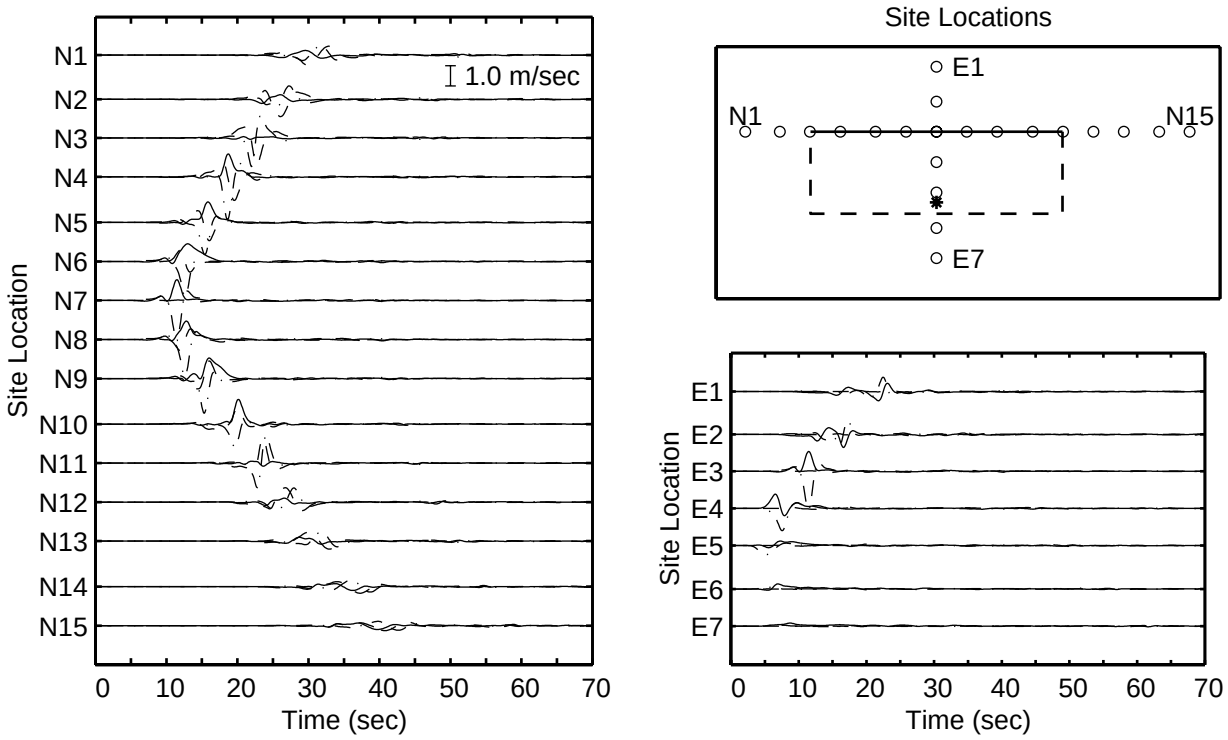

Fig. 3.19. Velocity time histories along a north-south line over the trace of the fault (left) and along an east-west line passing over the center of the fault (right) for scenario dip30HB. The three components are denoted by the solid line (east-west), the dashed line (north-south), and the dash-dotted line (vertical). The diagram in the upper right identifies the locations of the sites (open circles) relative to the fault trace (solid line), the buried edges of the fault (dashed lines), and the epicenter (asterisk). The hypocenter near the bottom center of the fault maximizes the amount of up-dip rupture, which coincides with the direction of slip, and generates significantly larger ground motions relative to a hypocenter at mid-depth away from the center of the fault.

Appendix C contains plots of the velocity time histories along the two lines for all ten scenarios.

3.4 Response Spectra

The acceleration response spectra provide an additional tool for evaluating the severity of shaking associated with the earthquake ruptures. The horizontal acceleration response spectra are computed for five percent of critical damping after rotating the ground motion in the direction of the maximum peak-to-peak velocity for each location. The focus of the following two sections is on the response spectrum for a few select periods over the entire ground surface and then at a single site for higher resolution spectra.

3.4.1 Response Spectra on Ground Surface

Figure 3.20 gives the response spectra on the entire ground surface for scenario dip90HA at periods of 2.0, 3.0, 4.0, and 5.0 seconds. Several local maxima in the response spectra exceed 0.4 g; values greater than 0.6 g occur off the two ends of the fault for a period of 3.0 sec. Although not immediately evident in the contour plots of the response spectra in figure 3.20, the spatial distributions become smoother at longer periods due to the larger wavelengths of the surface waves that control the response.

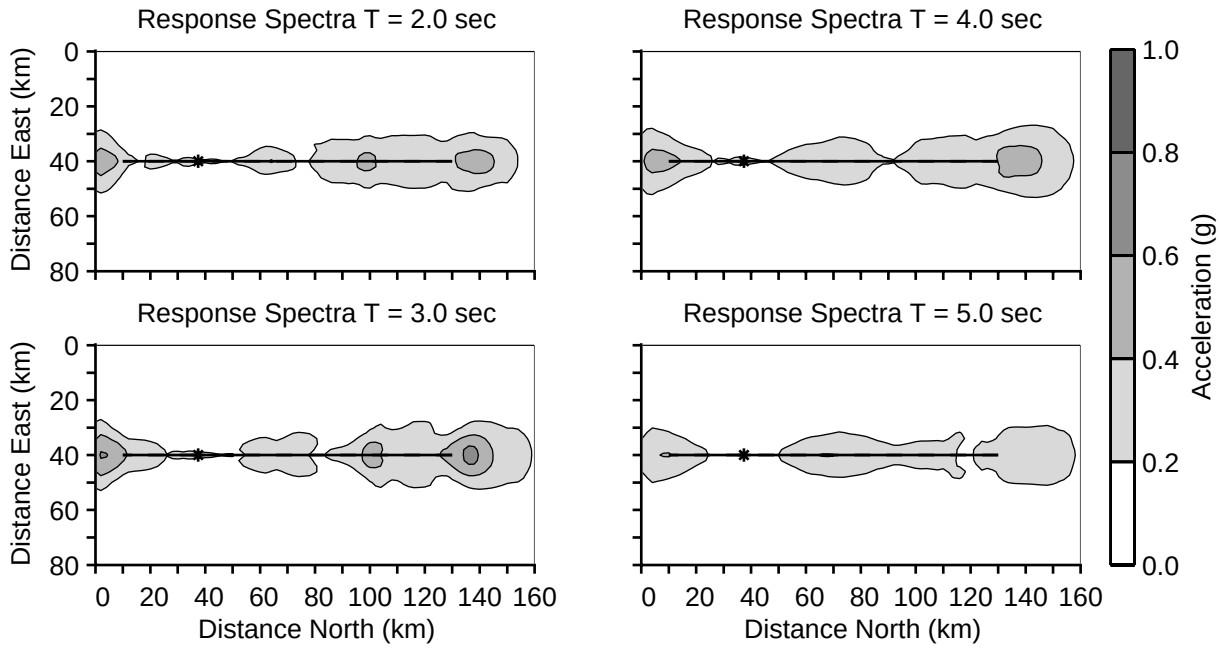

Fig. 3.20. Horizontal acceleration response spectra on the ground surface for five percent of critical damping at four periods for scenario dip90HA. The thick solid line shows the surface trace of the fault and the asterisk identifies the epicenter. The spectra are associated with ground motions resolved along the direction of the maximum peak-to-peak velocity.

The response spectra for scenario dip60HA, shown in figure 3.21, display a complex spatial distribution northwest of the northern half of the fault. These complex variations arise from the presence of both Love and Rayleigh waves which have different radiation patterns; they created similar patterns in the distributions of the maximum velocity and maximum peak-to-peak velocity (figures 3.9 and 3.10). The greater wavelengths associated with the longer-period surface waves smooth these patterns as the period increases. As expected based on the larger ground motions for scenario dip60HA compared to the strike-slip scenario dip90HA, the response spectra for all four periods contain many local maxima exceeding 0.6 g with some greater than 0.8 g.

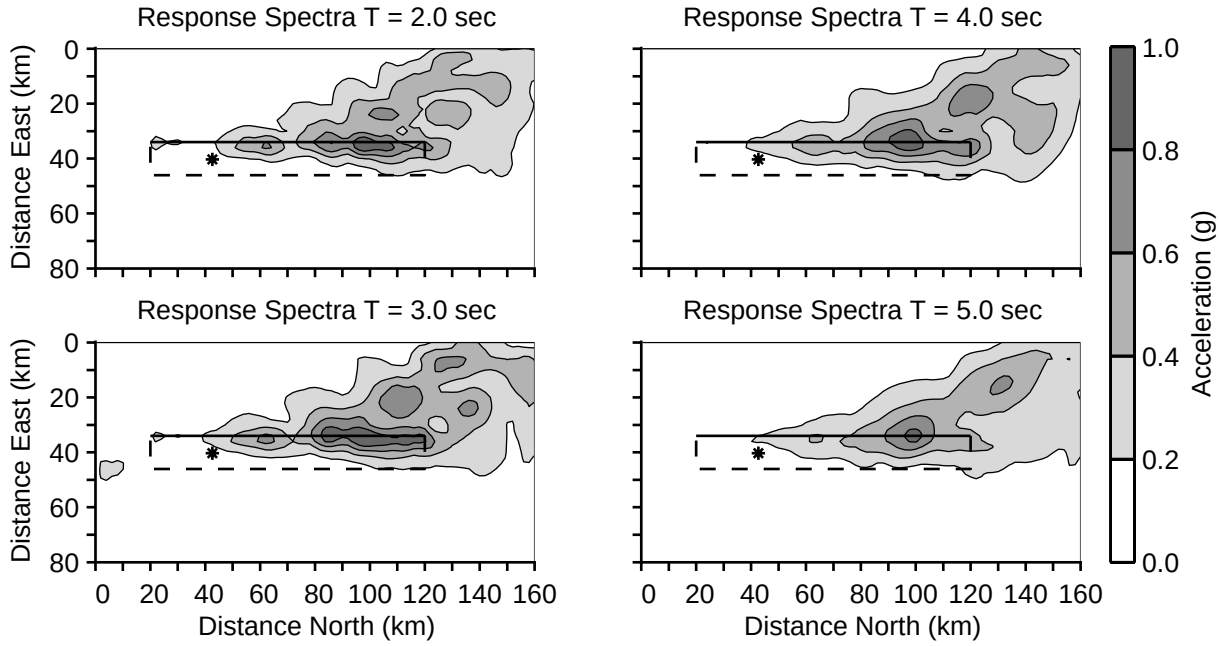

Fig. 3.21. Horizontal acceleration response spectra on the ground surface for five percent of critical damping at four periods for scenario dip60HA. The thick solid line shows the surface trace of the fault, the thick dashed line indicates the surface projection of the buried edges of the fault, and the asterisk identifies the epicenter. The spectra are associated with ground motions resolved along the direction of the maximum peak-to-peak velocity. The response spectra reflect both the large-amplitude ground motions and the complex spatial distribution of shaking created by the presence of Love and Rayleigh waves.

As the dip angle of the fault decreases and the slip rake angle increases, the response spectra values decrease in accordance with the smaller ground motions. For scenario dip30HA the response spectra in figure 3.22 contain only small regions with values greater than 0.4 g. Smoother variations are observed for longer periods, along with some minor fluctuations in the distribution

with changes in period, but the largest values continue to coincide with the peaks in the Rayleigh wave radiation pattern that extend off the northwest and southwest corners of the fault at angles of about 45 degrees.

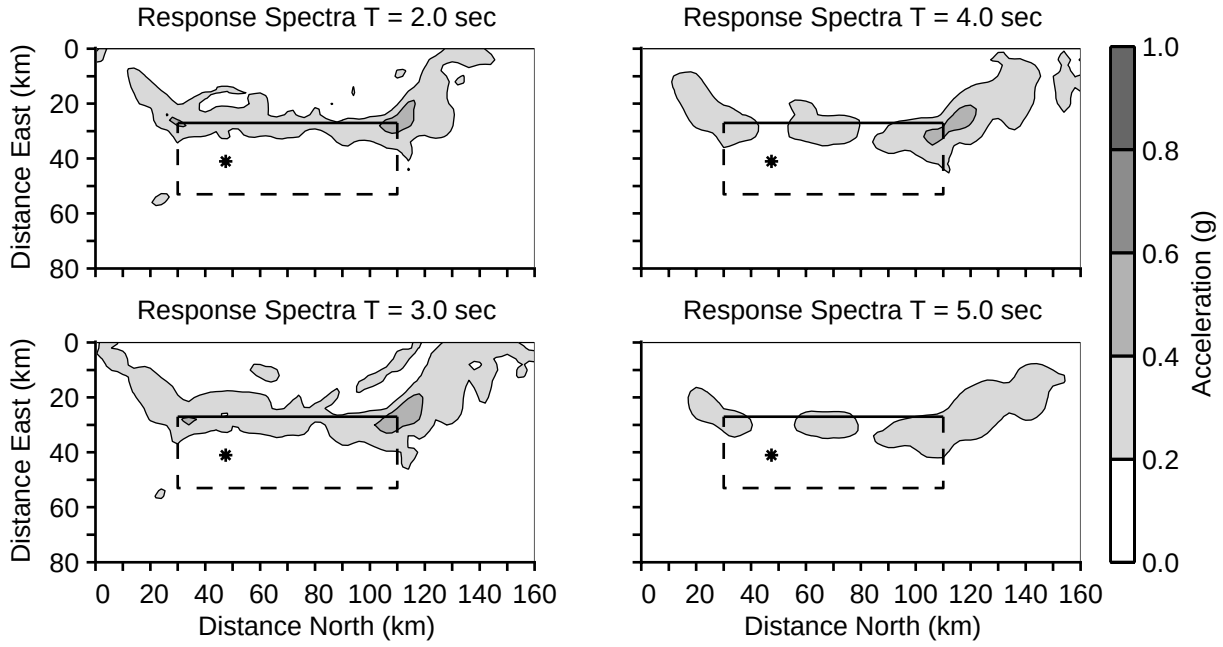

Fig. 3.22. Horizontal acceleration response spectra on the ground surface for five percent of critical damping at four periods for scenario dip30HA. The thick solid line shows the surface trace of the fault, the thick dashed line indicates the surface projection of the buried edges of the fault, and the asterisk identifies the epicenter. The spectra are associated with ground motions resolved along the direction of the maximum peak-to-peak velocity. The maxima in the response spectra occur at peaks in the Rayleigh wave radiation pattern which extend in the southwest and northwest directions from the top corners of the fault.

For scenario dip60HB where the hypocenter sits 5.0 km up-dip from the bottom center of the 60 degree dipping fault, as opposed to mid-depth at the southern quarter point of the fault, the horizontal acceleration response spectra values shown in figure 3.23 decrease significantly with values exceeding 0.6 g over only small, limited areas. This stems from the lower-amplitude ground motions. However, the spatial distribution has a similar complex shape due to the combination of Love and Rayleigh waves that dominate the ground motions.

With a hypocenter slightly up-dip from the bottom center of the fault and pure thrust motion in scenario dip30HB, the acceleration response spectra given in figure 3.24 exhibit a significant change in shape compared to a mid-depth hypocenter at the southern quarter point of the fault.

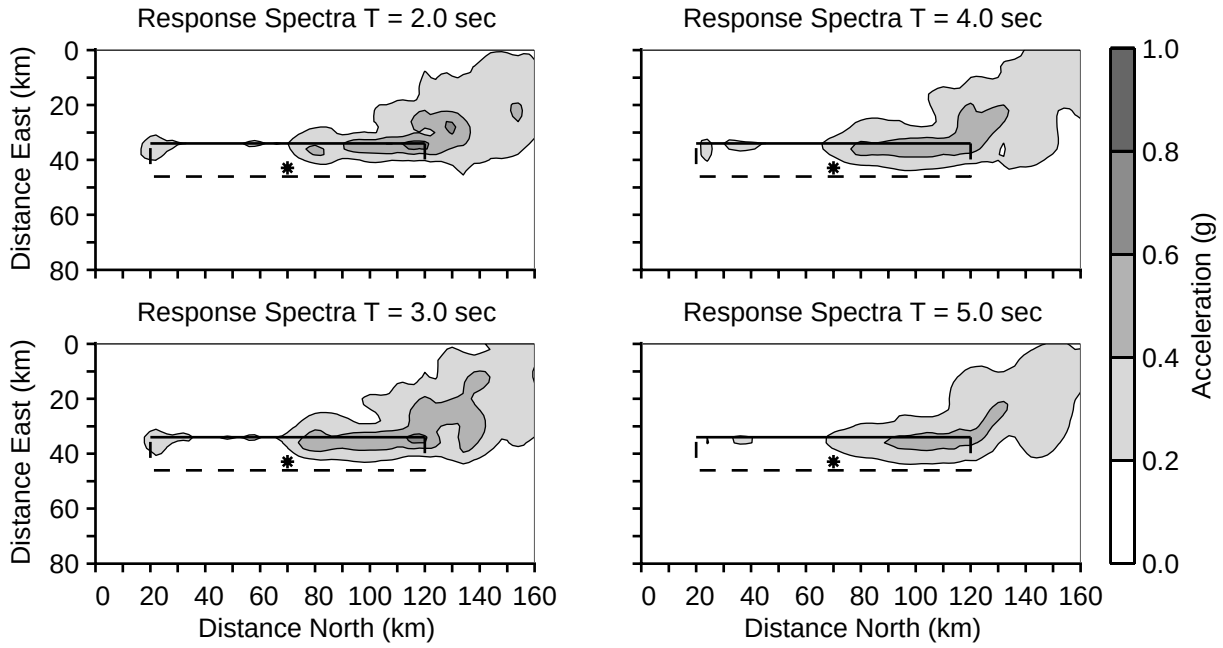

Fig. 3.23. Horizontal acceleration response spectra on the ground surface for five percent of critical damping at four periods for scenario dip60HB. The thick solid line shows the surface trace of the fault, the thick dashed line indicates the surface projection of the buried edges of the fault, and the asterisk identifies the epicenter. The spectra are associated with ground motions resolved along the direction of the maximum peak-to-peak velocity. A shift in the hypocenter from HA to HB results in lower response spectra values, but a similar complex spatial distribution due to the continued presence of both Love and Rayleigh waves is still present.

The values are greater over a larger region up-dip from the hypocenter and are much larger near the southwest corner of the fault (a region where the ground motions also increase). In contrast to scenario dip30HA where the spectral values rarely exceed 0.4 g, the spectral values exceed 0.4 g over a significant area for a period of 3.0 sec and reach 0.6 g at some locations for a period of 2.0 sec.

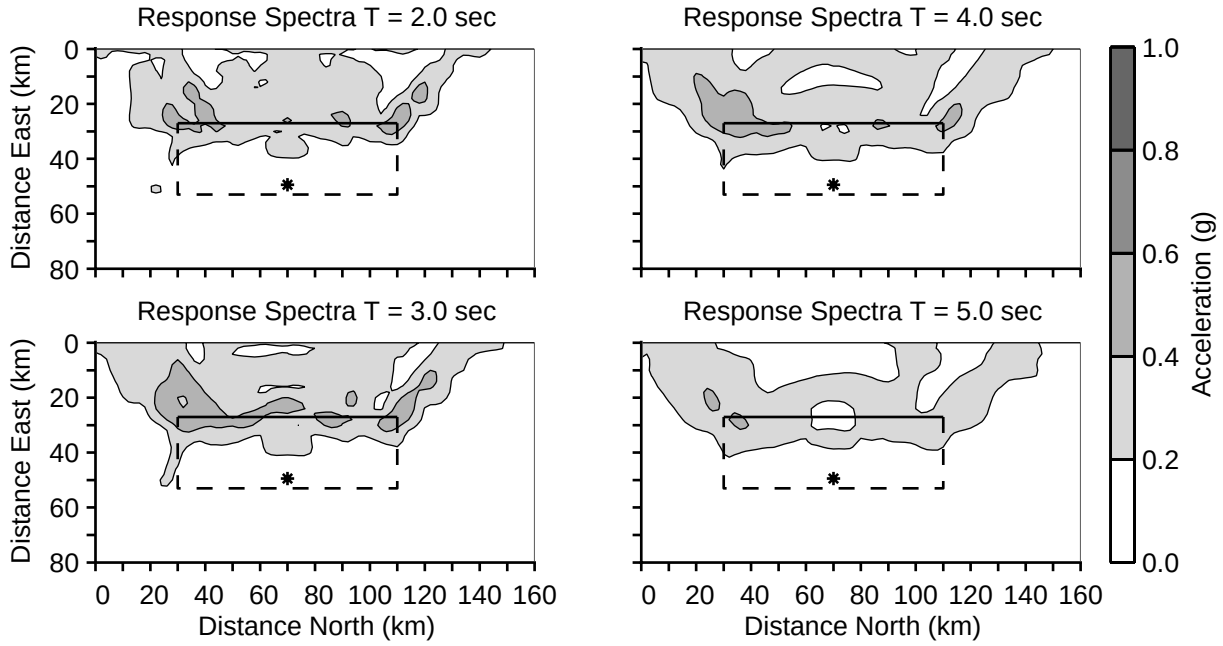

Fig. 3.24. Horizontal acceleration response spectra on the ground surface for five percent of critical damping at four periods for scenario dip30HB. The thick solid line shows the surface trace of the fault, the thick dashed line indicates the surface projection of the buried edges of the fault, and the asterisk identifies the epicenter. The spectra are associated with ground motions resolved along the direction of the maximum peak-to-peak velocity. Locating the hypocenter near the bottom center of the fault increases the amount of up-dip rupture and produces spectral values of more than 0.4 g over a significant area in the up-dip direction.

3.4.2 Response Spectra at Site N10

In order to illustrate the variation in the response spectra as a more continuous function of period, we examine the horizontal acceleration response spectra at site N10, which sits on the hanging wall of the fault trace 30 km north of the center of the fault. This site lies in the region with the most rupture directivity for all ten scenarios and generally experiences some of the strongest motion. Figure 3.25 shows the response spectra over a period range of 2.0 to 12 seconds for the scenarios discussed in the previous section. The spectra reaffirm that the ground motion in scenario

dip60HA is the most severe with values between 0.9 g and 1.0 g over a period range of 2.0 to 5.0 seconds. Likewise, the motion in scenario dip30HA is the most benign over nearly the entire range of periods. At site N10 the response spectra for all scenarios fall below 0.4 g for periods above about 9 sec.

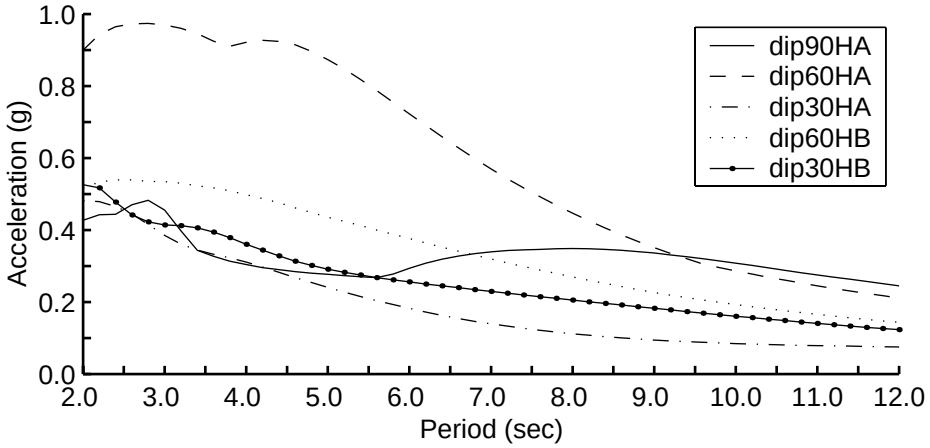

Fig. 3.25. Horizontal acceleration response spectra at site N10 for scenarios dip90HA, dip60HA, dip30HA, dip60HB, and dip30HB. The spectra are associated with ground motions resolved along the direction of the maximum peak-to-peak velocity. The large values in the response spectrum for scenario dip60HA at periods between 2.0 and 5.0 seconds correspond to the strong level of shaking associated with the large-amplitude Love and Rayleigh waves.

Appendix D contains plots of the horizontal acceleration response spectra on the ground surface at four periods (2.0–5.0 seconds) for all ten scenarios, as well as response spectra as continuous functions of period for each scenario at site N10.

4 Discussion

Large-amplitude long-period ground motions were observed in all ten scenarios. The choices for the values of final slip, peak slip rate (slip duration), and rupture speed all affect the amplitude of the ground motion [Aagaard *et al*., 2001]. As discussed in section 2.3, the values selected for these simulations fall within reasonable ranges, so the level of shaking should be indicative of the long-period motions in real earthquakes. Furthermore, even if the amplitude of the motion was under- or overestimated due to the earthquake parameters selected, the trends with respect to the geometry of the faulting remain valid.

In order to gauge how the severity of shaking changes on a large scale in the transition from pure strike-slip faulting on a vertical fault to thrust faulting on a 30 degree dipping fault, three aggregate measures of ground motion are considered: the area on the ground surface where a given level of displacement or velocity is exceeded, how fast the displacements and velocities on the ground surface decay with distance from the fault, and the radiated energy.

4.1 Area Subjected to Levels of Ground Motion

Figure 4.1 gives the areas on the ground surface where the maximum peak-to-peak displacements or velocities exceed a given value for all five scenarios with hypocenter HA (mid-depth at the southern quarter point of the fault), where each scenario corresponds to a different dip angle of the fault. In all five cases very large areas (more than 1000 square kilometers) receive long-period ground motions with peak-to-peak displacements or velocities greater than 1.0 m or 1.0 m/sec. In accordance with the observations noted in chapter 3, the amount of rupture directivity controls the amplitude of the motion, so that the largest areas subjected to strong shaking occur in the scenarios with a fault dip angle of 60 or 75 degrees. Furthermore, at the strongest levels of shaking, these areas far exceed the corresponding areas for the other scenarios.

The case of pure strike-slip motion on a vertical fault generally falls in the middle ground below the 60 and 75 degree dipping fault scenarios and above the 45 and 30 degree dipping fault scenarios. The curves relating area and maximum peak-to-peak displacements for scenarios

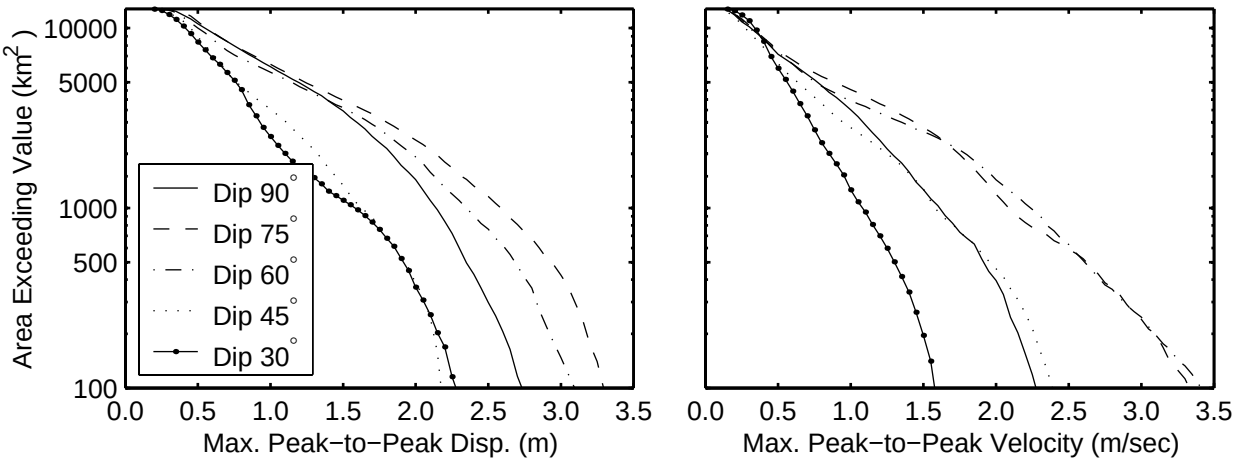

Fig. 4.1. Area on the ground surface where the maximum peak-to-peak displacements (left) and velocities (right) exceed a given value for scenarios with hypocenter HA. In all five scenarios areas greater than 1000 km^2 undergo peak-to-peak displacements and velocities exceeding 1.0 m or 1.0 m/sec with much larger areas for scenarios dip60HA and dip75HA.

dip30HA and dip45HA closely follow each other, but the curve relating area and maximum peak-to-peak velocities for scenario dip45HA lies well to the right of the one for scenario dip30HA. Thus, for hypocenter HA, the case of pure thrust motion on a 30 degree dipping fault results in the smallest area subjected to a given level of peak-to-peak velocity.

Compared to the scenarios with hypocenter HA, those with hypocenter HB (5.0 km up-dip from the bottom center of the fault) exhibit much less variation in the area experiencing a given level of shaking for the various combinations of fault dip and slip rake angles as illustrated in figure 4.2. The more central hypocenter near the bottom of the fault leads to less variation in the distance the rupture propagates in the mode-II direction (direction parallel to slip) because the amount of along-strike rupture decreases while the amount of up-dip rupture increases. This reduces the amount of mode-II rupture in the cases with small slip rake angles, which were dominated by mode-II rupture for hypocenter HA, and increases the amount of mode-II rupture in the cases with large slip rake angles, which were dominated by mode-III rupture for hypocenter HA. The 60 degree dipping fault with a slip rake angle of 45 degrees continues to generally produce the largest areas subjected to a given level of shaking with this different hypocenter, but the curve for pure thrust motion on the 30 degree dipping fault shifts toward the middle ground. For some ranges of moderate peak-to-peak velocities, the case of pure thrust motion on the 30 degree dipping fault has the largest areas where these levels of motion are exceeded.

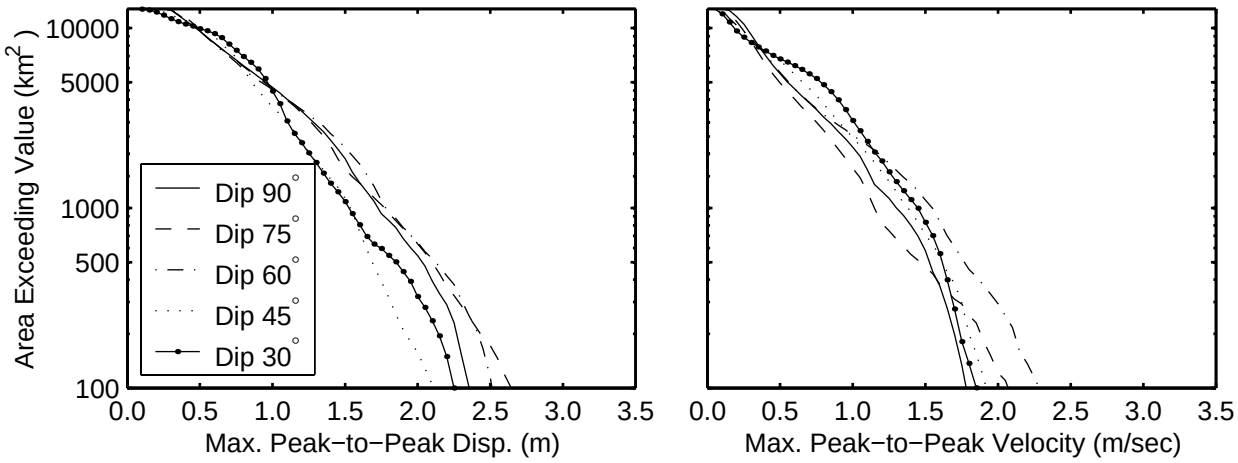

Fig. 4.2. Area on the ground surface where the maximum peak-to-peak displacements (left) and velocities (right) exceed a given value for scenarios with hypocenter HB. Shifting the hypocenter to near the bottom center of the fault leads to much smaller variations in the area subjected to a given level of shaking across the five fault dip and slip rake angle pairs.

Figure 4.3 illustrates how changing the hypocenter for pure thrust motion on the 30 degree dipping fault alters the curves relating the area experiencing a given level of peak-to-peak displacement and velocity. The hypocenter has only a small effect on the curve for the peak-to-peak displacements, because the slip distribution, which remains the same, largely controls the amplitude of the peak-to-peak displacements. On the other hand, moving the hypocenter from HA to HB shifts the curve for the peak-to-peak velocities toward larger velocities as a result of the increase in the amount of mode-II (in this case up-dip) rupture.

Appendix E contains plots of the area where the maximum peak-to-peak displacements and velocities exceed a given value for the two hypocenters (analogous to figure 4.3) for each fault geometry.

4.2 Decay in Ground Motion with Distance

In this section we characterize how the ground motions decay with distance from the fault, while including the effects of rupture directivity and the unpredictability of the hypocenter. This is done by considering identical events occurring along an infinite fault and superimposing the distributions of the maximum displacements and velocities for a given scenario such that the faults lie end to end as illustrated in figure 4.4. At each location the largest values across all of the overlapping domains were selected and then averaged along the strike of the fault to obtain the average motion on each side of the fault at a given distance. The decay in the level of motion is compared with that of the near-source factor, N_v, from the 1997 Uniform Building Code [ICBO,

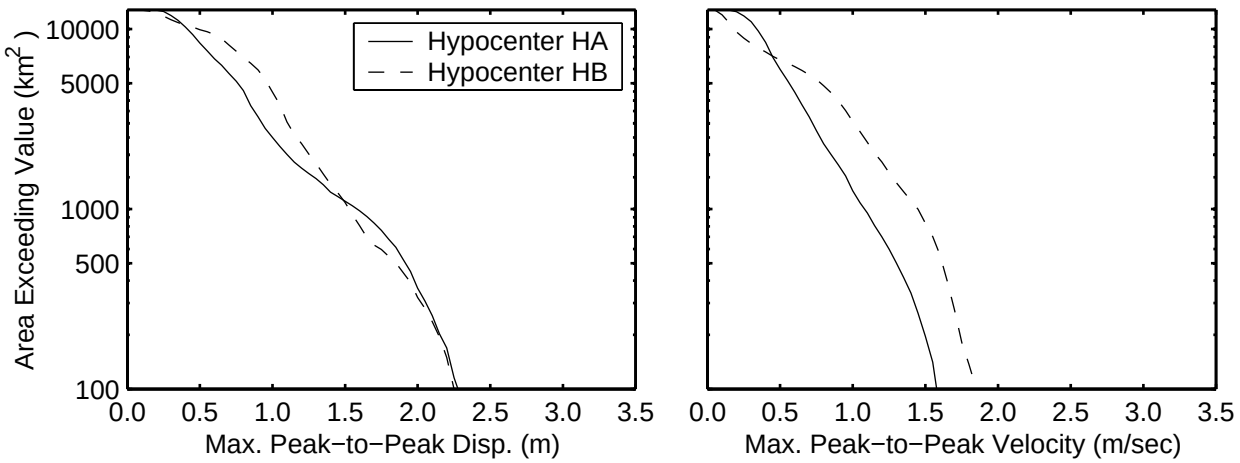

Fig. 4.3. Area on the ground surface where the maximum peak-to-peak displacements (left) and velocities (right) exceed a given value for scenarios dip30HA and dip30HB. For the 30 degree dipping fault, the hypocenter has a strong effect on the area subjected to a given level of peak-to-peak velocity, but has little effect on the area subjected to a given level of peak-to-peak displacement.

1997]. Figure 4.5 displays the UBC near-source factor for each of the five fault geometries. On the up-dip (west) side of the fault, the near-source factors are identical, but on the down-dip (east) side of the fault, the near-source factors for shallower dip angles remain high before decreasing at greater distances from the fault.

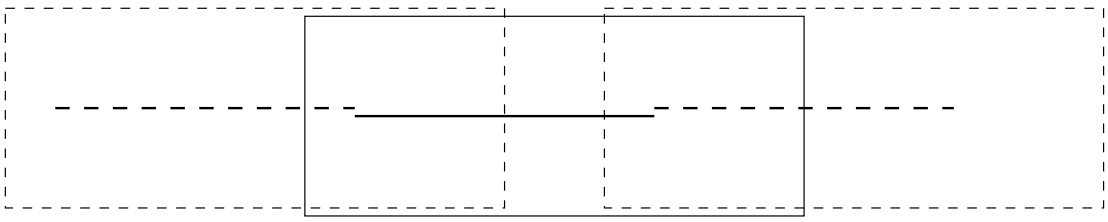

Fig. 4.4. Illustration of how an infinite fault is created from the finite fault in order to examine the decay in ground motion amplitudes with distance from the fault.

The variation in the ground motions along the strike of the fault creates a complex decay in the ground motions with distance from the fault as demonstrated for scenario dip60HA in figure 4.6. The 60 degree dip angle of the fault produces an asymmetric distribution of the maximum peak-to-peak displacements and velocities with a much slower decay with distance on the up-dip (west) side compared to the down-dip (east) side. The sites with the largest peak-to-peak values fall within the region of the highest near-source factor, but the mean falls near the up-dip boundary. Appendix F contains analogous plots for all ten scenarios.

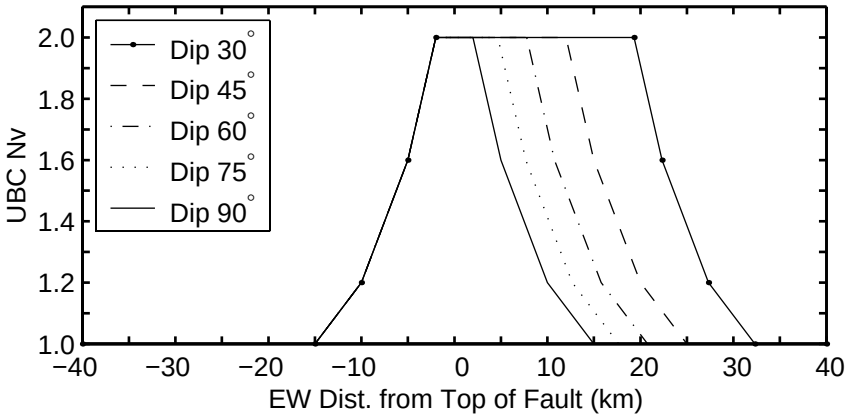

Fig. 4.5. UBC near-source factor N_v for a type A source for each fault geometry. The dip angle of the fault affects only the location where the decay begins on the hanging wall (east) side of the fault.

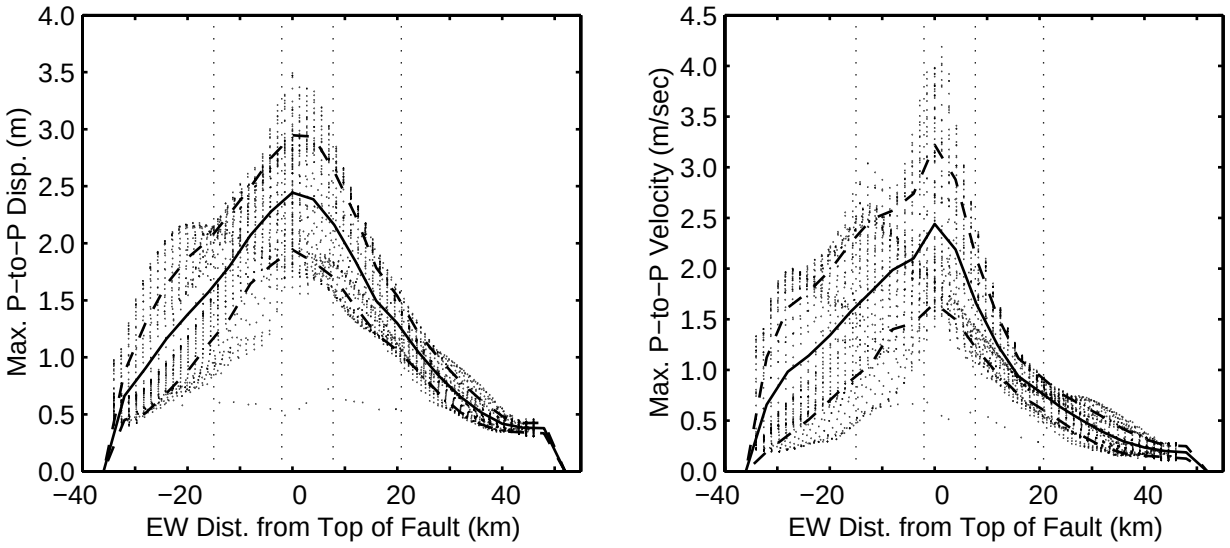

Fig. 4.6. Maximum horizontal peak-to-peak displacements and velocities as a function of distance from the fault for scenario dip60HA. The dots indicate the values at locations on the ground surface, the solid line delineates the mean, and the dashed lines correspond to one standard deviation above and below the mean. The vertical dotted lines bound the locations where the UBC near-source factor N_v is largest (inner pair) and smallest (outer pair). The fault dip angle of 60 degrees cause the asymmetry in the distributions of the peak-to-peak values, while local extrema in the distributions result in a complex decay with distance from the fault.

Figures 4.7 through 4.9 show the decay of the maximum peak-to-peak displacements and velocities with distance from the fault for each of the two hypocenters for the scenarios with fault dip angles of 90, 60, and 30 degrees. We find that moving the hypocenter causes no significant change in the shape of the mean distribution, e.g., location of the peak. However, hypocenter HB yields smaller mean values for fault dip angles of 90 and 60 degrees due to the bilateral nature of the rupture. On the other hand, this hypocenter gives larger mean values for a fault dip angle of 30 degrees because the amount of up-dip rupture increases. The asymmetry with respect to the locations that bound the smallest and largest UBC near-source values grows as the dip becomes shallower with much larger peak-to-peak velocities on the up-dip (west) side compared to the down-dip (east) side. Appendix F contains similar plots for the other fault dip angles as well.

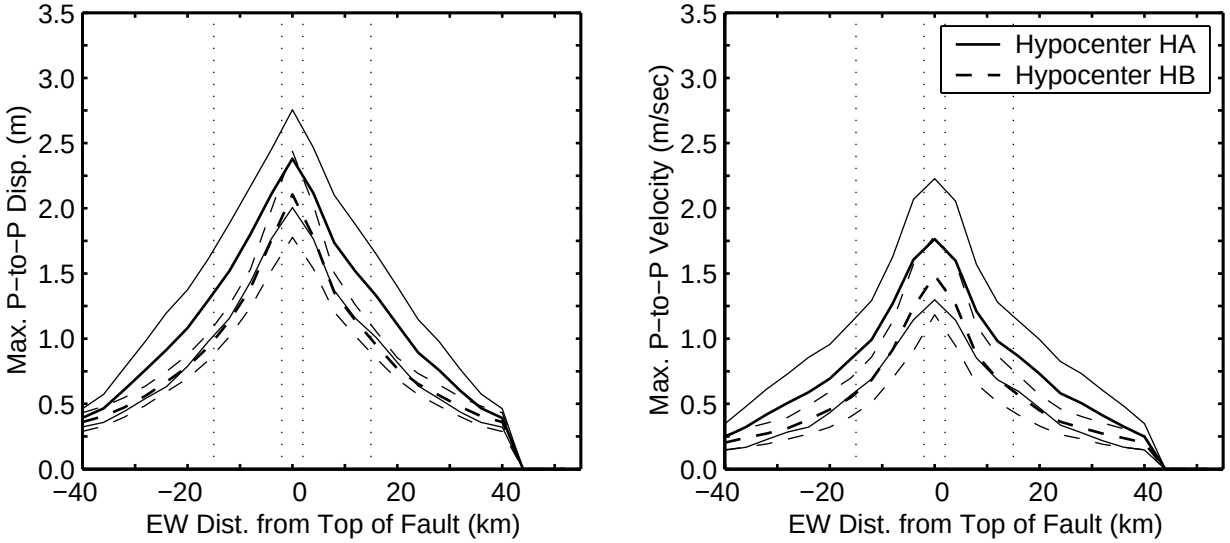

Fig. 4.7. Maximum horizontal peak-to-peak displacements and velocities as a function of distance from the fault for scenarios dip90HA and dip90HB. The three lines (solid or dashed) for each hypocenter correspond to the mean and the mean plus or minus one standard deviation. The vertical dotted lines bound the locations where the UBC near-source factor N_v is largest (inner pair) and smallest (outer pair). The maximum peak-to-peak displacements and velocities decay rapidly with distance from the fault.

In figure 4.10 the mean maximum peak-to-peak displacement and velocities for scenarios with hypocenter HA are compared across the five fault dip angles. On the down-dip (east) side of the fault at distances between 10 and 30 kilometers, the mean peak-to-peak values vary remarkably little with the dip angle of the fault. At shorter distances and on the up-dip (west) side of the fault, the mean maximum peak-to-peak values span a larger range of values; they are lowest for pure thrust motion on the 30 degree dipping fault and several times greater for oblique slip on the 60

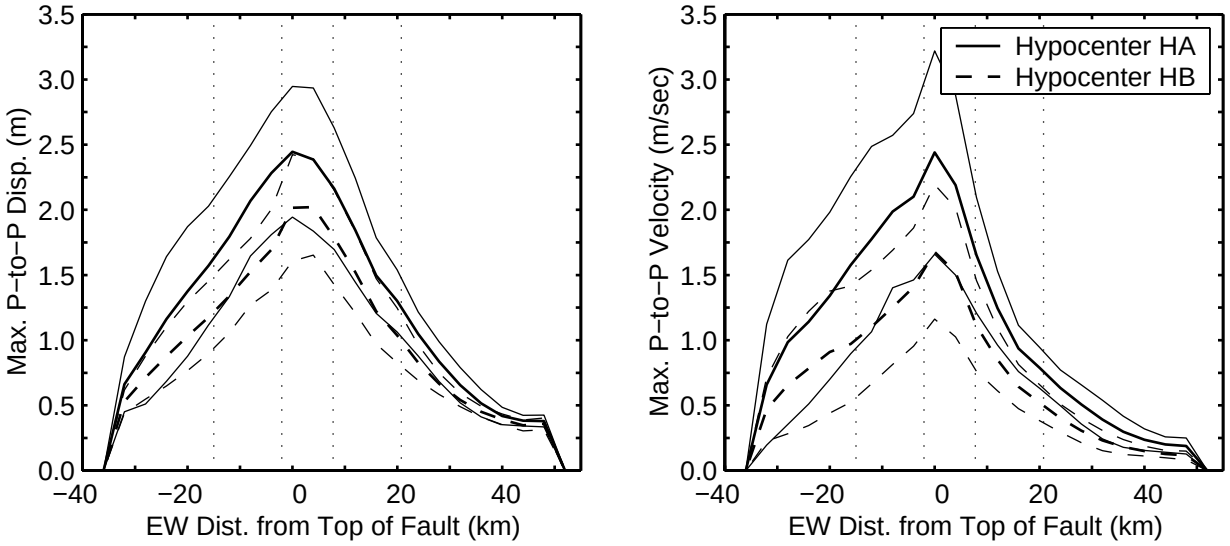

Fig. 4.8. Maximum horizontal peak-to-peak displacements and velocities as a function of distance from the fault for scenarios dip60HA and dip60HB. The three lines (solid or dashed) for each hypocenter correspond to the mean and the mean plus or minus one standard deviation. The vertical dotted lines bound the locations where the UBC near-source factor N_v is largest (inner pair) and smallest (outer pair). The directivity of the rupture produces an asymmetric distribution of the peak-to-peak values with a much slower decay with distance and greater variation about the mean on the up-dip (west) side of the fault.

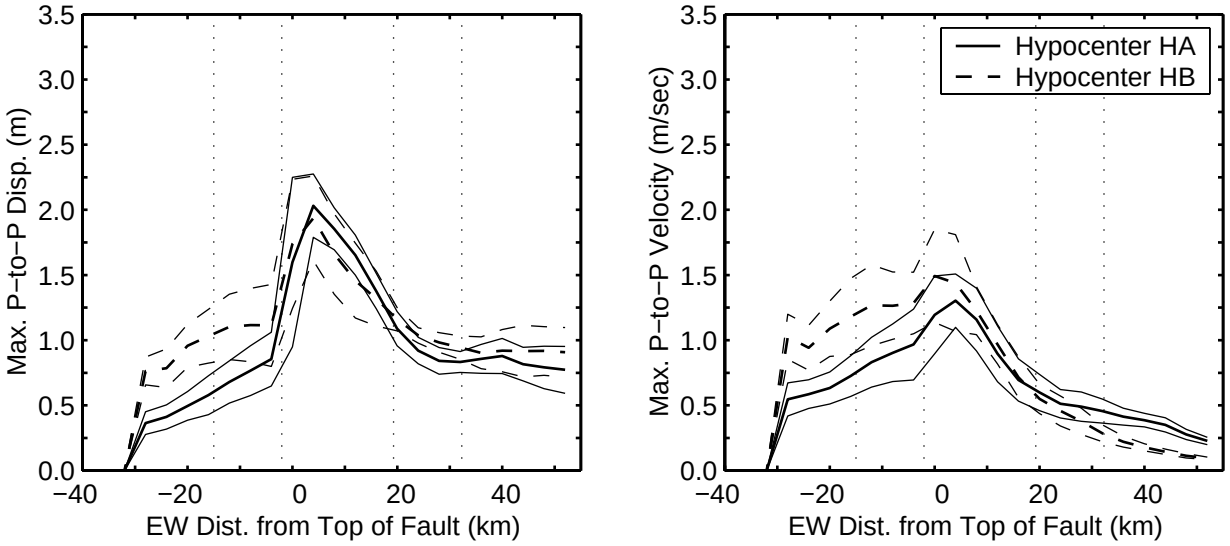

Fig. 4.9. Maximum horizontal peak-to-peak displacements and velocities as a function of distance from the fault for scenarios dip30HA and dip30HB. The three lines (solid or dashed) for each hypocenter correspond to the mean and the mean plus or minus one standard deviation. The vertical dotted lines bound the locations where the UBC near-source factor N_v is largest (inner pair) and smallest (outer pair). Shifting the hypocenter toward the bottom of the fault results in more up-dip rupture and increases the peak-to-peak velocities near the fault and at greater distances from the fault on the up-dip (west) side.

and 75 degree dipping faults. These differences arise from the high degree of rupture directivity for the combination of hypocenter HA with the steeply dipping fault geometries and the low degree of rupture directivity for the same hypocenter with the shallow dipping fault geometries.

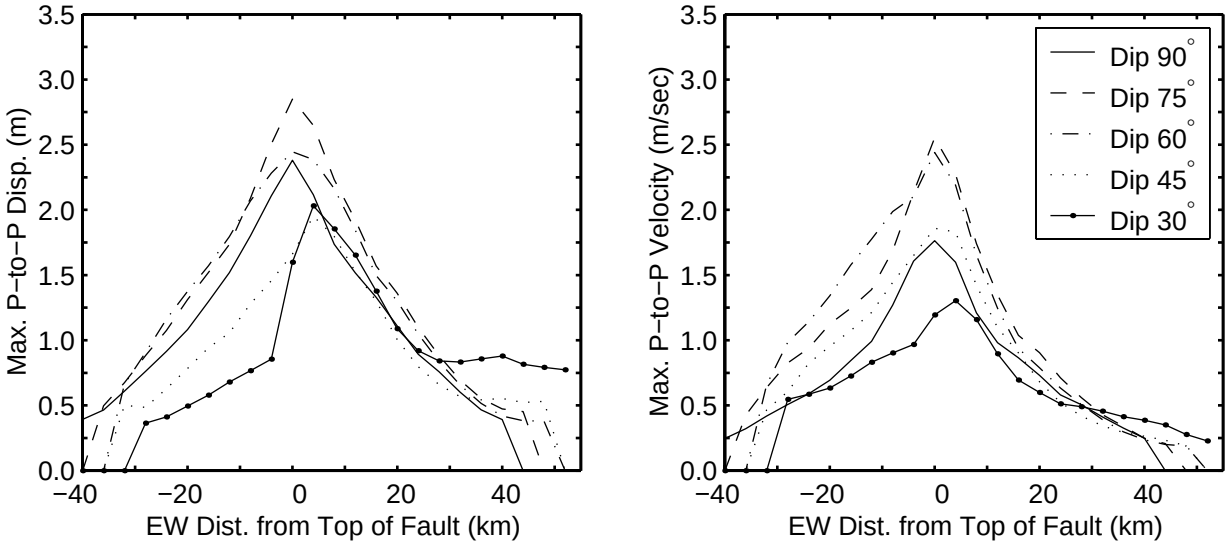

Fig. 4.10. Mean maximum horizontal peak-to-peak displacements and velocities as a function of distance from the fault for scenarios with hypocenter HA. While the mean peak-to-peak values do not dramatically differ on the down-dip (east) side of the fault, they span a wide range of values both up-dip (west) of the fault and near the fault trace.

As we found with the area where the maximum peak-to-peak motion exceeds a given level, we find less variation in how the mean maximum peak-to-peak motion decays with distance from the fault for hypocenter HB (figure 4.11) than for hypocenter HA (figure 4.10). Near the trace of the fault, the mean peak-to-peak displacements and velocities exhibit only small variations. Likewise, the mean peak-to-peak velocities on the down-dip (east) side of the fault decay in nearly an identical fashion for all five fault dip angles. However, on the up-dip (east) side of the fault, the mean peak-to-peak displacements and velocities decay at varying rates for the different fault dip angles. The values decay rapidly for the steeply dipping faults and significantly more slowly for the shallow dipping faults, although the displacements for the 30 degree dipping fault drop dramatically from the hanging wall (east side) to the footwall (west side) before decaying slowly with distance.

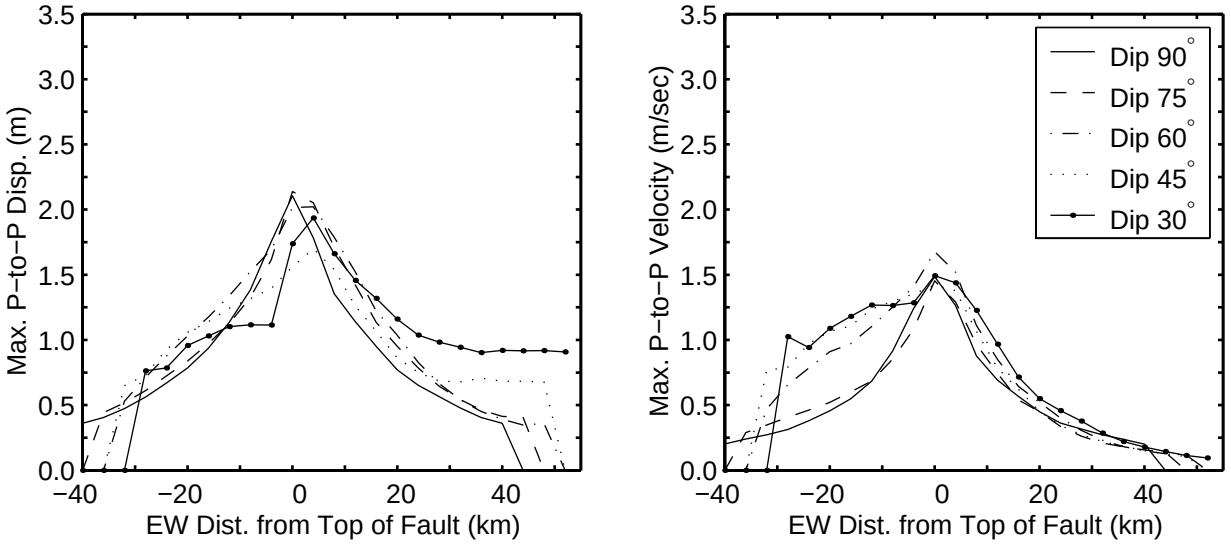

Fig. 4.11. Mean maximum horizontal peak-to-peak displacements and velocities as a function of distance from the fault for scenarios with hypocenter HB. The mean maximum peak-to-peak values generally fall within a smaller range for hypocenter HB compared to HA. On the up-dip (west) side of the fault, the mean velocities decay more slowly as the fault dip becomes shallower.

4.3 Radiated Energy

The radiated energy (figure 4.12) displays the same general trends across the ten scenarios as the velocity amplitudes on the ground surface. The radiated energy corresponds to the energy in the seismic waves in the simulation. Consequently, they do not account for energy at periods shorter than 2.0 sec. The two scenarios with the largest-amplitude ground motions (scenarios dip60HA and dip75HA) also radiate the largest amount of energy (1.1×10^{16} J). Scenario dip90HA radiates slightly less energy (9.8×10^{15} J). As expected from the amplitude of the ground motions, the smallest radiated energy of 5.5×10^{15} J occurs in scenario dip30HA. Moving the hypocenter to HB results in a 23% increase in the amount of radiated energy for the 30 degree dipping fault, while it decreases the radiated energy for the other fault geometries. Scenarios dip75HB, dip60HB, and dip45HB all radiate about 7.2×10^{15}J. Consequently, in accordance with the level of long-period shaking, the scenarios with hypocenter HB exhibit much less variation in the radiated energy than those with hypocenter HA. Overall, we find that the radiated energy closely follows the velocity amplitudes on the ground surface.

4.4 Implications for Analysis of 1999 Chi-Chi, Taiwan, Earthquake

Scenario dip30HA with pure thrust motion on a 30 degree dipping fault with hypocenter HA approximates the geometry of the Chi-Chi earthquake [Huang *et al.*, 2000; Ma *et al.*, 2000;

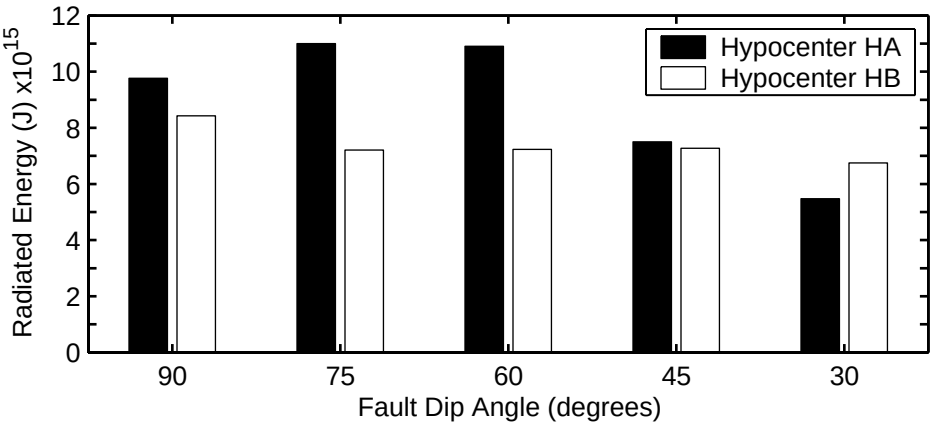

Fig. 4.12. Radiated energy for each of the two hypocenters for each of the five different fault geometries. For predominantly along-strike, unilateral ruptures (hypocenter A) the steeply dipping faults radiate considerably more energy than the shallow dipping faults. For predominantly up-dip, bilateral ruptures (hypocenter HB) the radiated energies from the five scenarios exhibit much less variation.

Johnson *et al.*, 2001; Ma *et al.*, 2001; Ji *et al.*,]. The selection of a fault area of 2400 km^2 and an average slip of 2.9 m results in a moment magnitude of 7.4 compared to estimates of 7.6–7.7 for the Chi-Chi earthquake. Nevertheless, scenario dip30HA provides a good representation of the earthquake.

For hypocenter HA scenario dip30HA generates the smallest-amplitude ground motions of all five fault geometries. Near the surface trace of the fault and in the region up-dip from the fault, the mean maximum horizontal peak-to-peak velocities for the other four scenarios far exceed those of scenario dip30HA. For example, the greatest mean maximum peak-to-peak velocities for the other four scenarios range from 1.8 m/sec to 2.6 m/sec compared to 1.3 m/sec for scenario dip30HA. Even in the case of the mean maximum peak-to-peak displacements on the hanging wall near the fault trace, where there is relatively little variation, the values for dip30HA fall at the low end of the spectrum. The largest ground motions occur for a small rake angle and a steeply dipping fault; these geometries create a significant amount of rupture directivity and generate both Love and Rayleigh waves with large amplitudes. As a result, in scenario dip60HA the horizontal acceleration response spectrum at site N10 approaches 1 g over a broad range of periods (figure 3.25).

Additionally, a deeper hypocenter than HA for thrust motion on the 30 degree dipping fault yields more rupture directivity and leads to larger ground motions. Scenario dip30HB illustrates this for a hypocenter located near the bottom center of the fault. Although the greatest mean maximum horizontal peak-to-peak displacement actually drops slightly from 2.0 m to 1.9 m, the greatest mean maximum horizontal peak-to-peak velocity increases from 1.3 m/sec to 1.5 m/sec.

Furthermore, the area on the ground surface subjected to a given level of peak-to-peak velocity increases significantly for peak-to-peak velocities greater than $0.5\,\mathrm{m/sec}$ (figure 4.3).

Of all ten scenarios considered in this study, which range from pure strike-slip motion on a vertical fault to pure thrust motion on a shallow dipping fault, the one most like the Chi-Chi earthquake produces the mildest long-period ground motion. Up-dip from the fault the ground motions for the other scenarios are significantly more severe, particularly for the case of predominantly strike-slip motion on steeply dipping faults. The increased level of long-period motion is evident in numerous measures of the ground shaking, including the response spectra, the area where the peak-to-peak displacements and velocities exceed a given level, and the mean maximum peak-to-peak displacements and velocities at a given distance from the fault.

5 Conclusions

Owing to the presence of shallow slip in the magnitude 7.4 earthquake simulations considered, Love and/or Rayleigh waves dominate the ground motions with strike-slip faulting that tends to generate Love waves and thrust faulting that tends to generate Rayleigh waves. The amount of rupture in the direction parallel to slip (mode-II direction) controls the severity of the long-period shaking. For strike-slip faulting the shaking is most severe for unilateral rupture, while for thrust faulting the shaking is most severe for up-dip rupture from a deep hypocenter.

When the hypocenter sits mid-depth at a fault quarter point, the largest ground motions occur for the 60 degree dipping fault, which has a slip rake angle of 45 degrees. This fault geometry generates large-amplitude Love and Rayleigh waves that lead to a maximum horizontal peak-to-peak displacement of 3.6 m and a maximum peak-to-peak velocity of 4.2 m/sec. The mildest shaking (a maximum peak-to-peak velocity of 1.7 m/sec) occurs for pure thrust motion on a 30 degree dipping fault because the rupture propagates primarily in the mode-III direction (in-plane direction perpendicular to slip). This case closely matches the fault geometry of the 1999 Chi-Chi earthquake and implies that a different style of faulting with a similar hypocenter would have led to large-amplitude ground motions over a broader area.

Shifting the hypocenter toward the bottom center of the fault results in less variation in the level of shaking across the five pairs of fault dip and slip rake angles considered. The bilateral nature of the ruptures reduces the ground motions for scenarios with predominantly strike-slip faulting, while the larger amount of up-dip rupture increases the ground motions for scenarios with predominantly thrust faulting. This means a deeper hypocenter in the Chi-Chi earthquake would have also likely increased the area subject to severe shaking.

Similar mean maximum horizontal peak-to-peak velocities are found on the down-dip side of the fault across all of the scenarios, particularly for bilateral rupture. On the up-dip side of the fault, local extrema in the maximum peak-to-peak displacements and velocities produce a complex decay in the mean maximum peak-to-peak values with distance from the fault. For example, in the case of the 30 degree dipping fault with pure thrust motion, the mean peak-to-peak displacements drop dramatically from the hanging wall to the footwall before gradually decaying with distance from the fault.

The variations in the level of shaking are also evident in the horizontal acceleration response spectra. For each scenario the spatial distribution of the response spectra becomes smoother as the period increases due to the longer wavelengths, but the spectra maintain the same general shape at periods of 2.0 to 5.0 seconds. The largest response spectra values occur for the 60 degree dipping fault, which has a slip rake angle of 45 degrees, and approach 1 g at several locations. The response spectra for the 30 degree dipping fault are much smaller, particularly in the case of the hypocenter located mid-depth one quarter of the way along the strike of the fault.

These simulations suggest that while the ground motions in the 1999 Chi-Chi earthquake in Taiwan may have been large, they were at the low range for the size of the event due to the shallow hypocenter and predominantly unilateral rupture on the shallow dipping fault with mostly thrust motion. Consequently, severe long-period ground motions should be expected over a much larger area when events of the same size occur with other styles of faulting or deeper hypocenters.

References

Aagaard, B. T. (1999). Finite-element simulations of earthquakes. Technical Report 99-03, California Institute of Technology, Earthquake Engineering Research Laboratory, Pasadena, CA.

Aagaard, B. T., J. F. Hall, and T. H. Heaton (2001, May). Characterization of near-source ground motions with earthquake simulations. *Earthquake Spectra 17*(2), 177–207.

Aagaard, B. T., T. H. Heaton, and J. F. Hall (2001, December). Dynamic earthquake ruptures in the presence of lithostatic normal stresses: Implications for friction models and heat production. *Bulletin of the Seismological Society of America 91*(6), 1765–1796.

Allen, C. R., J. R. Brune, L. S. Cluff, and A. G. Barrows (1998, November/December). Evidence for unusually strong near-field ground motion on the hanging wall of the San Fernando fault during the 1971 earthquake. *Seismological Research Letters 69*(6), 524–531.

Andrews, D. (1976, November 10). Rupture velocity of plane strain shear cracks. *Journal of Geophysical Research 81*(32), 5679–5687.

Archuleta, R. J., and G. A. Frazier (1978, June). Three-dimensional numerical simulations of dynamic faulting in a half-space. *Bulletin of the Seismological Society of America 68*(3), 541–572.

Archuleta, R. J., and S. H. Hartzell (1981, August). Effects of fault finiteness on near-source ground motion. *Bulletin of the Seismological Society of America 71*(4), 939–957.

Day, S. M. (1982, December). Three-dimensional simulation of spontaneous rupture: The effect of nonuniform prestress. *Bulletin of the Seismological Society of America 72*(6), 1881–1902.

Graves, R. W. (1998, August). Three-dimensional finite-difference modeling of the San Andreas fault: Source parameterization and ground-motion levels. *Bulletin of the Seismological Society of America 88*(4), 881–897.

Haskell, N. (1969, April). Elastic displacements in the near-field of a propagating fault. *Bulletin of the Seismological Society of America 59*(2), 865–908.

Heaton, T. H. (1990, November). Evidence for and implications of self-healing pulses of slip in earthquake rupture. *Physics of the Earth and Planetary Interiors 64*(1), 1–20.

Hisada, Y., H. Bao, J. Bielak, O. Ghattas, and D. O'Hallaron (1998, December). Simulations of long-period ground motions during the 1995 Hyogo-Ken Nanbu (Kobe) earthquake using a 3-D finite element method. In *2nd International Symposium on Effect of Surface Geology on Seismic Motion*, Yokohama, Japan, pp. 59–66.

Huang, B., K. Chen, W. Huang, J. Wang, T. Chang, R. Hwang, H. Chiu, and C. Tsai (2000, September 1). Characteristics of strong ground motion across a thrust fault tip from the September 21, 1999, Chi-Chi, Taiwan earthquake. *Geophysical Research Letters 27*(17), 2729–2732.

ICBO (1997). *Uniform Building Code*. Whittier, CA: International Conference of Building Officials (ICBO).

Inoue, T., and T. Miyatake (1998, December). 3-D simulation of near-field strong ground motion based on dynamic modeling. *Bulletin of the Seismological Society of America 88*(6), 1445–1456.

Iwan, W., and X. Chen (1994). Important near-field ground motion data from the Landers earthquake. In *Proceedings of the 10th European Conference on Earthquake Engineering*, Volume 1, Vienna, pp. 229–234.

Ji, C., D. V. Helmberger, D. J. Wald, and K. Ma. Slip history and dynamic implication of the 1999 Chi-Chi earthquake. *Journal of Geophysical Research - Solid Earth*. Submitted.

Johnson, K., Y. Hsu, P. Segall, and S. Yu (2001, June 1). Fault geometry and slip distribution of the 1999 Chi-Chi, Taiwan earthquake imaged from inversion of GPS data. *Geophysical Research Letters 28*(11), 2285–2288.

Kamae, K., and K. Irikura (1998, April). Source model of the 1995 Hyogo-Ken Nanbu earthquake and simulation of near-source ground motion. *Bulletin of the Seismological Society of America 88*(2), 400–412.

Ma, K., T. Song, S. Lee, and H. Wu (2000, October 15). Spatial slip distribution of the September 20, 1999, Chi-Chi, Taiwan, earthquake (m(w)7.6) — Inverted from teleseismic data. *Geophysical Research Letters 27*(20), 3417–3420.

Ma, K., J. Wang, and D. Zhao (1996). Three-dimensional seismic velocity structure if the crust and uppermost mantle beneath Taiwan. *Journal of Physical Earth 44*(2), 85–105.

Ma, K.-F., J. Mori, S.-J. Lee, and S. Yu (2001). Spatial and temporal distribution of slip for the 1999 Chi-Chi, Taiwan, earthquake. *Bulletin of the Seismological Society of America 91*(5), 1069–1087.

Madariaga, R., K. Olsen, and R. Archuleta (1998, October). Modeling dynamic rupture in a 3-D earthquake fault model. *Bulletin of the Seismological Society of America 88*(5), 1182–1197.

Oglesby, D. D., R. J. Archuleta, and S. B. Nielsen (2000, June). The three-dimensional dynamics of dipping faults. *Bulletin of the Seismological Society of America 90*(3), 616–628.

Olsen, K., and R. Archuleta (1996, June). Three-dimensional simulation of earthquakes on the Los Angeles fault system. *Bulletin of the Seismological Society of America 86*(3), 575–596.

Olsen, K., R. Madariaga, and R. Archuleta (1997, October 31). Three-dimensional dynamic simulation of the 1992 Landers earthquake. *Science 278*, 834–839.

Olsen, K. B., R. J. Archuleta, and J. R. Matarese (1995, December 8). Three-dimensional simulation of a magnitude-7.75 earthquake on the San-Andreas Fault. *Science 270*(5242), 1628–1632.

Pitarka, A., K. Irikura, T. Iwata, and S. Sekiguchi (1998, April). Three-dimensional simulation of the near-fault ground motion for the 1995 Hyogo-ken Nanbu (Kobe), Japan, earthquake. *Bulletin of the Seismological Society of America 88*(2), 428–440.

Somerville, P. G., N. F. Smith, R. W. Graves, and N. A. Abrahamson (1997, January/February). Modification of empirical strong ground motion attenuation relations to include the amplitude and duration effects of rupture directivity. *Seismological Research Letters 68*(1), 199–222.

Wells, D., and K. Coppersmith (1994, August). New empirical relationships among magnitude, rupture length, rupture width, rupture area, and surface displacement. *Bulletin of the Seismological Society of America 84*(4), 974–1002.

Appendix A Summary of Computational Requirements

The mesh resolution, the size of the domain, and the material properties (shear and dilatational wave speeds) dictate the computational requirements. The lengths of the propagating waves govern the size of the elements with linear tetrahedral elements requiring a node spacing of 10% of the wavelength. The spatial resolution was chosen because it captures waves with periods down to 2.0 sec. The variations of the shear and dilatational wave speeds with depth require a nominal node spacing of 400 m at the ground surface and 800 m at the bottom of the domain. The size of the domain controls the total number of elements. For the 160 km long, 80 km wide, and 40 km deep domain, the finite-element mesh contains 9.0 million elements, 1.7 million nodes, and 5.0 million degrees of freedom. Figure A.1 shows the mesh at a coarse resolution where the node spacing is four times larger than that used in the simulation.

The simulations require 3.7 gigabytes of memory along with millions of floating point operations. Consequently, parallel processing was used to distribute the memory and computational burdens across multiple processors. The single-program, multiple-data (SPMD) parallel-processing model was followed, where each processor executes the same code with a different portion of the data. The Message Passing Interface (MPI) was used to implement the parallel processing of the computation and the input/output.

Currently the simulations are run on the Hewlett Packard V-Class supercomputer at Caltech's Center for Advanced Computing Research. This machine contains 128 400MHz HP PA-8500 64-bit RISC processors with 128 gigabytes of total memory. Using 16 processors each of the simulations with 2400 time steps took 2.0 hours.

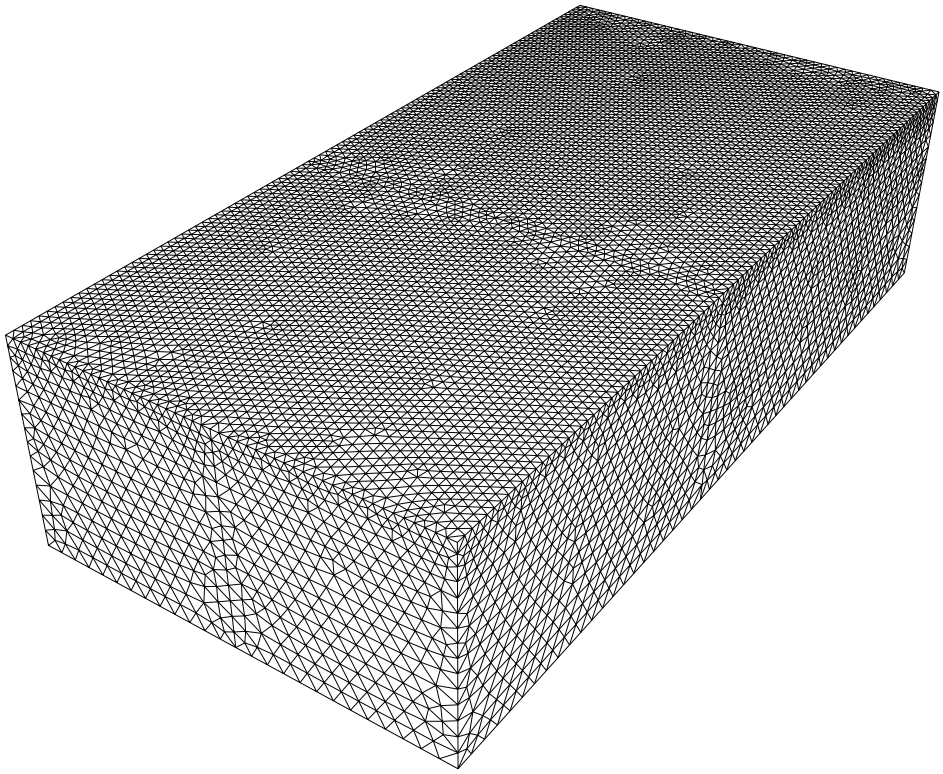

Fig. A.1. Finite-element mesh at coarse resolution for the domain with the 90 degree dipping fault. The mesh for the simulation has a node spacing that is four times smaller than the one shown.

Appendix B Maximum Displacements and Velocities

The plots below show the maximum peak-to-peak horizontal displacements and velocities on the ground surface. The thick solid line indicates the surface tract of the fault, the thick dashed line shows the projection of the buried edges of the fault, and the asterisk identifies the epicenter.

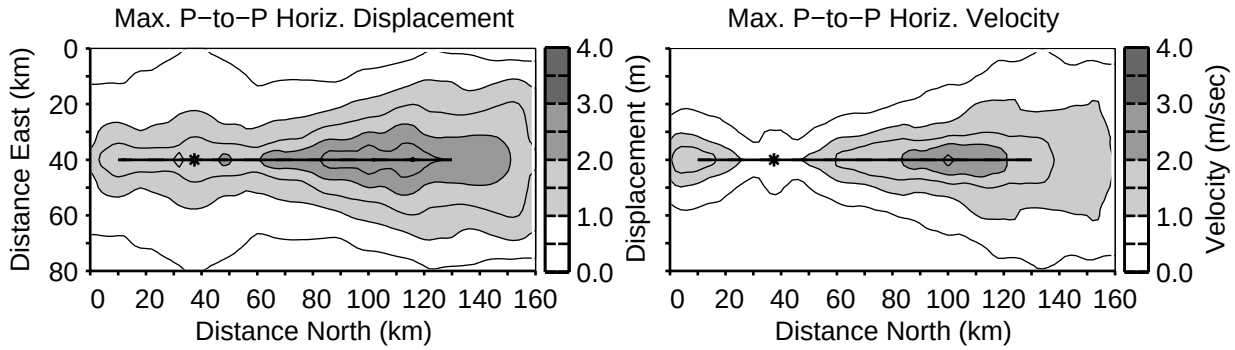

Scenario dip90HA

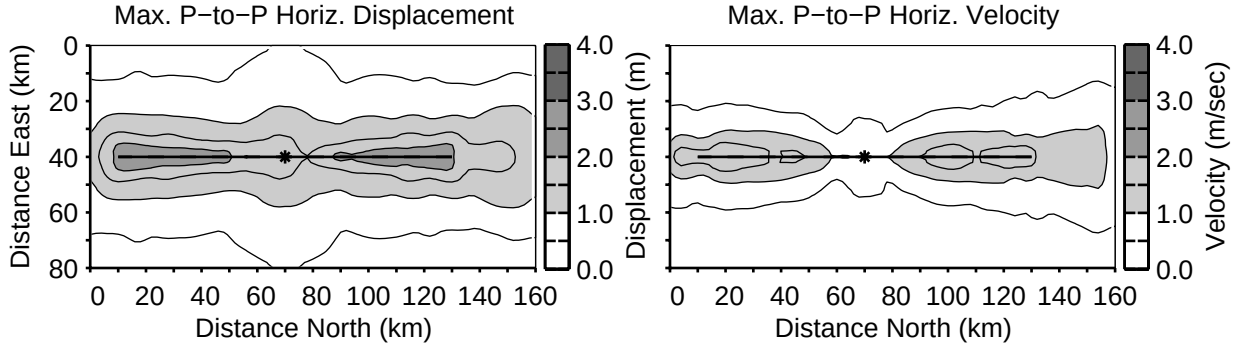

Scenario dip90HB

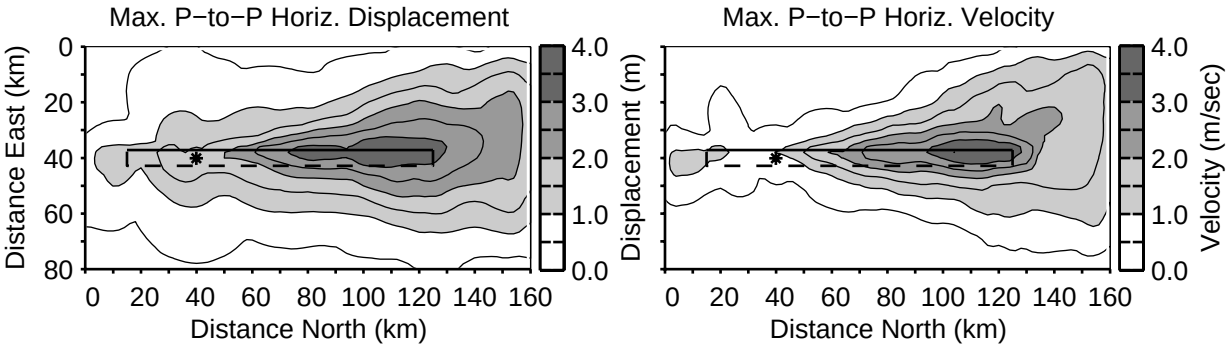

Scenario dip75HA

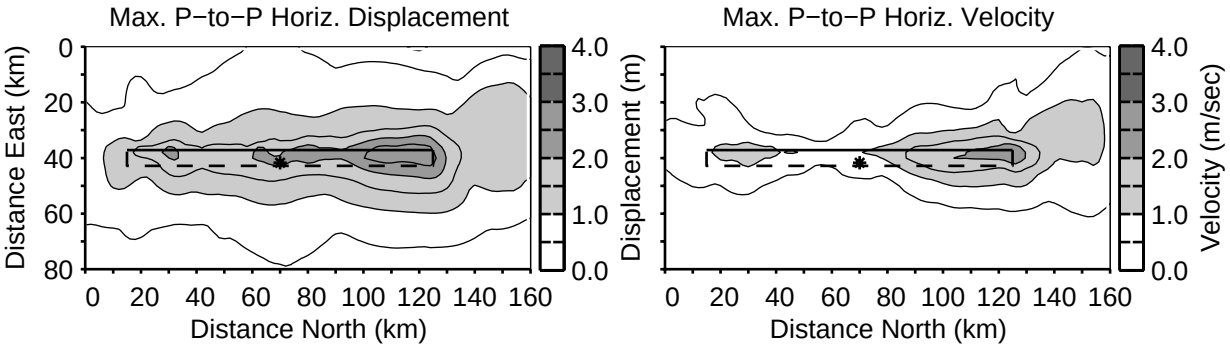

Scenario dip75HB

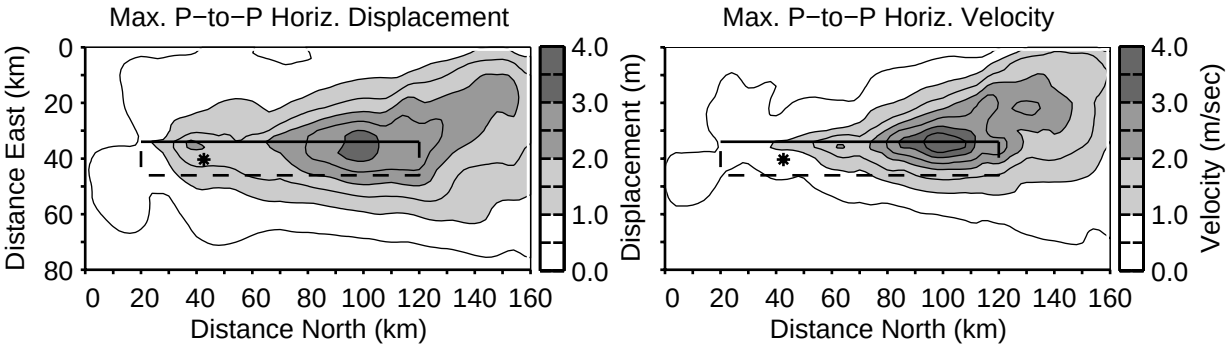

Scenario dip60HA

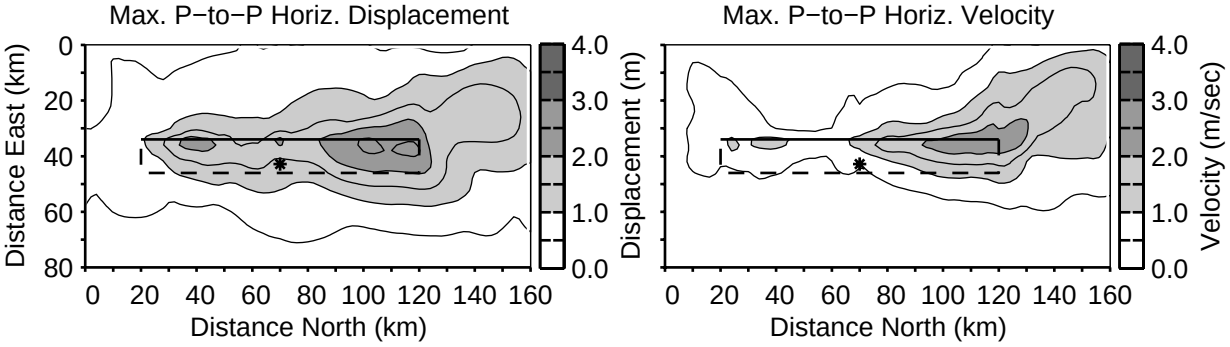

Scenario dip60HB

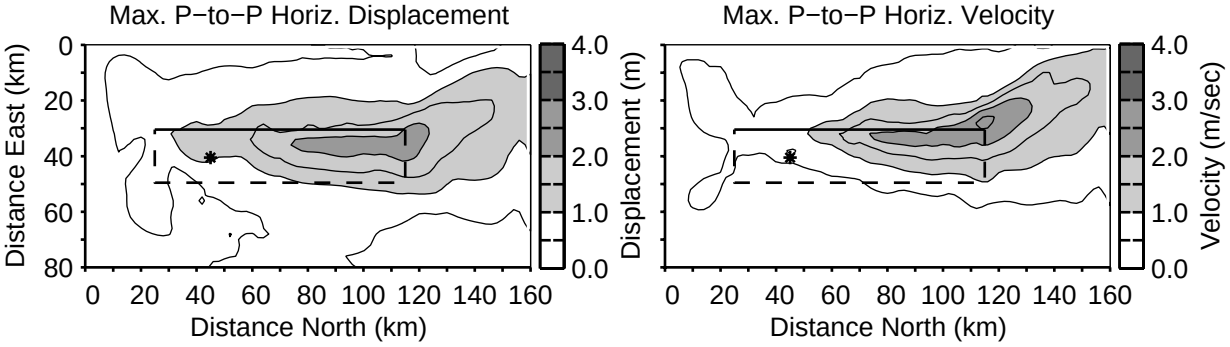

Scenario dip45HA

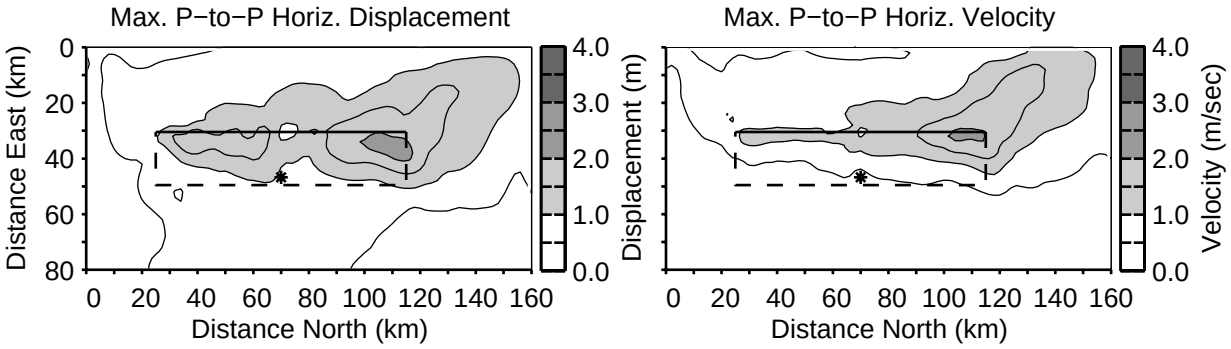

Scenario dip45HB

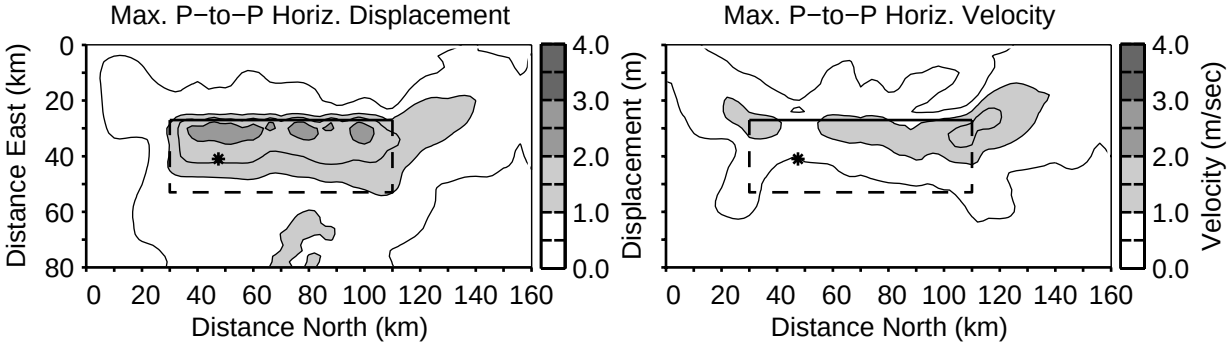

Scenario dip30HA

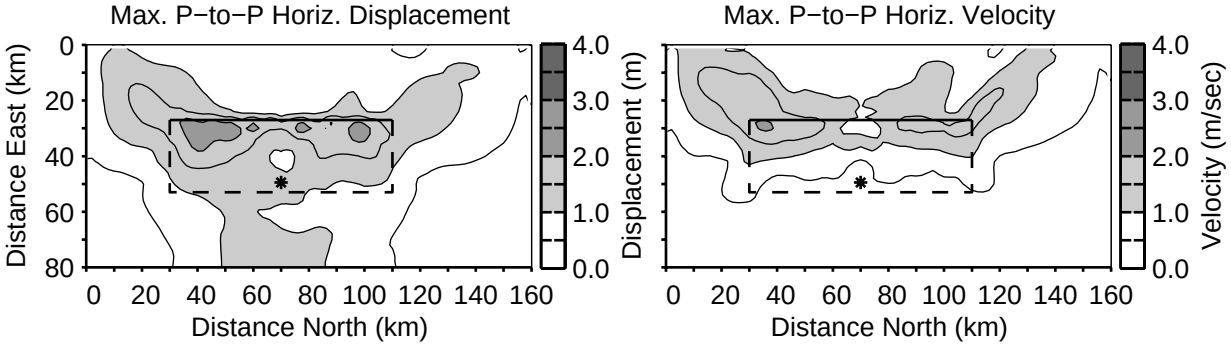

Scenario dip30HB

Appendix C Ground Motion Time Histories

The plots below display the velocity time histories along a north-south line running over the trace of the fault (left plot) and along an east-west line passing over the center of the fault (lower right plot). In each plot the solid line denotes the east-west component, the dashed line denotes the north-south component, and the dash-dotted line denotes the vertical component. The diagram in the upper right identifies the locations of the sites (open circles) relative to the fault trace (solid line), the buried edges of the fault (dashed lines), and the epicenter (asterisk).

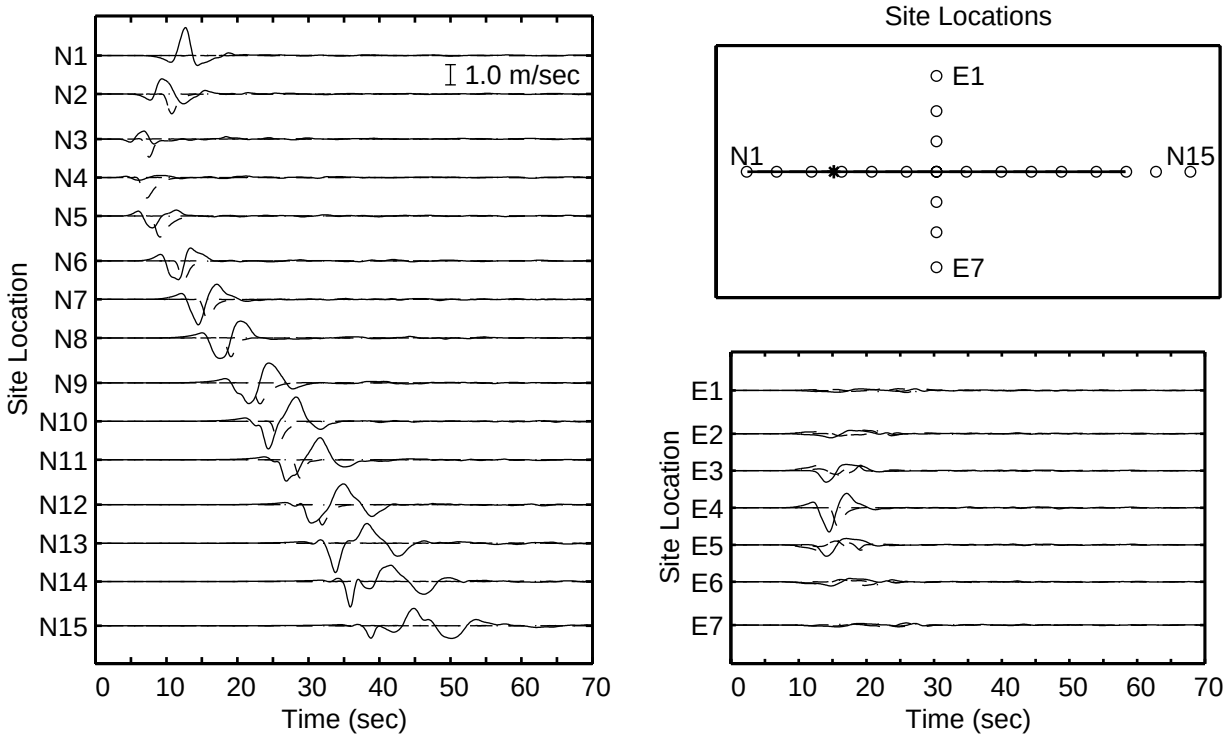

Scenario dip90HA

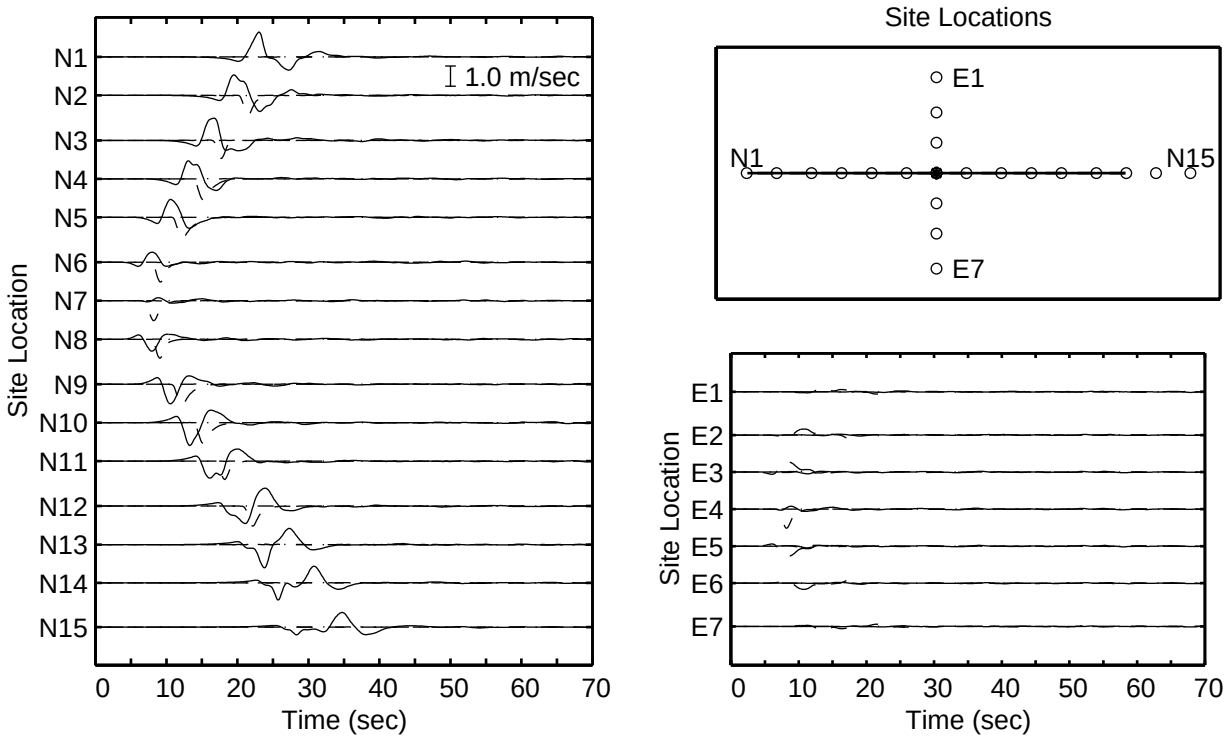

Scenario dip90HB

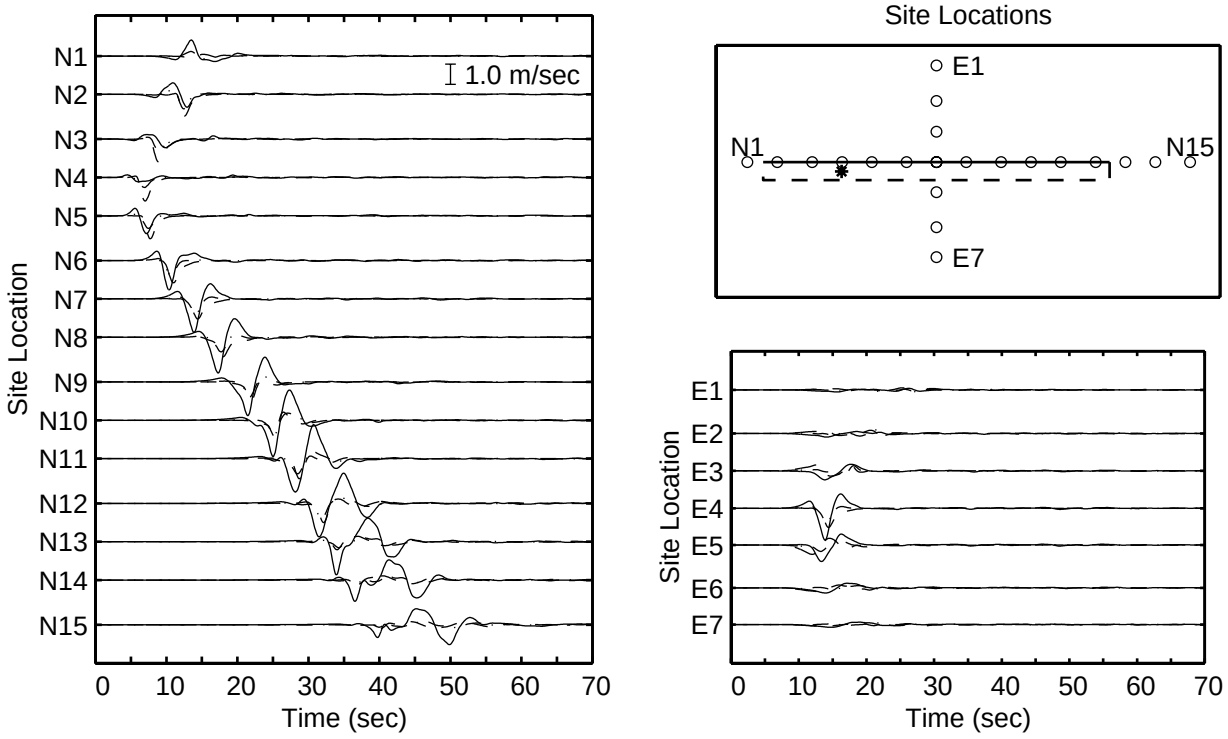

Scenario dip75HA

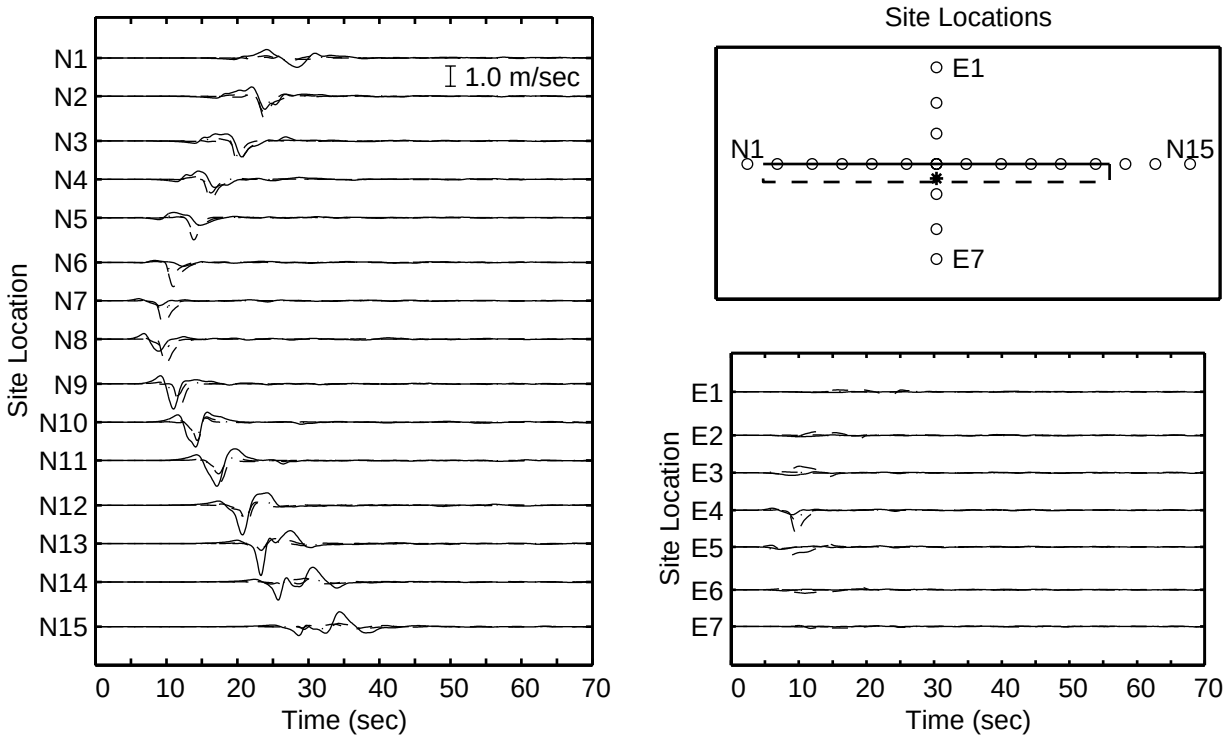

Scenario dip75HB

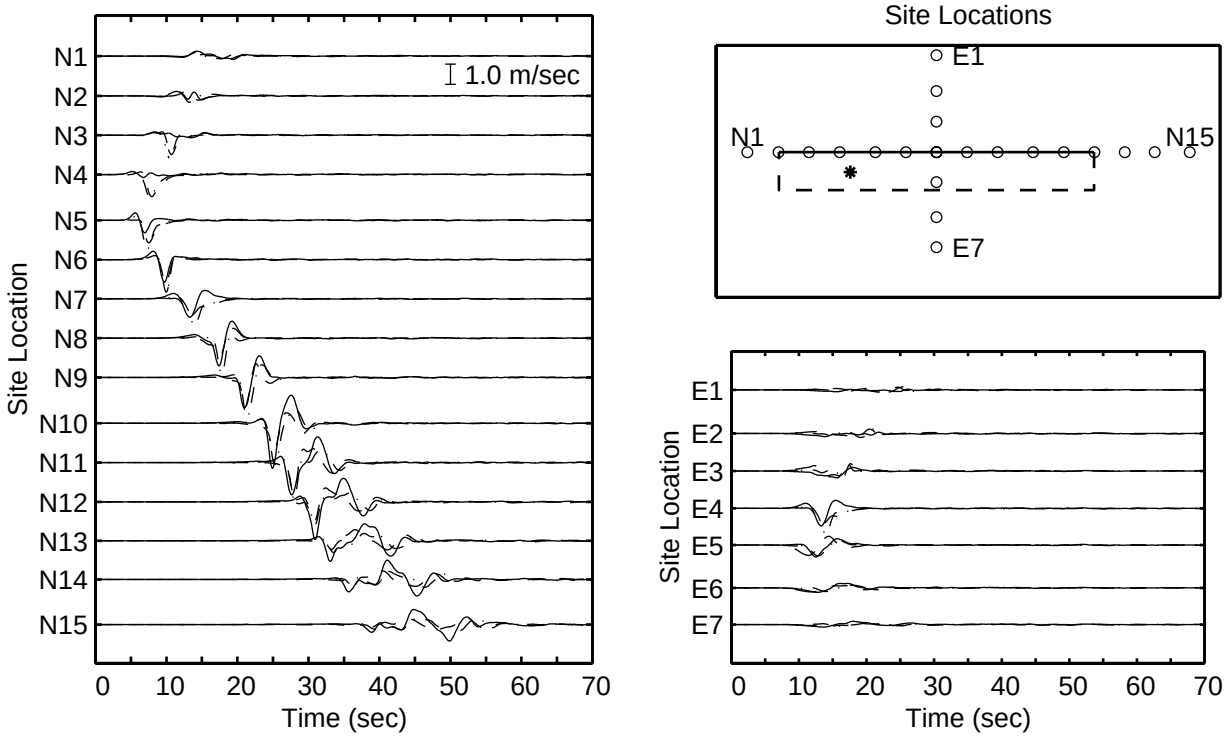

Scenario dip60HA

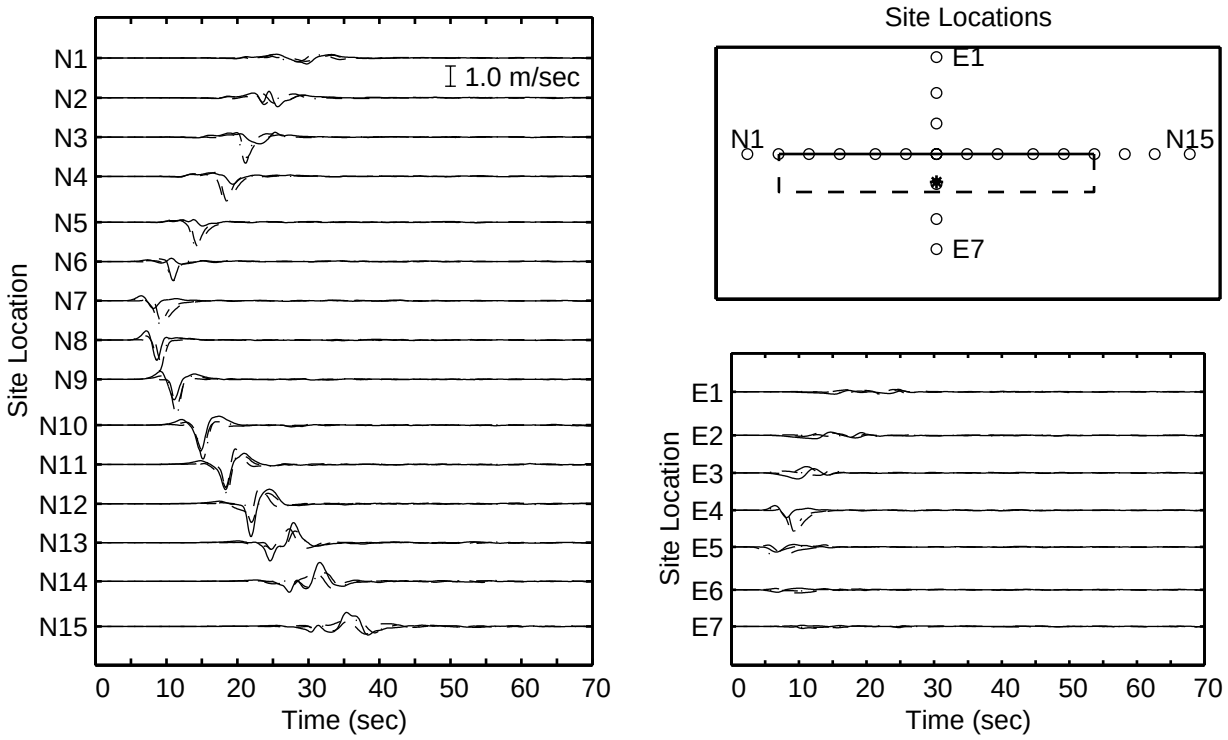

Scenario dip60HB

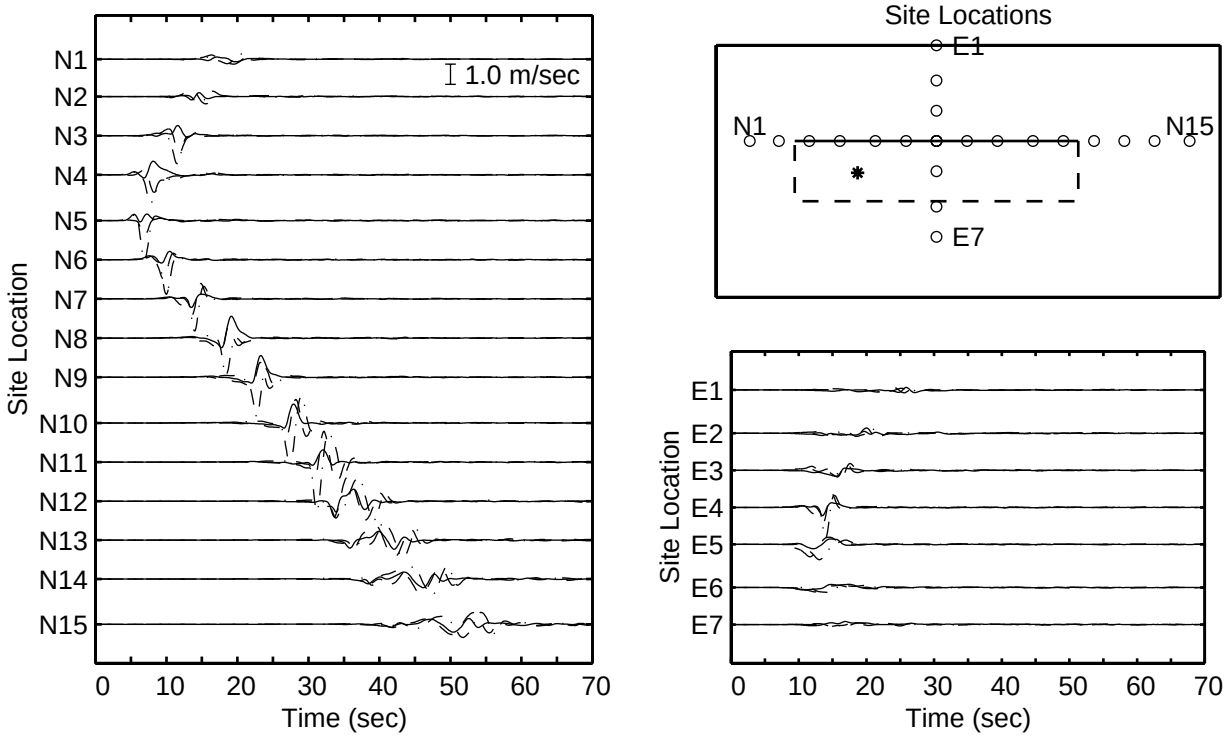

Scenario dip45HA

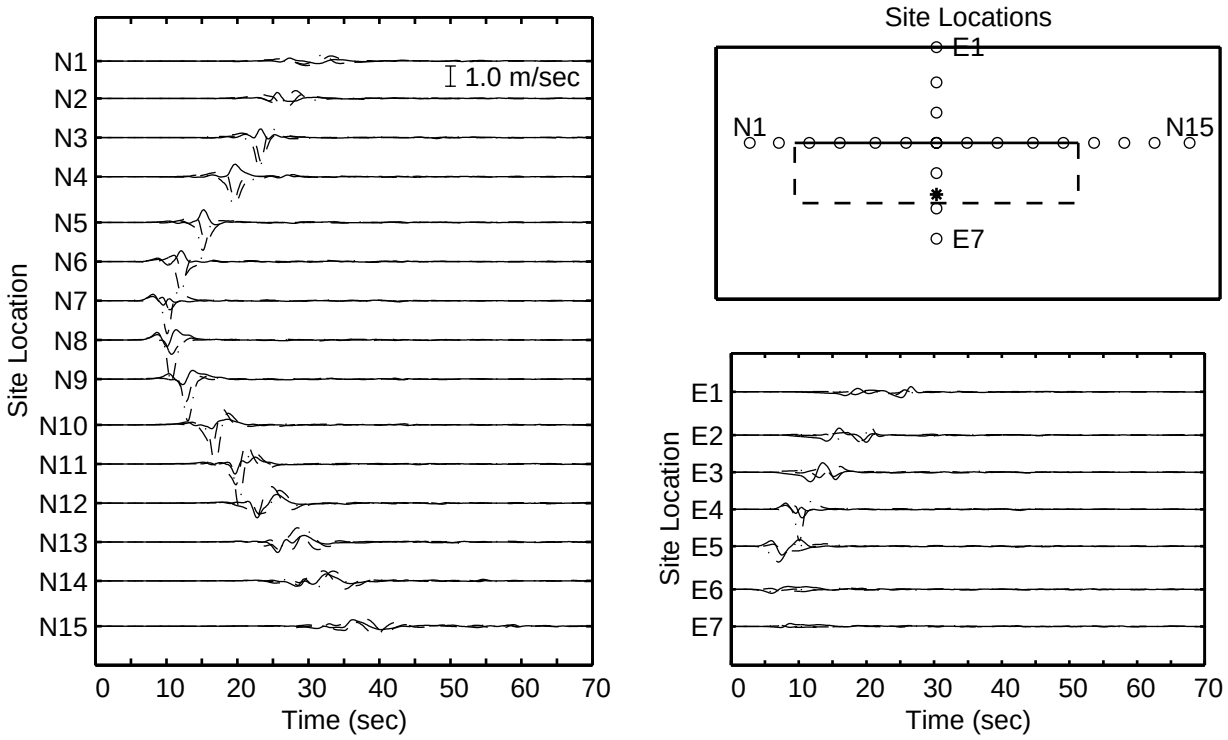

Scenario dip45HB

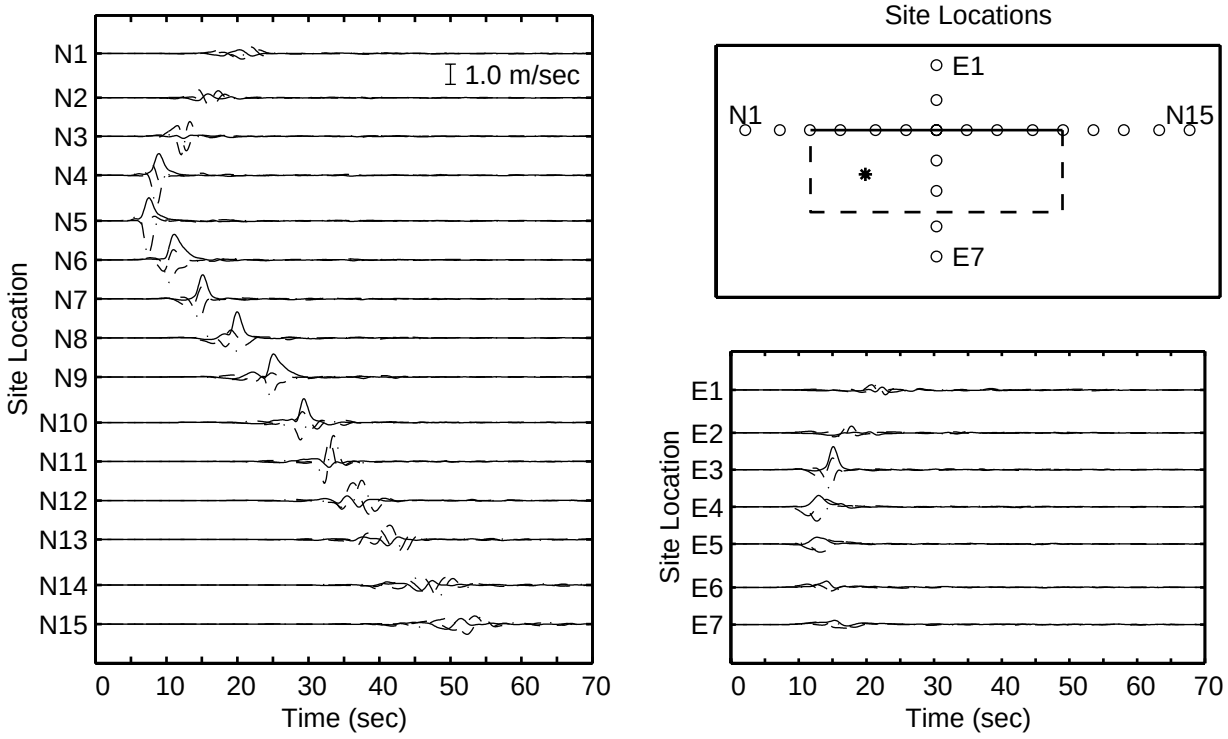

Scenario dip30HA

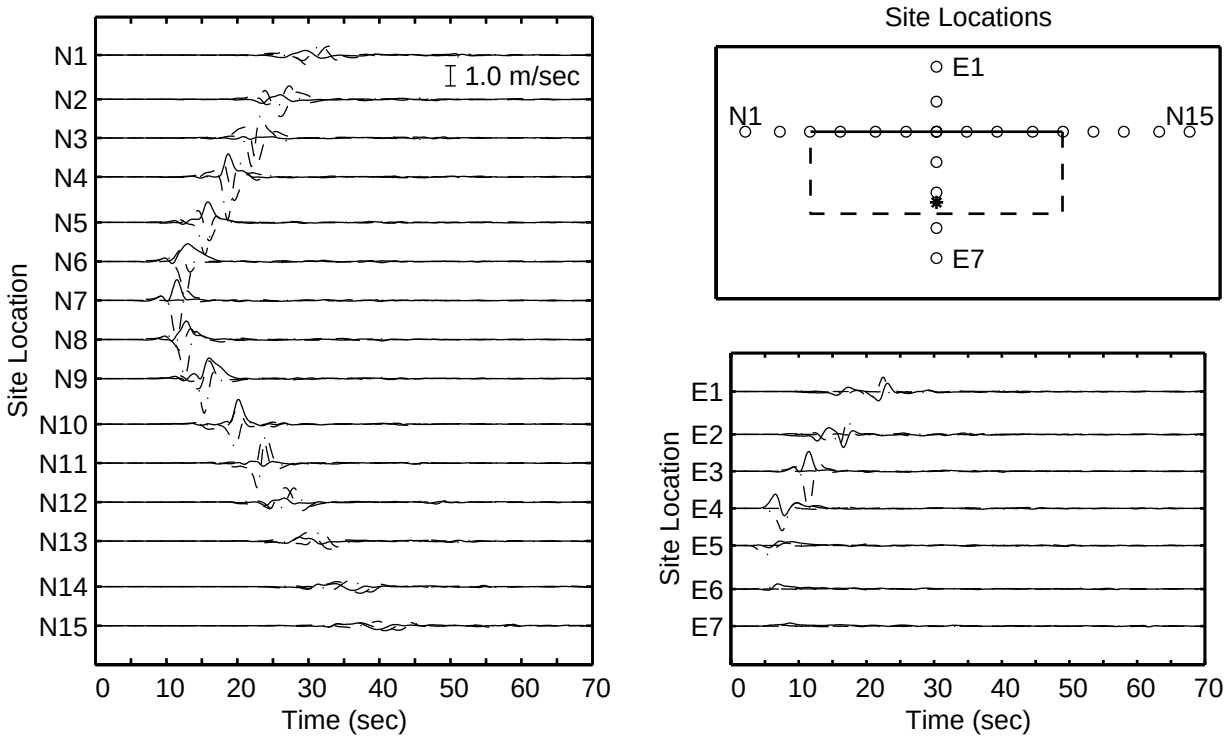

Scenario dip30HB

Appendix D Acceleration Response Spectra

The first series of plots show the horizontal acceleration response spectra on the ground surface for five percent critical damping at four periods. The thick solid line shows the surface trace of the fault, the thick dashed line indicates the surface projection of the buried edges of the fault, and the asterisk identifies the epicenter. The second series of plots display the horizontal acceleration response spectra for each scenario at site N10 for periods from 2.0 to 12 seconds. Site N10 sits on the hanging wall 30 km north of the center of the fault (see figure 2.1).

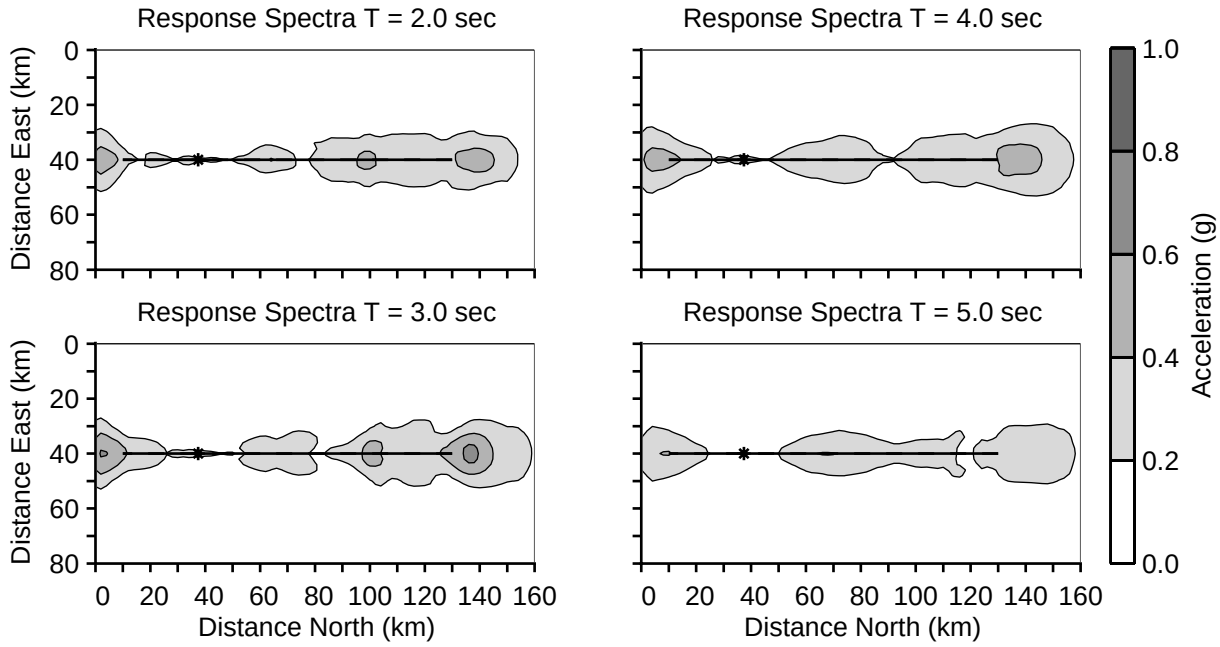

Scenario dip90HA

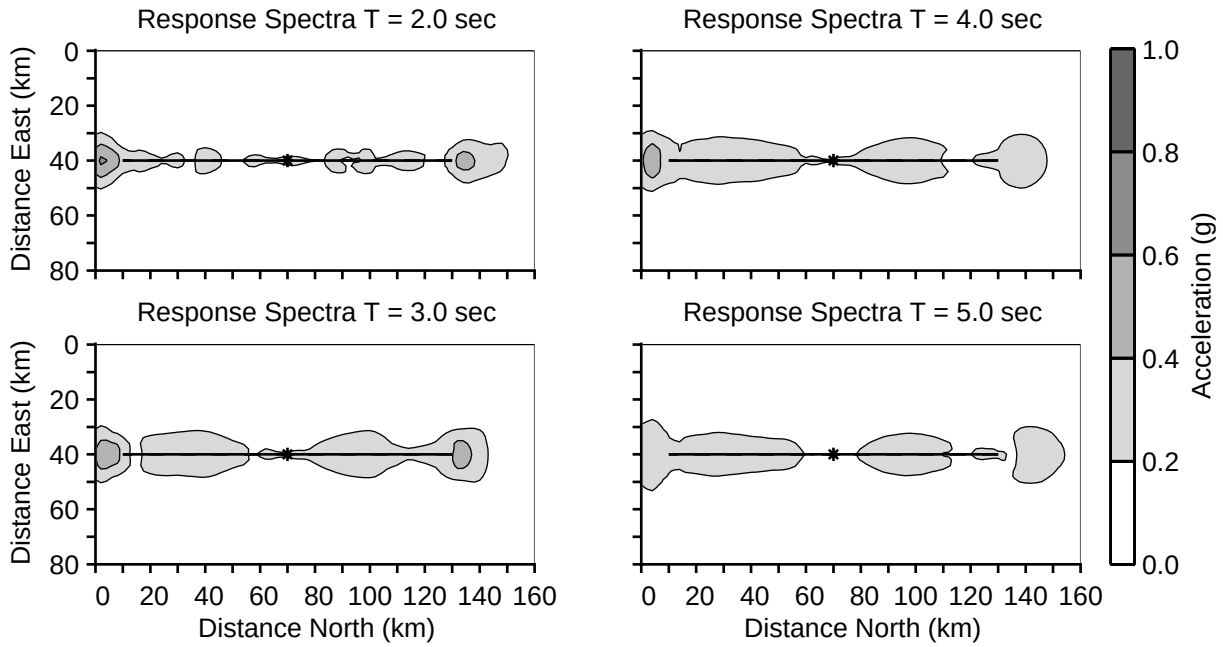

Scenario dip90HB

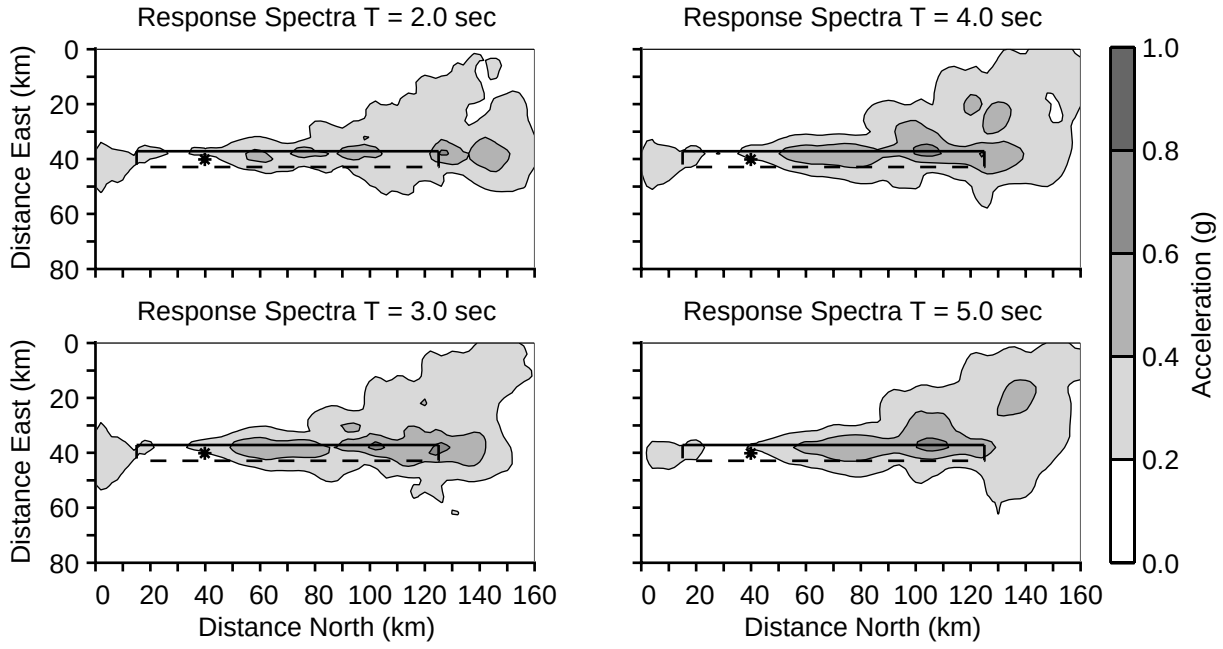

Scenario dip75HA

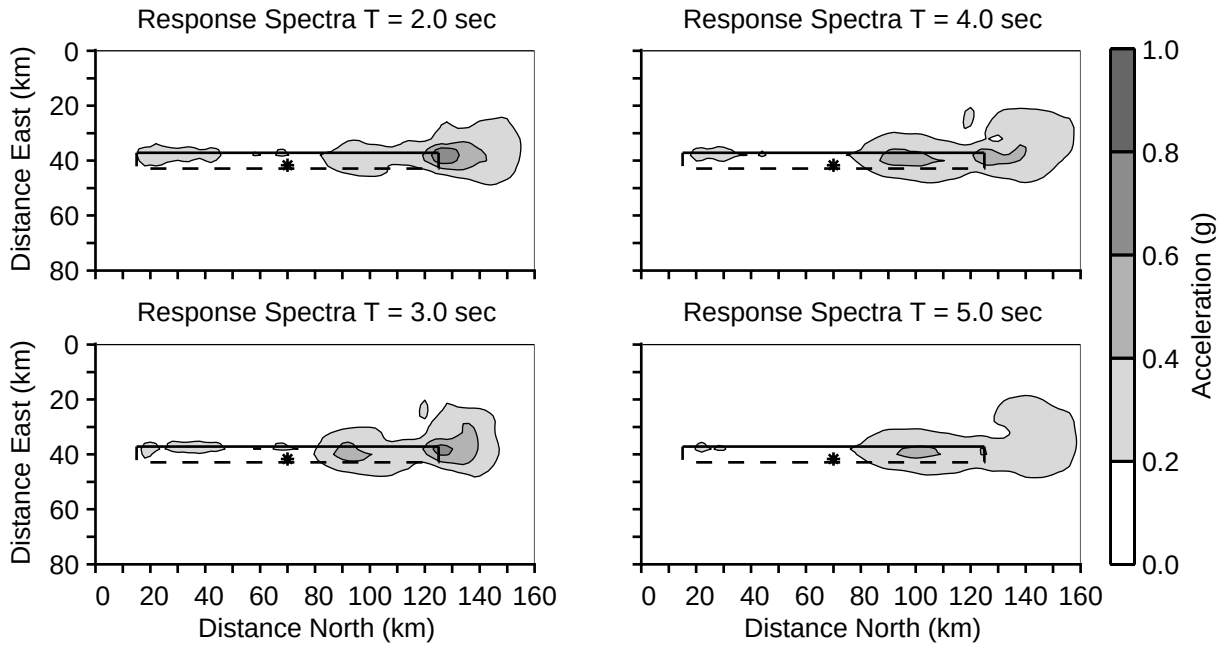

Scenario dip75HB

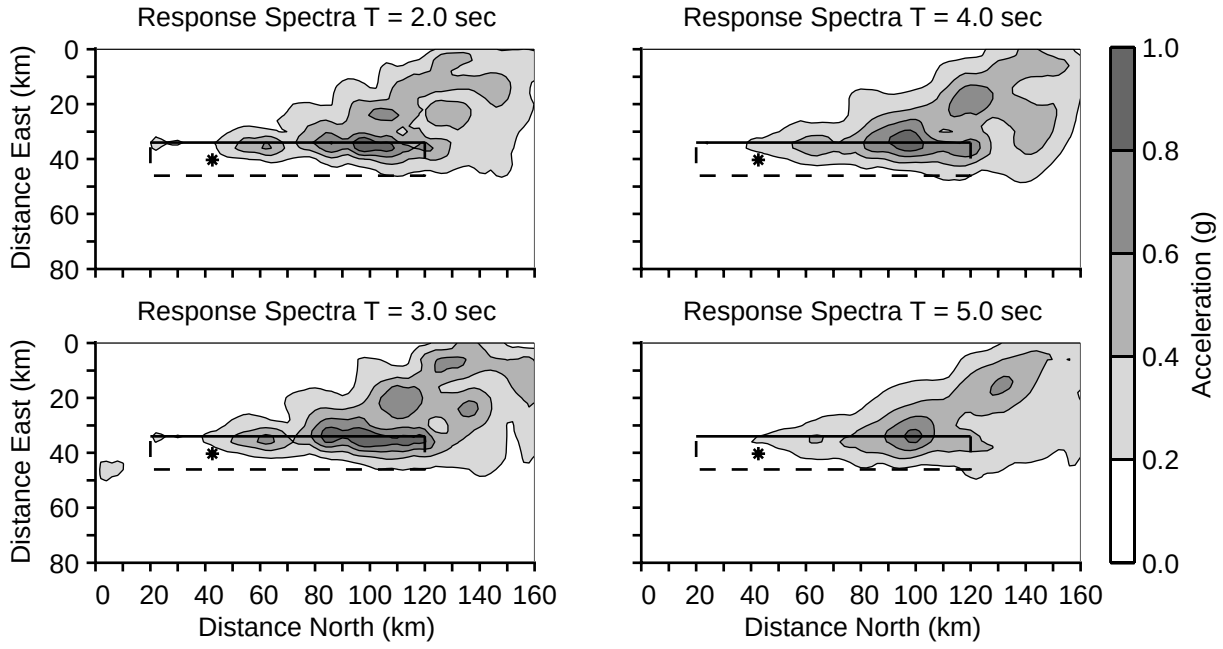

Scenario dip60HA

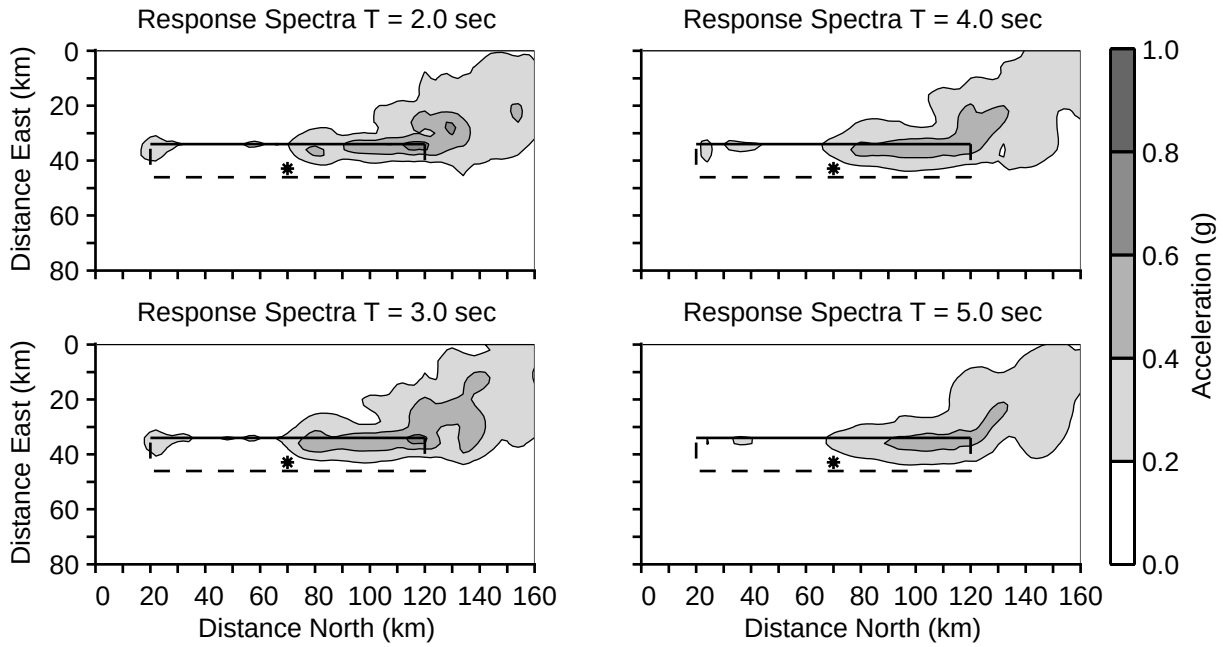

Scenario dip60HB

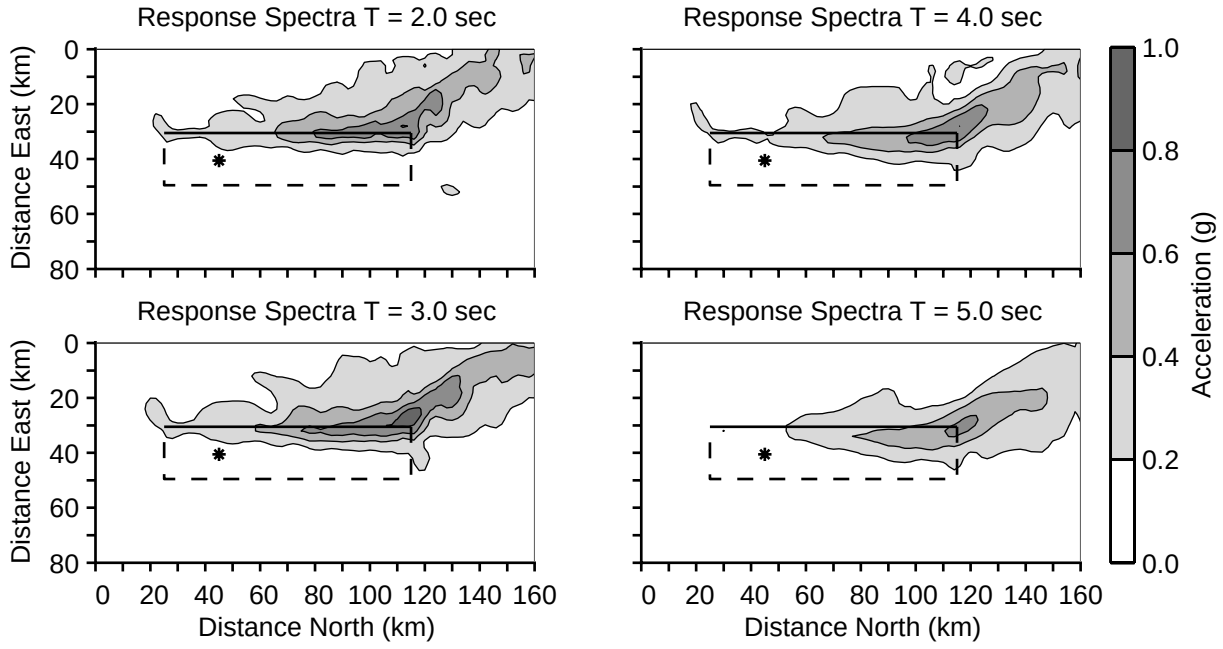

Scenario dip45HA

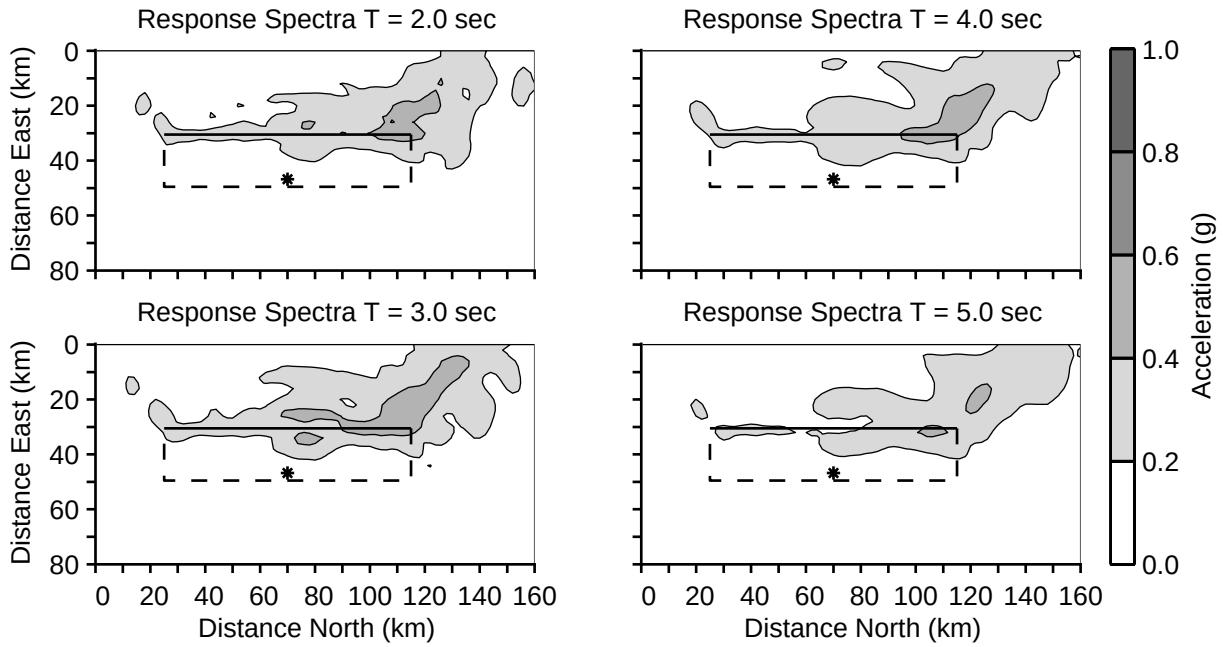

Scenario dip45HB

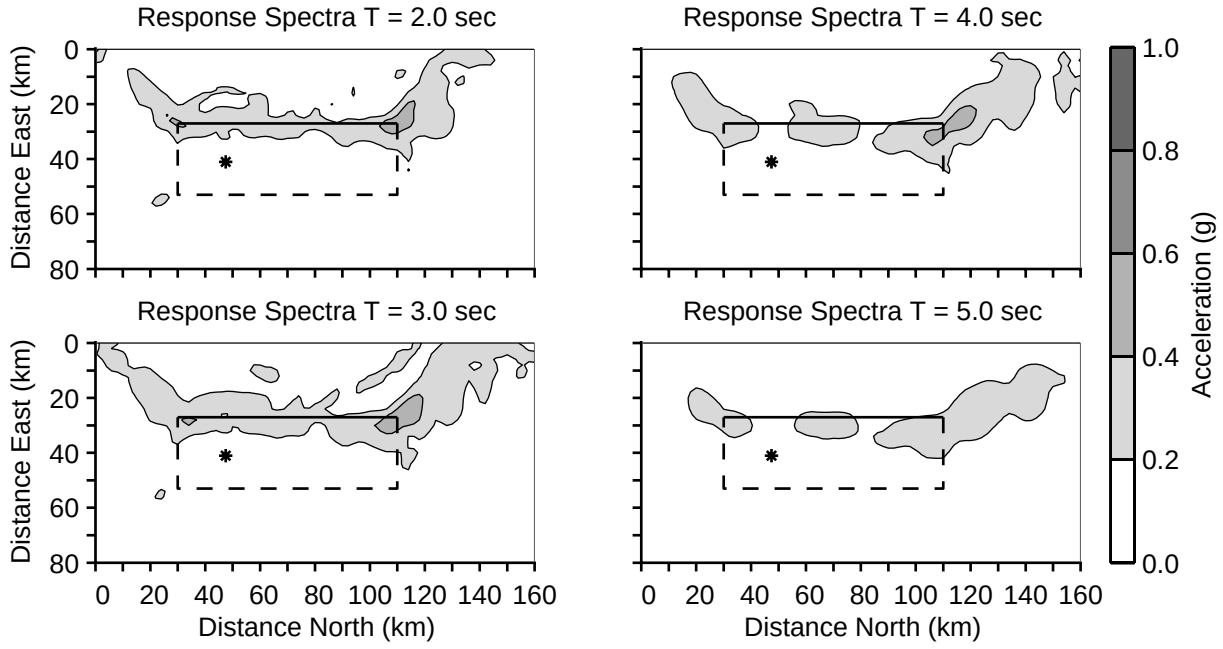

Scenario dip30HA

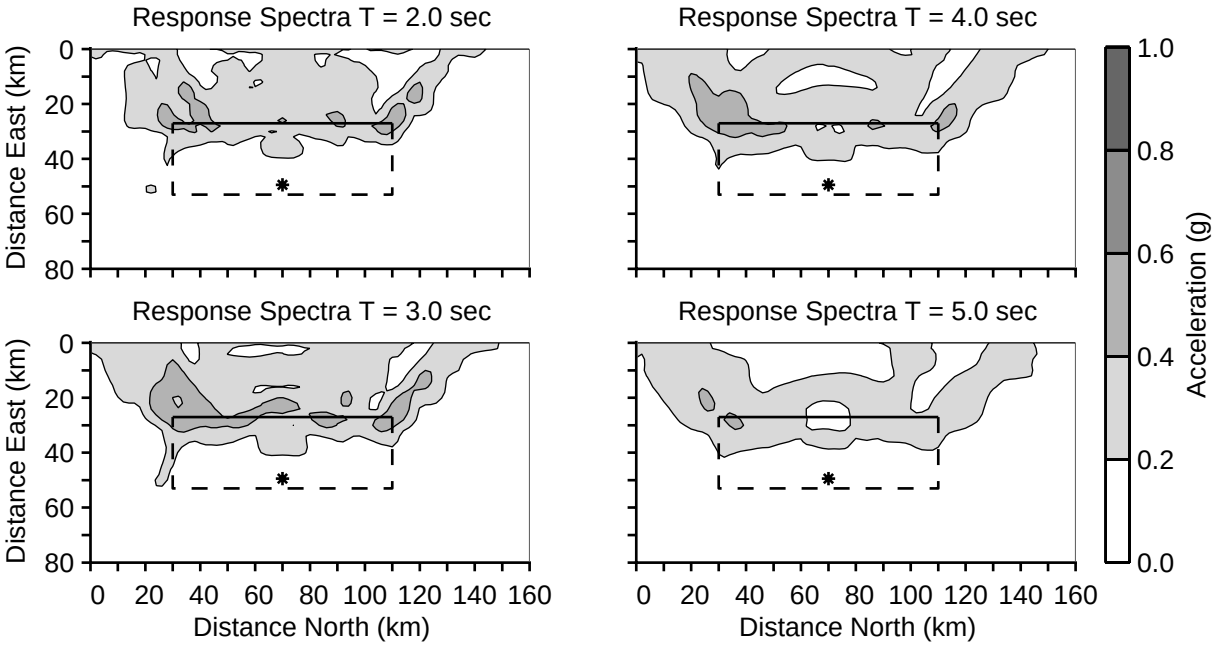

Scenario dip30HB

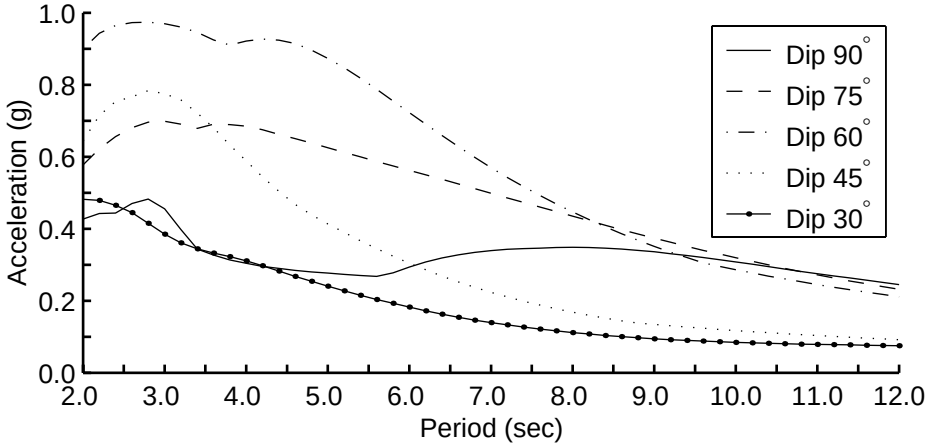

Site N10, Hypocenter HA

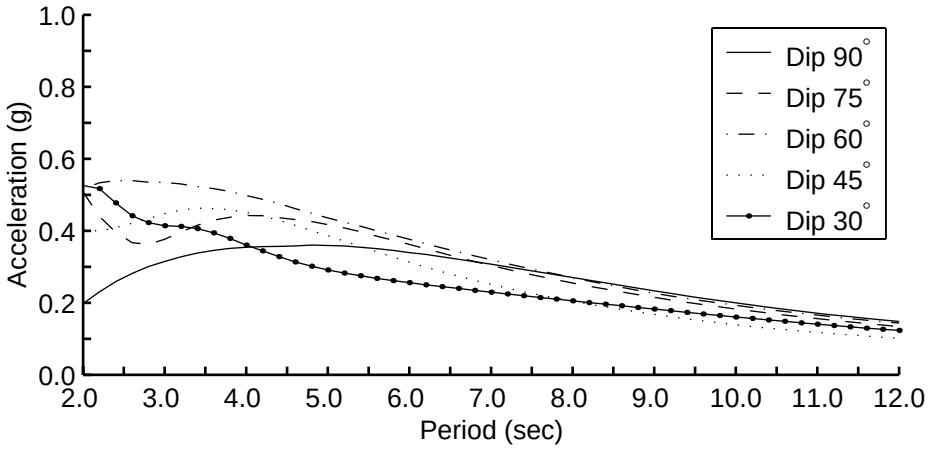

Site N10, Hypocenter HB

Appendix E Area Where Shaking Exceeds Given Level

The plots display the area on the ground surface where the maximum horizontal peak-to-peak displacements (left) and velocities (right) exceed a given value for the two hypocenters for each fault geometry.

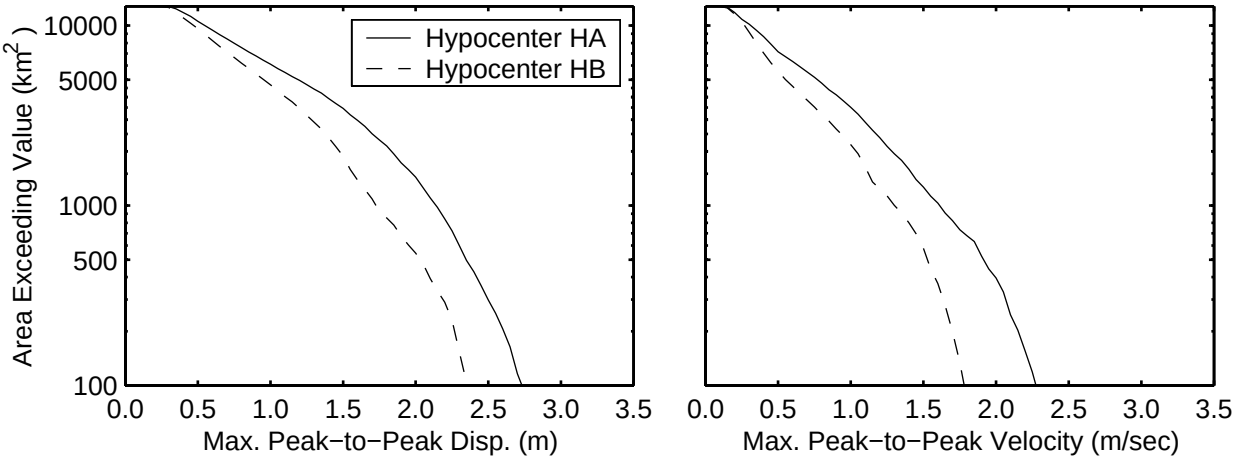

Scenarios dip90HA and dip90HB

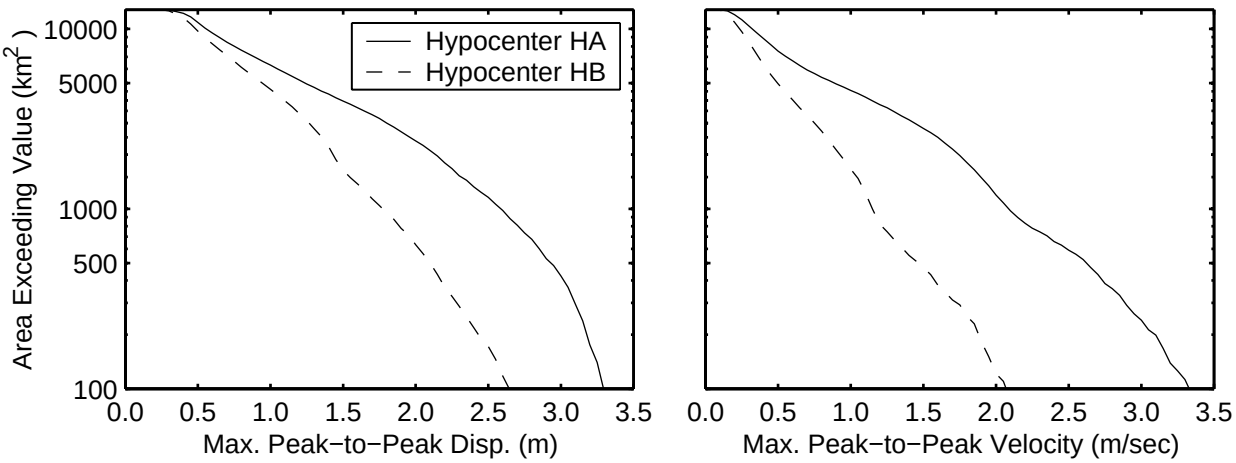

Scenarios dip75HA and dip75HB

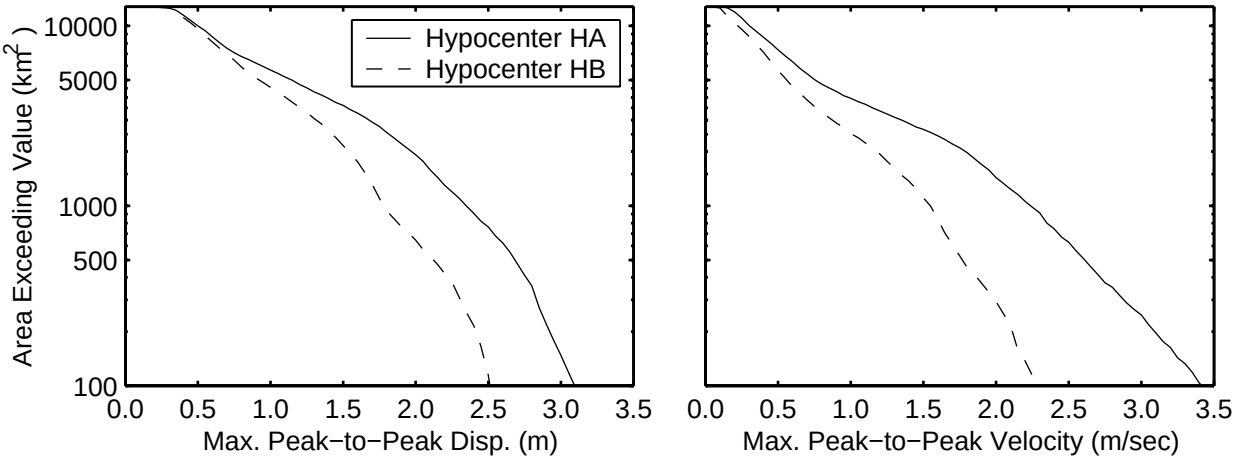

Scenarios dip60HA and dip60HB

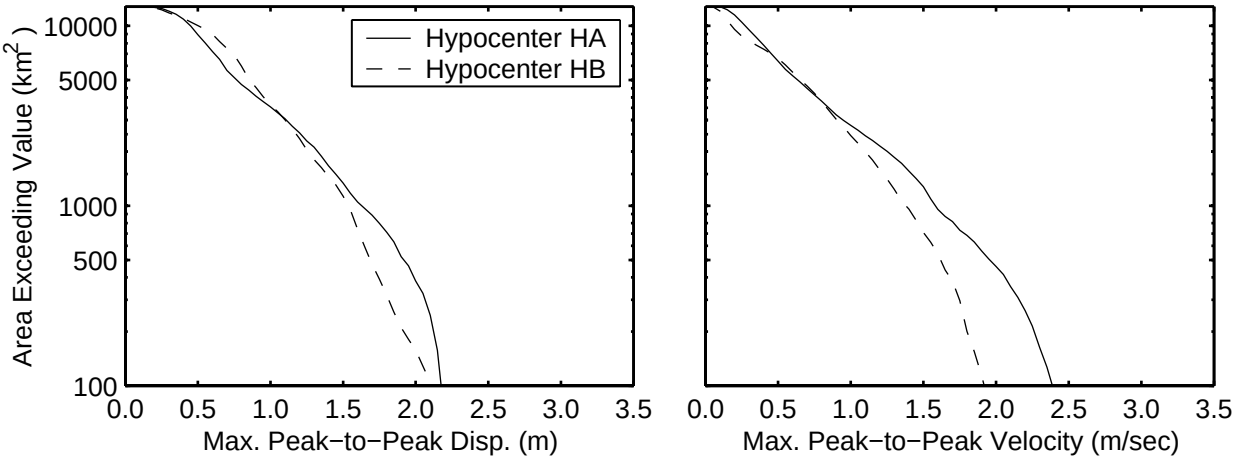

Scenarios dip45HA and dip45HB

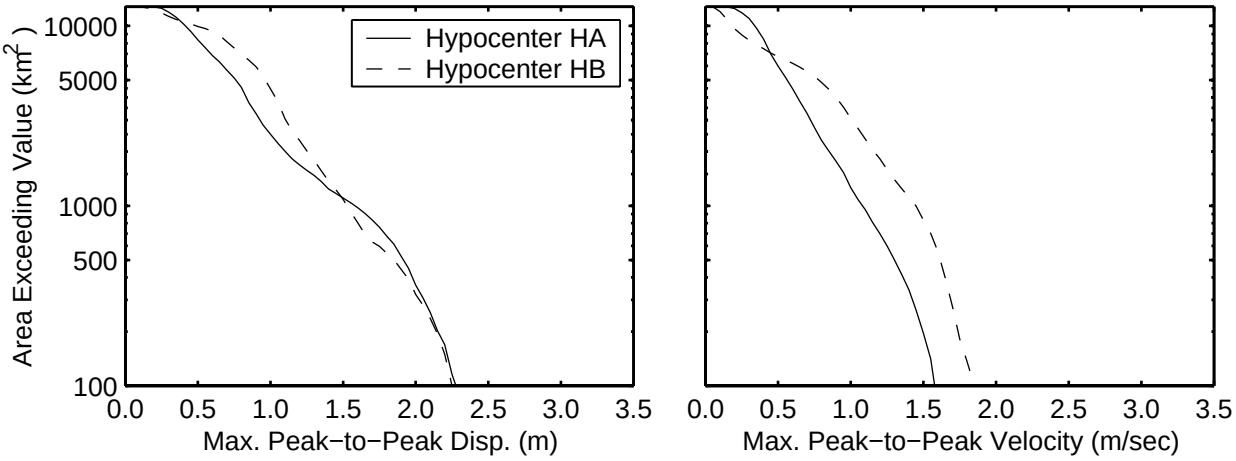

Scenarios dip30HA and dip30HB

Appendix F Maximum Ground Motion versus Distance

The first series of plots gives the maximum horizontal peak-to-peak displacements and velocities as a function of distance from the fault for each scenario. The dots represent the values at locations on the ground surface, the solid line delineates the mean, and the dashed lines correspond to one standard deviation above and below the mean. The vertical dotted lines bound the locations where the UBC near-source factor N_v is largest (inner pair) and smallest (outer pair). The second series displays just the mean and one standard deviation above and below the mean for the two hypocenters for each fault geometry.

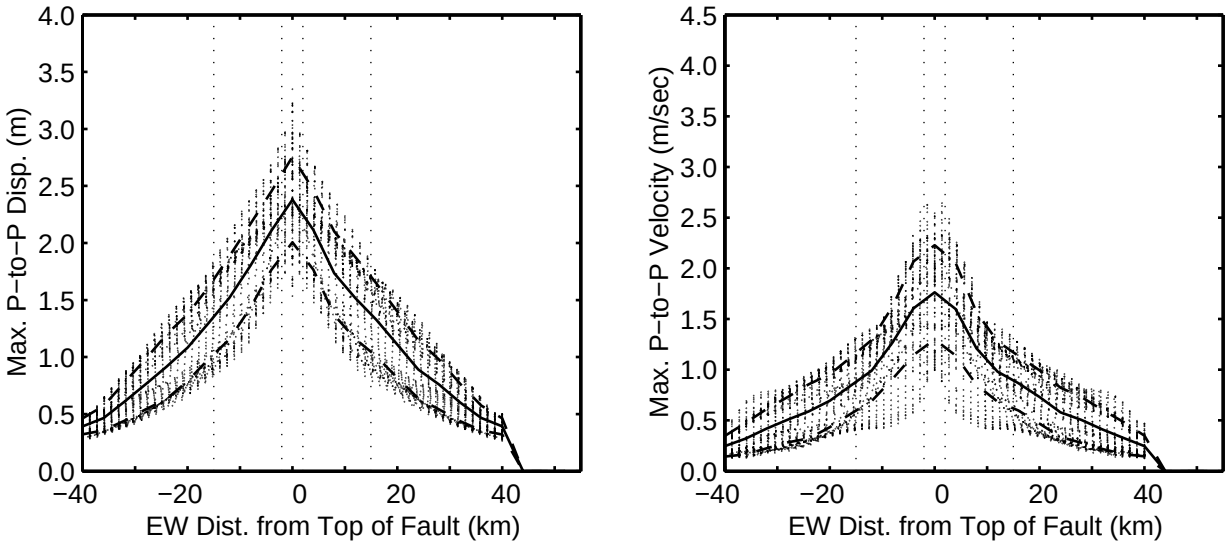

Scenario dip90HA

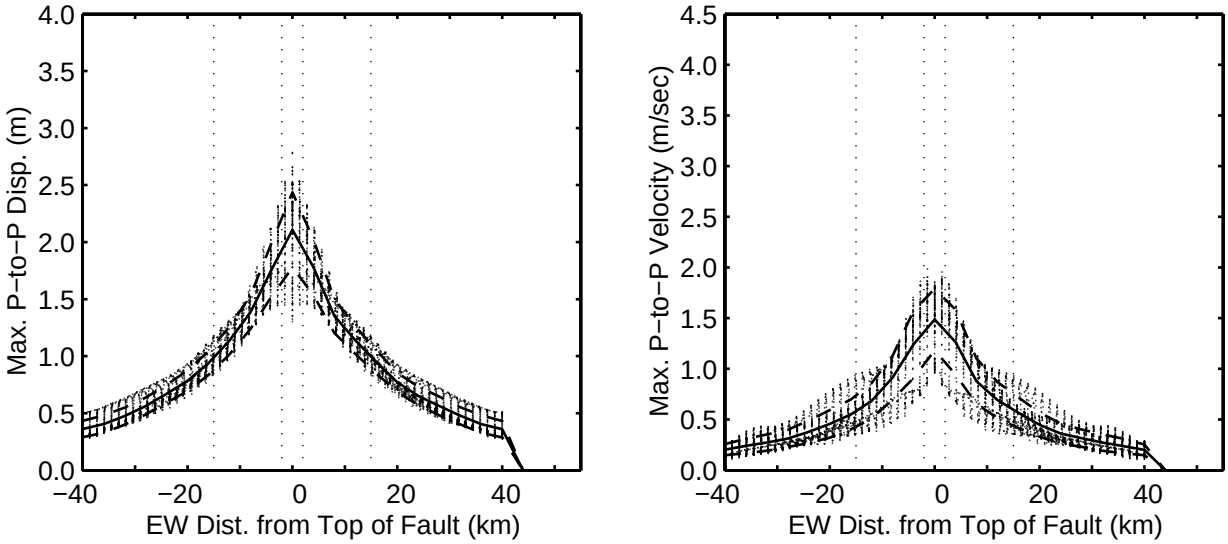

Scenario dip90HB

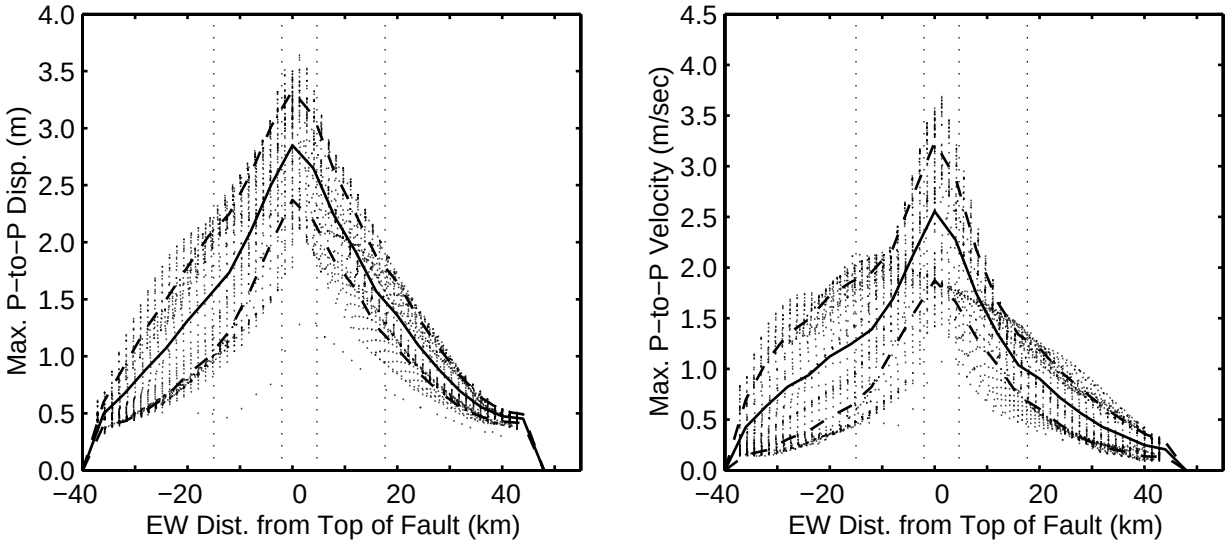

Scenario dip75HA

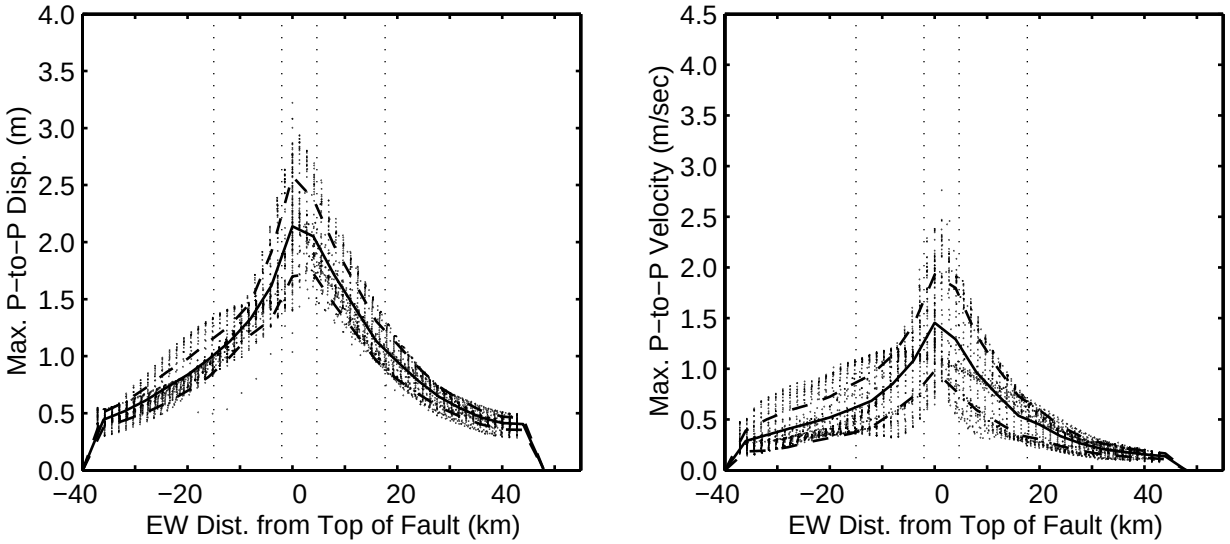

Scenario dip75HB

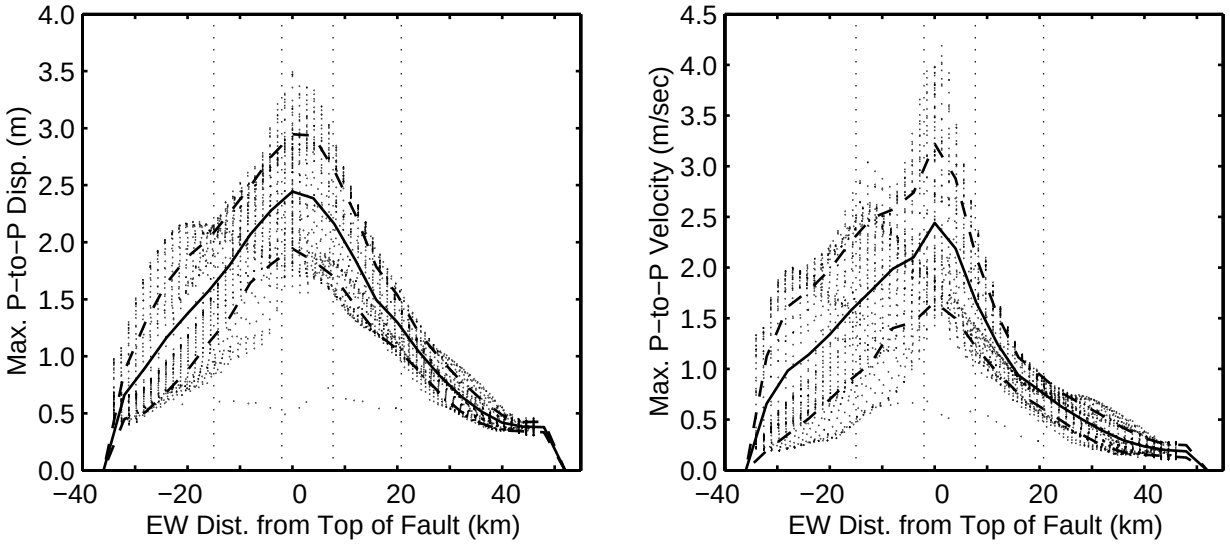

Scenario dip60HA

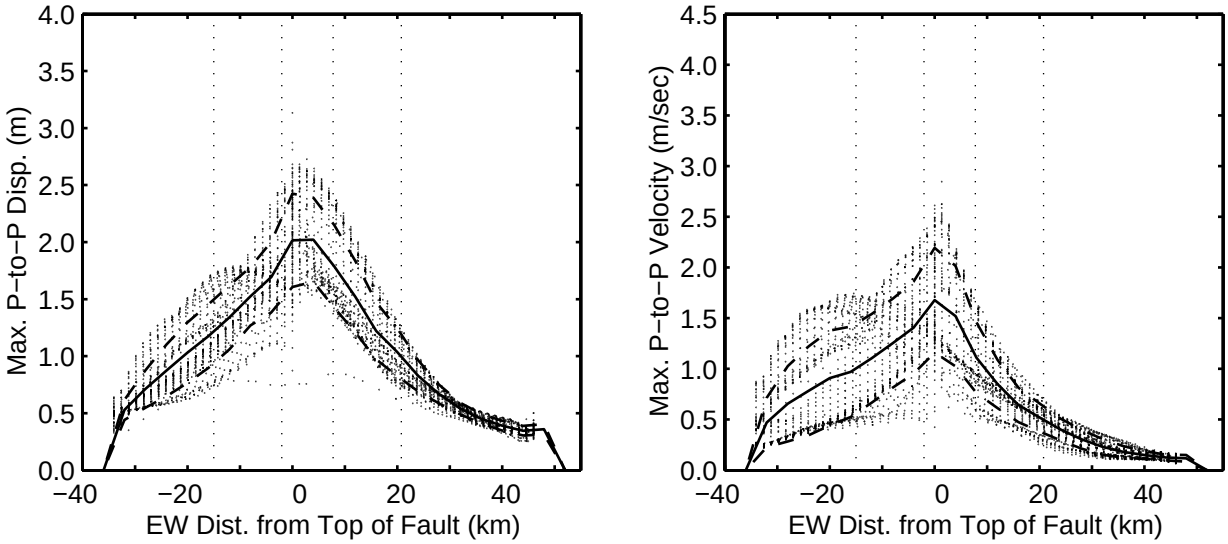

Scenario dip60HB

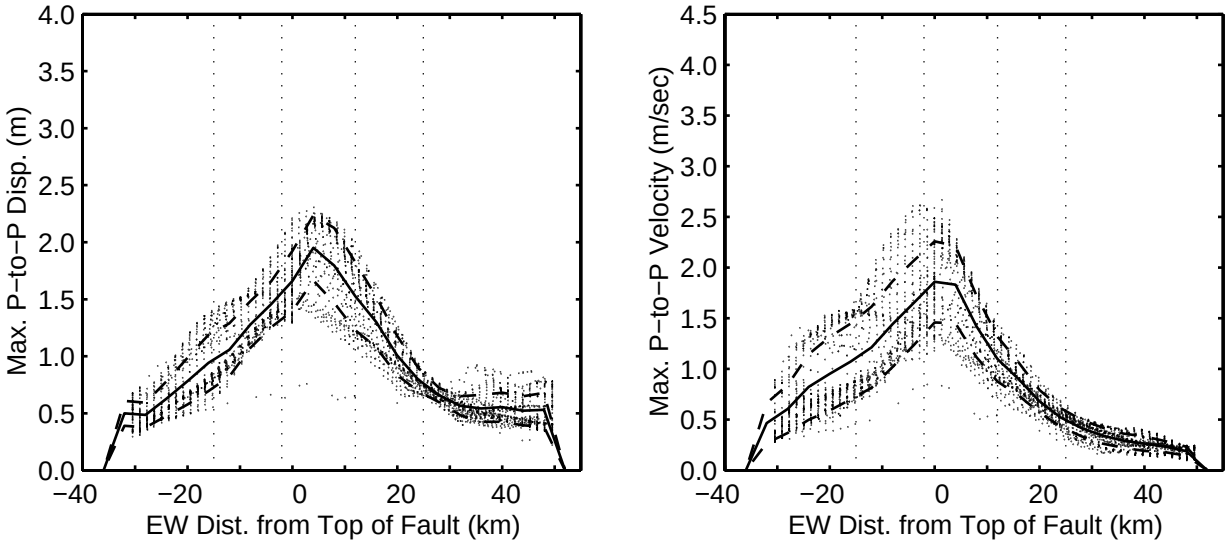

Scenario dip45HA

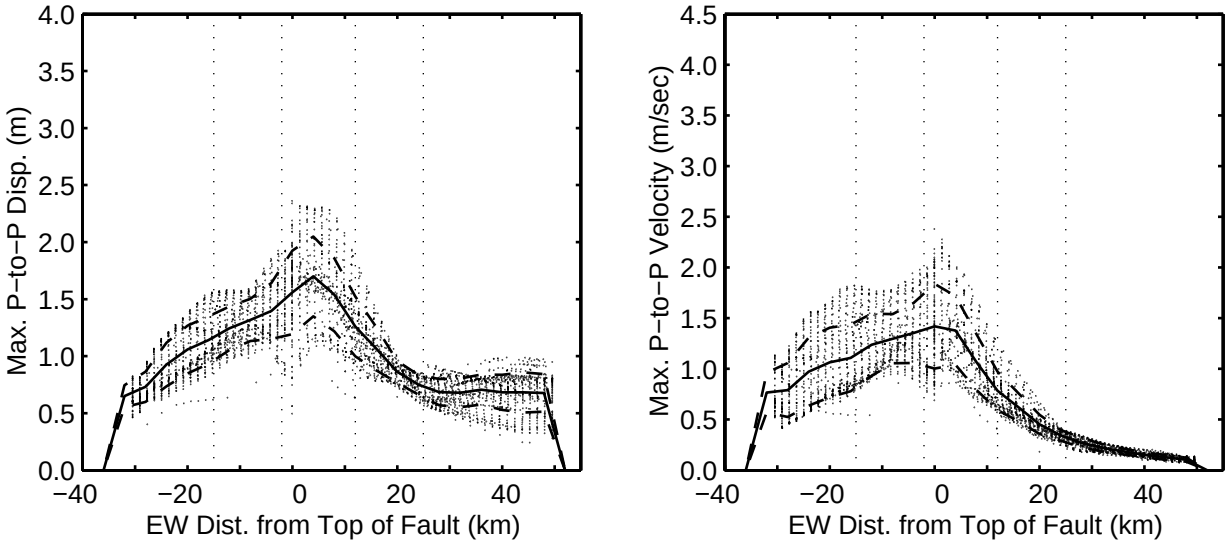

Scenario dip45HB

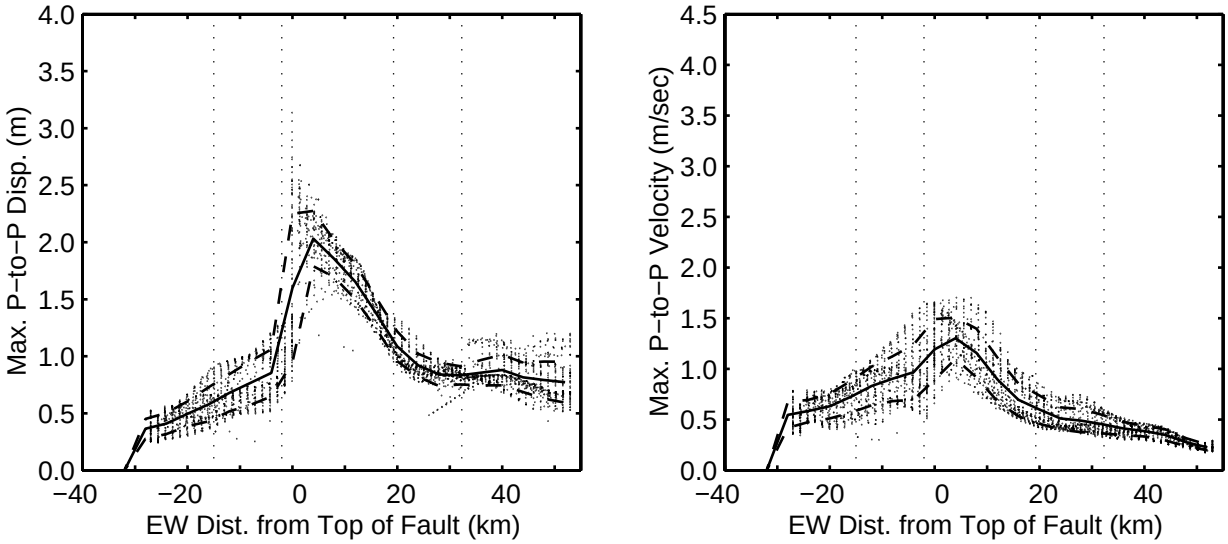

Scenario dip30HA

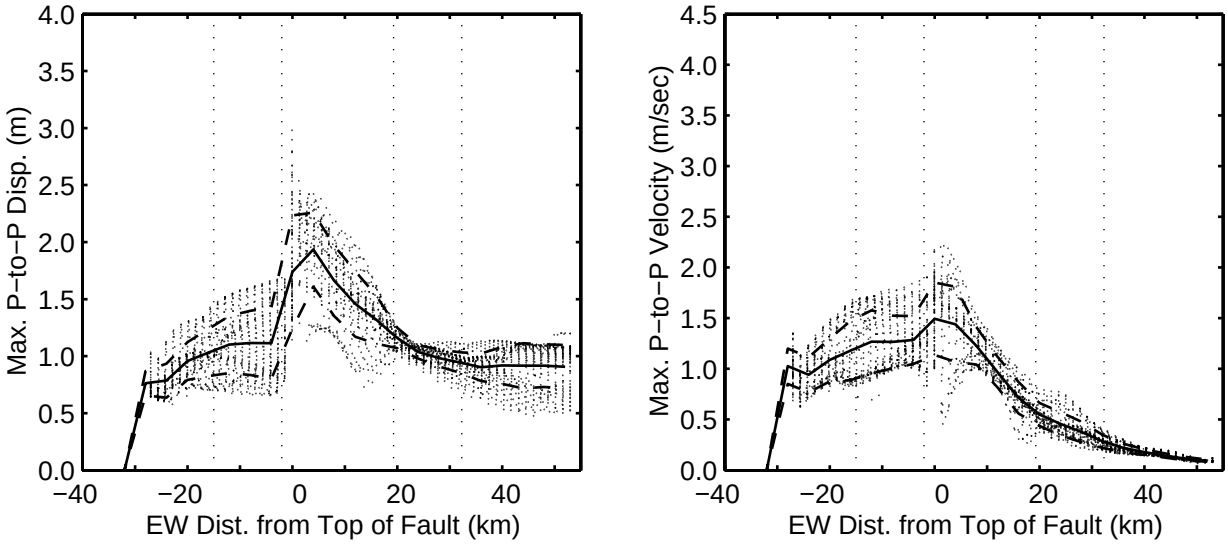

Scenario dip30HB

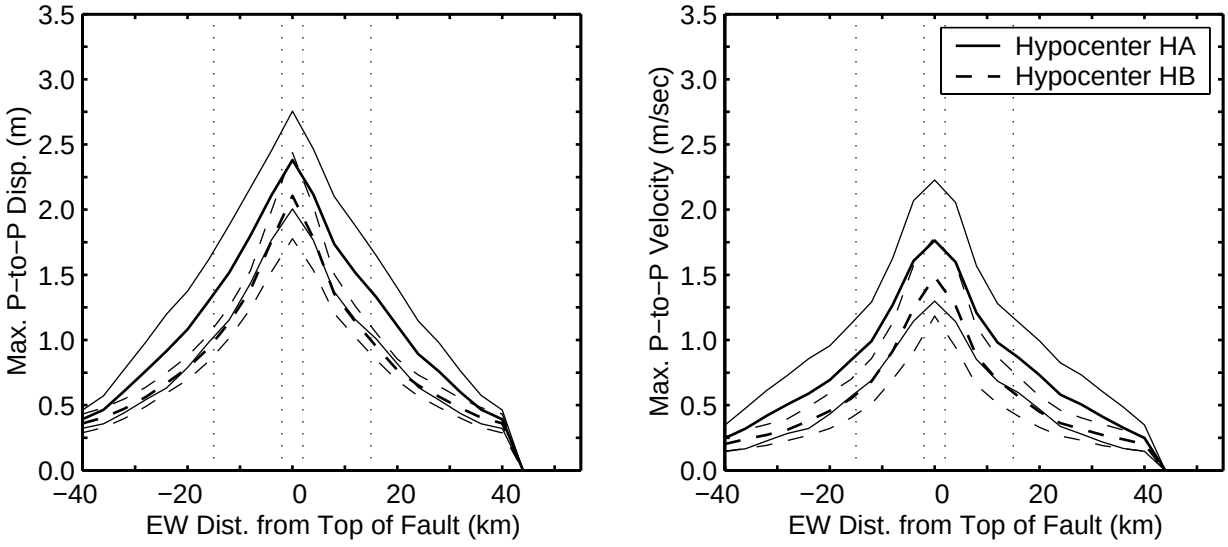

Scenarios dip90HA and dip90HB

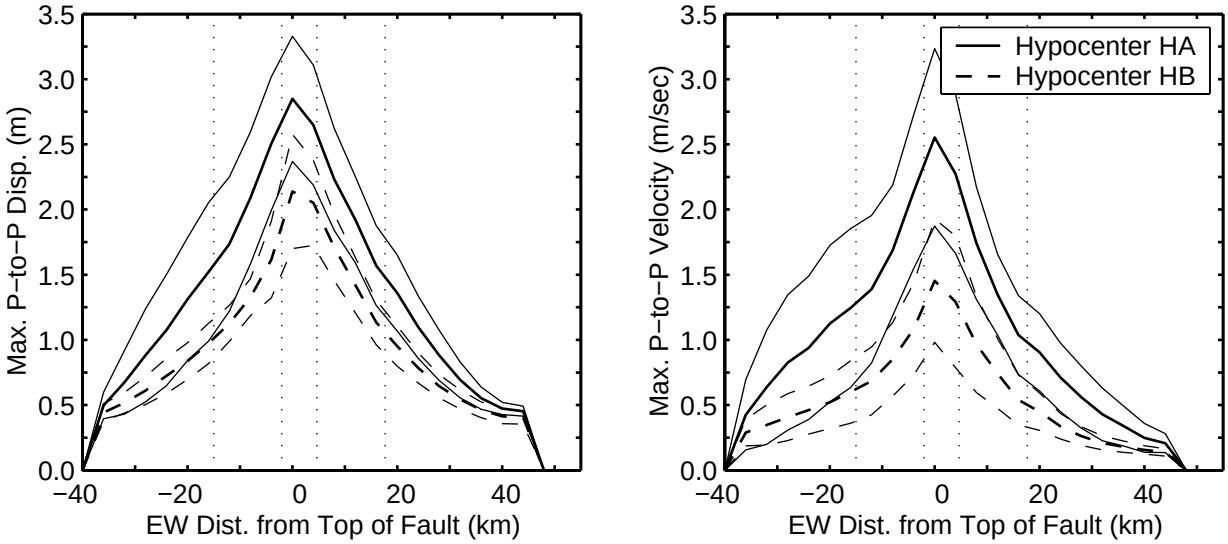

Scenarios dip75HA and dip75HB

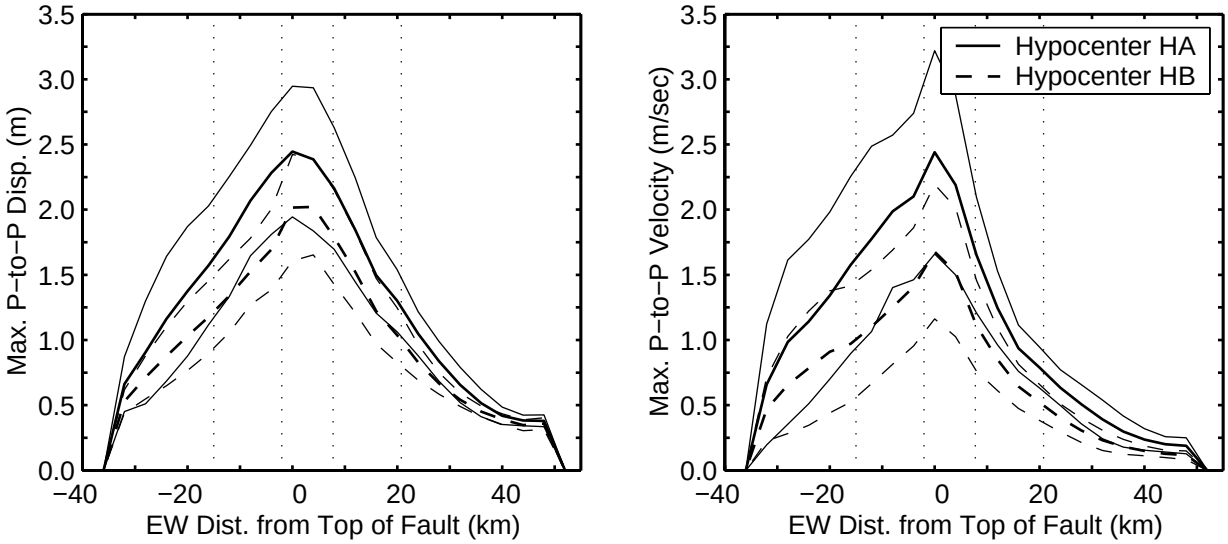

Scenarios dip60HA and dip60HB

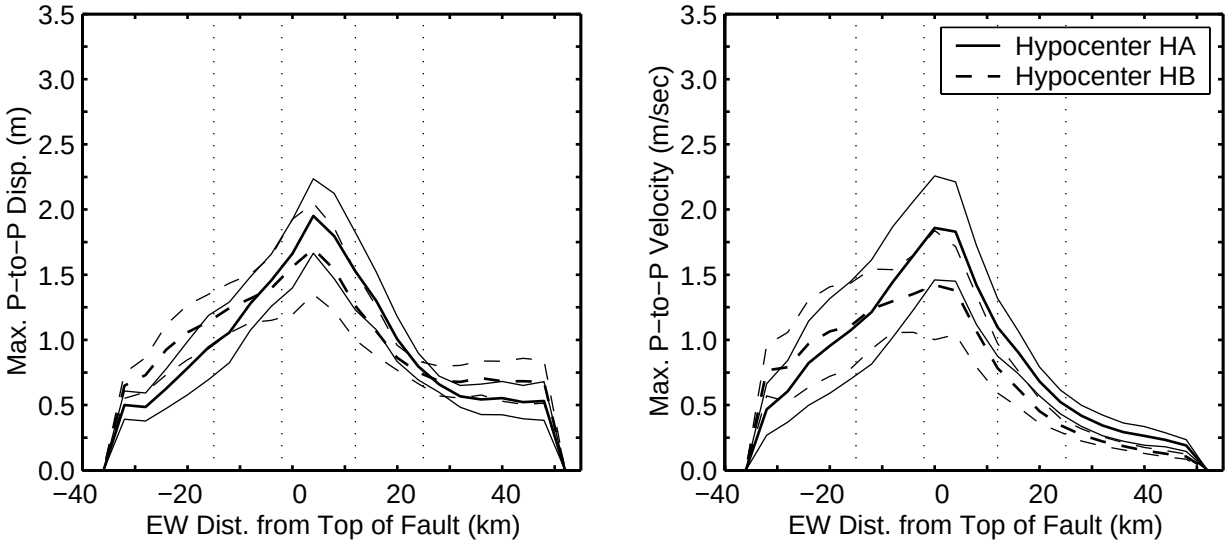

Scenarios dip45HA and dip45HB

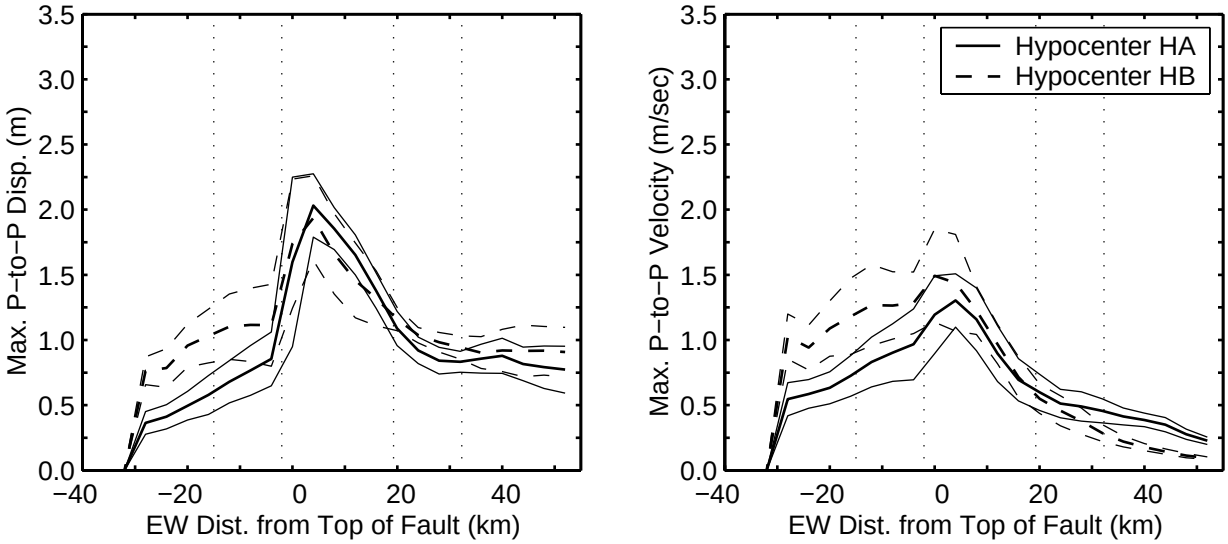

Scenarios dip30HA and dip30HB

PEER REPORTS

PEER reports are available from the National Information Service for Earthquake Engineering (NISEE). To order PEER reports, please contact the Pacific Earthquake Engineering Research Center, 1301 South 46th Street, Richmond, California 94804-4698. Tel.: (510) 231-9468; Fax: (510) 231-9461.

PEER 2002/13 *Probabilistic Models and Fragility Estimates for Bridge Components and Systems.* Paolo Gardoni, Armen Der Kiureghian, and Khalid M. Mosalam. June 2002.

PEER 2002/12 *Effects of Fault Dip and Slip Rake on Near-Source Ground Motions: Why Chi-Chi Was a Relatively Mild M7.6 Earthquake.* Brad T. Aagaard, John F. Hall, and Thomas H. Heaton. December 2002.

PEER 2002/11 Analytical and Experimental Study of Fiber-Reinforced Strip Isolators. *James M. Kelly and Shakzhod M. Takhirov.* September 2002.

PEER 2002/09 *Documentation and Analysis of Field Case Histories of Seismic Compression during the 1994 Northridge, California, Earthquake.* Jonathan P. Stewart, Patrick M. Smith, Daniel H. Whang, and Jonathan D. Bray. October 2002.

PEER 2002/08 *Component Testing, Stability Analysis and Characterization of Buckling-Restrained Unbonded Braces™.* Cameron Black, Nicos Makris, and Ian Aiken. September 2002.

PEER 2002/07 *Seismic Performance of Pile-Wharf Connections.* Charles W. Roeder, Robert Graff, Jennifer Soderstrom, and Jun Han Yoo. December 2001.

PEER 2002/06 *The Use of Benefit-Cost Analysis for Evaluation of Performance-Based Earthquake Engineering Decisions*. Richard O. Zerbe and Anthony Falit-Baiamonte. September 2001.

PEER 2002/05 *Guidelines, Specifications, and Seismic Performance Characterization of Nonstructural Building Components and Equipment*. André Filiatrault, Constantin Christopoulos, and Christopher Stearns. September 2001.

PEER 2002/03 *Investigation of Sensitivity of Building Loss Estimates to Major Uncertain Variables for the Van Nuys Testbed.* Keith A. Porter, James L. Beck, and Rustem V. Shaikhutdinov. August 2002.

PEER 2002/02 *The Third U.S.-Japan Workshop on Performance-Based Earthquake Engineering Methodology for Reinforced Concrete Building Structures*. July 2002.

PEER 2002/01 *Nonstructural Loss Estimation: The UC Berkeley Case Study. Mary C. Comerio and John C. Stallmeyer.* December 2001.

PEER 2001/16 *Statistics of SDF-System Estimate of Roof Displacement for Pushover Analysis of Buildings.* Anil K. Chopra, Rakesh K. Goel, and Chatpan Chintanapakdee. December 2001.

PEER 2001/15 *Damage to Bridges during the 2001 Nisqually Earthquake.* R. Tyler Ranf, Marc O. Eberhard, and Michael P. Berry. November 2001.

PEER 2001/14 *Rocking Response of Equipment Anchored to a Base Foundation.* Nicos Makris and Cameron J. Black. September 2001.

PEER 2001/13 *Modeling Soil Liquefaction Hazards for Performance-Based Earthquake Engineering.* Steven L. Kramer and Ahmed-W. Elgamal. February 2001.

PEER 2001/12 *Development of Geotechnical Capabilities in OpenSees.* Boris Jeremic. September 2001.

PEER 2001/11 *Analytical and Experimental Study of Fiber-Reinforced Elastomeric Isolators*. James M. Kelly and Shakhzod M. Takhirov. September 2001.

PEER 2001/10 *Amplification Factors for Spectral Acceleration in Active Regions.* Jonathan P. Stewart, Andrew H. Liu, Yoojoong Choi, and Mehmet B. Baturay. December 2001.

PEER 2001/09 *Ground Motion Evaluation Procedures for Performance-Based Design.* Jonathan P. Stewart, Shyh-Jeng Chiou, Jonathan D. Bray, Robert W. Graves, Paul G. Somerville, and Norman A. Abrahamson. September 2001.

PEER 2001/08 *Experimental and Computational Evaluation of Reinforced Concrete Bridge Beam-Column Connections for Seismic Performance*. Clay J. Naito, Jack P. Moehle, and Khalid M. Mosalam. November 2001.

PEER 2001/07 *The Rocking Spectrum and the Shortcomings of Design Guidelines.* Nicos Makris and Dimitrios Konstantinidis. August 2001.

PEER 2001/06 *Development of an Electrical Substation Equipment Performance Database for Evaluation of Equipment Fragilities*. Thalia Agnanos. April 1999.

PEER 2001/05 *Stiffness Analysis of Fiber-Reinforced Elastomeric Isolators.* Hsiang-Chuan Tsai and James M. Kelly. May 2001.

PEER 2001/04 *Organizational and Societal Considerations for Performance-Based Earthquake Engineering.* Peter J. May. April 2001.

PEER 2001/03 *A Modal Pushover Analysis Procedure to Estimate Seismic Demands for Buildings: Theory and Preliminary Evaluation.* Anil K. Chopra and Rakesh K. Goel. January 2001.

PEER 2001/02 *Seismic Response Analysis of Highway Overcrossings Including Soil-Structure Interaction.* Jian Zhang and Nicos Makris. March 2001.

PEER 2001/01 *Experimental Study of Large Seismic Steel Beam-to-Column Connections.* Egor P. Popov and Shakhzod M. Takhirov. November 2000.

PEER 2000/10 *The Second U.S.-Japan Workshop on Performance-Based Earthquake Engineering Methodology for Reinforced Concrete Building Structures.* March 2000.

PEER 2000/09 *Structural Engineering Reconnaissance of the August 17, 1999 Earthquake: Kocaeli (Izmit), Turkey.* Halil Sezen, Kenneth J. Elwood, Andrew S. Whittaker, Khalid Mosalam, John J. Wallace, and John F. Stanton. December 2000.

PEER 2000/08 *Behavior of Reinforced Concrete Bridge Columns Having Varying Aspect Ratios and Varying Lengths of Confinement.* Anthony J. Calderone, Dawn E. Lehman, and Jack P. Moehle. January 2001.

PEER 2000/07 *Cover-Plate and Flange-Plate Reinforced Steel Moment-Resisting Connections.* Taejin Kim, Andrew S. Whittaker, Amir S. Gilani, Vitelmo V. Bertero, and Shakhzod M. Takhirov. September 2000.

PEER 2000/06 *Seismic Evaluation and Analysis of 230-kV Disconnect Switches.* Amir S. J. Gilani, Andrew S. Whittaker, Gregory L. Fenves, Chun-Hao Chen, Henry Ho, and Eric Fujisaki. July 2000.

PEER 2000/05 *Performance-Based Evaluation of Exterior Reinforced Concrete Building Joints for Seismic Excitation.* Chandra Clyde, Chris P. Pantelides, and Lawrence D. Reaveley. July 2000.

PEER 2000/04 *An Evaluation of Seismic Energy Demand: An Attenuation Approach.* Chung-Che Chou and Chia-Ming Uang. July 1999.

PEER 2000/03 *Framing Earthquake Retrofitting Decisions: The Case of Hillside Homes in Los Angeles.* Detlof von Winterfeldt, Nels Roselund, and Alicia Kitsuse. March 2000.

PEER 2000/02 *U.S.-Japan Workshop on the Effects of Near-Field Earthquake Shaking.* Andrew Whittaker, ed. July 2000.

PEER 2000/01 *Further Studies on Seismic Interaction in Interconnected Electrical Substation Equipment.* Armen Der Kiureghian, Kee-Jeung Hong, and Jerome L. Sackman. November 1999.

PEER 1999/14 *Seismic Evaluation and Retrofit of 230-kV Porcelain Transformer Bushings*. Amir S. Gilani, Andrew S. Whittaker, Gregory L. Fenves, and Eric Fujisaki. December 1999.

PEER 1999/13 *Building Vulnerability Studies: Modeling and Evaluation of Tilt-up and Steel Reinforced Concrete Buildings.* John W. Wallace, Jonathan P. Stewart, and Andrew S. Whittaker, editors. December 1999.

PEER 1999/12 *Rehabilitation of Nonductile RC Frame Building Using Encasement Plates and Energy-Dissipating Devices.* Mehrdad Sasani, Vitelmo V. Bertero, James C. Anderson. December 1999.

PEER 1999/11 *Performance Evaluation Database for Concrete Bridge Components and Systems under Simulated Seismic Loads.* Yael D. Hose and Frieder Seible. November 1999.

PEER 1999/10 *U.S.-Japan Workshop on Performance-Based Earthquake Engineering Methodology for Reinforced Concrete Building Structures.* December 1999.

PEER 1999/09 *Performance Improvement of Long Period Building Structures Subjected to Severe Pulse-Type Ground Motions*. James C. Anderson, Vitelmo V. Bertero, and Raul Bertero. October 1999.

PEER 1999/08 *Envelopes for Seismic Response Vectors.* Charles Menun and Armen Der Kiureghian. July 1999.

PEER 1999/07 *Documentation of Strengths and Weaknesses of Current Computer Analysis Methods for Seismic Performance of Reinforced Concrete Members.* William F. Cofer. November 1999.

PEER 1999/06 *Rocking Response and Overturning of Anchored Equipment under Seismic Excitations.* Nicos Makris and Jian Zhang. November 1999.

PEER 1999/05 *Seismic Evaluation of 550 kV Porcelain Transformer Bushings.* Amir S. Gilani, Andrew S. Whittaker, Gregory L. Fenves, and Eric Fujisaki. October 1999.

PEER 1999/04 *Adoption and Enforcement of Earthquake Risk-Reduction Measures.* Peter J. May, Raymond J. Burby, T. Jens Feeley, and Robert Wood.

PEER 1999/03 *Task 3 Characterization of Site Response General Site Categories*. Adrian Rodriguez-Marek, Jonathan D. Bray, and Norman Abrahamson. February 1999.

PEER 1999/02 *Capacity-Demand-Diagram Methods for Estimating Seismic Deformation of Inelastic Structures: SDF Systems*. Anil K. Chopra and Rakesh Goel. April 1999.

PEER 1999/01 *Interaction in Interconnected Electrical Substation Equipment Subjected to Earthquake Ground Motions.* Armen Der Kiureghian, Jerome L. Sackman, and Kee-Jeung Hong. February 1999.

PEER 1998/08 *Behavior and Failure Analysis of a Multiple-Frame Highway Bridge in the 1994 Northridge Earthquake.* Gregory L. Fenves and Michael Ellery. December 1998.

PEER 1998/07 *Empirical Evaluation of Inertial Soil-Structure Interaction Effects.* Jonathan P. Stewart, Raymond B. Seed, and Gregory L. Fenves. November 1998.

PEER 1998/06 *Effect of Damping Mechanisms on the Response of Seismic Isolated Structures.* Nicos Makris and Shih-Po Chang. November 1998.

PEER 1998/05 *Rocking Response and Overturning of Equipment under Horizontal Pulse-Type Motions.* Nicos Makris and Yiannis Roussos. October 1998.

PEER 1998/04 *Pacific Earthquake Engineering Research Invitational Workshop Proceedings, May 14–15, 1998: Defining the Links between Planning, Policy Analysis, Economics and Earthquake Engineering.* Mary Comerio and Peter Gordon. September 1998.

PEER 1998/03 *Repair/Upgrade Procedures for Welded Beam to Column Connections.* James C. Anderson and Xiaojing Duan. May 1998.

PEER 1998/02 *Seismic Evaluation of 196 kV Porcelain Transformer Bushings.* Amir S. Gilani, Juan W. Chavez, Gregory L. Fenves, and Andrew S. Whittaker. May 1998.

PEER 1998/01 *Seismic Performance of Well-Confined Concrete Bridge Columns.* Dawn E. Lehman and Jack P. Moehle. December 2000.